PONTIFICIA UNIVERSIDAD CATOLICA DE CHILE

SCHOOL OF ENGINEERING

TOPOGRAPHICAL, CLIMATIC, AND GEOLOGICAL CONTROLS OF GROUNDWATER FLOW IN MOUNTAINOUS SYSTEMS – IMPACT ON MOUNTAIN BLOCK RECHARGE AND GROUNDWATER-SURFACE WATER INTERACTION

ETIENNE BERNARD CHRISTIAN MARTI

Thesis submitted to the Office of Graduate Studies in partial fulfillment of the requirements for the Degree of Doctor in Engineering Sciences

Advisors:
SARAH LERAY
GONZALO YÁÑEZ

Santiago de Chile, March,2024

PONTIFICIA UNIVERSIDAD CATOLICA DE CHILE
SCHOOL OF ENGINEERING

TOPOGRAPHICAL, CLIMATIC, AND GEOLOGICAL CONTROLS OF GROUNDWATER FLOW IN MOUNTAINOUS SYSTEMS – IMPACT ON MOUNTAIN BLOCK RECHARGE AND GROUNDWATER-SURFACE WATER INTERACTION

ETIENNE BERNARD CHRISTIAN MARTI

Members of the Committee:

SARAH LERAY
GONZALO YÁÑEZ
MARCELA SÁNCHEZ
JAIME ARAYA
FRANCISCO SUÁREZ
CLÉMENT ROQUES
GUSTAVO LAGOS

Thesis submitted to the Office of Graduate Studies in partial fulfillment of the requirements for the Degree Doctor in Engineering Sciences

Santiago de Chile, March, 2024

À mes parents.

« C'est en allant vers la mer que le fleuve reste fidèle à sa source. »

Jean Jaurès

ACKNOWLEDGEMENTS

I would like to begin by expressing my gratitude to my advisors, Sarah Leray and Gonzalo Yáñez, whose guidance made this thesis possible. Both of you received me as an equal and made me understand that there were no silly questions. Sarah, thank you for everything, if you didn't think a French geophysicist with no skill in Spanish could become a good hydrogeologist in Chile, none of this would have been possible. Your trust, support and availability made this journey a lot easier. Gonzalo, I am grateful for your patience and dedication teaching me a fraction of your immense geophysical and geological knowledge, as well as sharing your Chilean way of thinking.

In a less formal way, yet equally influential role, I extend my thanks to Clément Roques, for the important part he played in this thesis. Including his endless ideas, the availability for our online meetings, and for the good times shared in Switzerland.

Then, I would like to express my gratitude the members of the committee: Marcela Sánchez, Jaime Araya, and Francisco Suárez, for our conversations and your perspectives on my investigation. Special mention for the professor Suárez, for our adventurous field trip in the Quebrada de Tarapacá.

My appreciation extends to the Pontificia Universidad Católica de Chile and the VRI for the scholarship and the opportunity to work in such a supportive environment. I am also grateful to Chile for its breathtaking landscapes and the kindness of its people.

On a more personal note, I thank the people from the Departamento de Hidráulica and from the Sala Austal, - Cesar, Carlos, Andreina, Matias, Angel, Betza, Carolina, and others who joined or left during my stay- for all the good moments shared together. To Sebastian and Eneko, I am thankful for the unforgettable field trip to Ojos del Salado and the lifelong memories we created.

My gratitude goes to Ronny, Jorge, Jose, Fernanda, Catalina, and Juan from the PUC geophysical team for all the field experiences. I also appreciate the friendships formed during my exchange in Neuchatel at the CHYN, particularly with Ronan, my office mate and EGU companion.

Special thanks to my friend Jesus for the great times in France and Chile, and to his parents, Nora and Ricardo, for welcoming me into their home when I first arrived in Chile. I also thank my long-time friends Lucas, Bruno, and Franck for staying in touch despite the distance, and my Paris VII and IPGP friends - Iale, Robin, Yann, Elliot – geosciences will not have been the same without you.

A heartfelt thank you to my partner Michelle, who knew how to cheer me up in tough times, while giving me my alone time when needed.

Finally, I extend my deepest thanks to my family, both those with us and those who left us too soon. A special acknowledgment to my parents, whose unwavering support and encouragement were indispensable during challenging and uncertain times.

Thank you all!

TABLE OF CONTENTS

ACKNOWLEDGEMENTS ..... **ii**

TABLE OF CONTENTS ..... **iv**

TABLES ..... **viii**

FIGURES ..... **ix**

ABSTRACT ..... **xv**

RESUMEN ..... **xvi**

THESIS OUTLINE ..... **xvii**

1. INTRODUCTION **1**

1.1. Mountain Front Recharge and mountain block groundwater flows organization 2

1.2. Principal controls of groundwater flows 4

1.2.1. Topography 4

1.2.2. Climate 5

1.2.3. Geology 6

1.2.4. Equivalence between recharge (R) and hydraulic conductivity (K) 8

1.3. Groundwater surface water interactions 9

1.4. Research questions and hypotheses 9

1.5. Main and specifics objectives 11

2. METHODOLOGICAL APPROACH **12**

2.1. North-Central Chile geomorphological and climatic context 12

2.2. Numerical approach 15

2.3. Field approach 17

2.4. Establishing a link between presented publications and specific objectives 18

3. FROM LOWLANDS TO MOUNTAIN PEAKS: IMPACTS OF LANDFORMS ON THE DESATURATION OF GROUNDWATER-DEPENDENT WETLANDS 20

3.1. Introduction 20

3.2. Material and methods 22

3.2.1. Geomorphological context 22

3.2.2. Classification of catchment topographies 24

3.2.3. Numerical modelling of seepage area 25

3.3. Results 27

3.3.1. Typology of catchments topography 27

3.3.2. Seepage distribution evolution with increasing K/R 28

3.3.3. Seepage patterns in representative catchments 30

3.3.4. Linking topographic features and desaturation behavior 31

3.4. Discussion and perspectives 33

3.5. Acknowledgments 34

3.6. Open Research 34

4. UNRAVELLING GEOLOGICAL CONTROLS ON GROUNDWATER FLOWS AND SURFACE WATER-GROUNDWATER INTERACTION IN MOUNTAIN SYSTEMS: A MULTI-DISCIPLINARY APPROACH 36

4.1. Introduction 36

4.1. Study site and methodology 40

4.1.1. Study site 40

4.1.1.1. Climatic context 40

4.1.1.2. Geological context 41

4.1.2. Geological methodology 43

4.1.3. Geophysical methods 43

4.1.3.1. Electrical Resistivity 43

4.1.3.2. Gravimetry 44

4.1.3.3. UAV-based magnetic survey 45

4.1.4. Streamflow measurements, remote sensing data, and hydric markers 46

4.1.5. Conceptual hydrogeological models 47

4.2. Results 48

4.2.1. Geology 48
4.2.2. Geophysical study 49
4.2.3. Streamflow measurements and remote sensing analysis 54
4.2.4. Joint interpretation of geophysical and geological results and hydraulic markers 56
4.3. Discussion 57
4.3.1. Conceptual hydrogeological models 57
4.3.2. Differentiating aspects and novelty of the approach 60
4.4. Conclusions 61
4.5. Acknowledgments 62
5. GEOLOGICAL STRUCTURES PERMEABILITY IMPACT ON GROUNDWATER FLOWS IN MOUNTAIN SYSTEMS: A NUMERICAL SENSITIVITY STUDY 63
5.1. Introduction 63
5.2. Material and methods 67
5.2.1. Study site and modeled domain 67
5.2.2. Numerical modelling 69
5.2.3. Establishing a reference case for the sensitivity study 69
5.2.4. Parameters space 70
5.2.5. Hydrological indicators 72
5.3. Results 73
5.3.1. Head relative differences and Seepage ratio 74
5.3.2. Flows arrival zones 76
5.3.3. Particles residence time and flow length 78
5.3.4. Residence times proportion and flows organization 79
5.4. Discussion 82
5.4.1. Local effects – How the fractures area affects flow path lengths 82
5.4.2. Backward tracking and origin of water 83
5.5. Conclusions 85
6. CONCLUSIONS AND PERSPECTIVES 87
6.1. Generalizing results to gain perspective on mountain systems 87

6.2. General remarks and paths to explore 89

7. REFERENCES 91

A. APPENDICES 113

A.1. Supplementary Material for chapter 3 113

A.2. Supplementary Material for chapter 4 120

A.3. Supplementary Material for chapter 5 124

TABLES

Table 4-1 Mean measured density (g/cc) and mean magnetic susceptibility (SI) for rock samples collected on the field (20 samples).....50

Table 4-2 Summary of possible conceptual models associated with their main process and the geological structure involved. Contribution surface values corresponds to Figure 4-7 area.....58

FIGURES

Figure 1-1 Mountain Block settings with groundwater flows organization and MFR components. Own elaboration. 3

Figure 1-2 Profile between the topographic high and low points of a catchment, with two types of conceptual reliefs and their interaction with the water table. Own elaboration. 5

Figure 1-3 Topographical cross section associated with two level of water table. The sky-blue line for a higher recharge rate and the navy-blue line for a lower recharge rate. Own elaboration. 6

Figure 1-4 a) Active circulation zone definition according to hydraulic conductivity and estimated depth. b) Impact on groundwater flows of a fault at the mountain block limit with the lowland aquifer. Groundwater flows example for a permeable fault (sky-blue line) or an impermeable fault (navy-blue line). Own elaboration. 7

Figure 2-1 a) Morphological settings along the North of Chile. B) Topographic map of Northern Chile. Own elaboration. 13

Figure 3-1 Workflow for topographical classification: a) Situation and topographic maps of the study area in which the 60 studied catchments are delimited by a colored line. The color scheme corresponds to the three clusters obtained after applying the classification methodology (section 3.2.2) and is maintained throughout. b) Classification of topographical features exemplified in one catchment: the landforms map, landforms proportion, and a reminder of principal landforms. c) PCA plot, displaying PC2 against PC1 with the percentage of variance in the dataset explained by each component. Each red arrow represents the landform eigenvectors. 23

Figure 3-2 Model features for one example catchment: a) Horizontal discretization and buffer zone beyond catchment limits, b) AA' cross-section including vertical discretization and an arbitrary water table intercepting the topography creating seepage areas (red dots), c) Sensitivity study results (blue dotted curve) with the power law fit (dashed red curve). 26

Figure 3-3 a) Normalized seepage area against K/R for the 60 catchments (colored lines with markers), including PCA results on the upper-right corner. Four illustrative

catchments are highlighted: mountain type M1 (blue diamond, b)), lowland type L2 (red cross, c)), transitory type T3 (green triangle, d)) and T4 (green cross, e)). Details include the topographic map overlayed by the seepage area at an arbitrary value of 20% (red mask) with corresponding K/R value followed by the landforms histogram. 29

Figure 3-4 Scatter plots for the 60-catchment dataset with spearman correlation coefficient r. a) λ against PC1 including the equation and the coefficient of determination (R2) coefficient of a global fit (black line with 95% confidence interval) and b) n against PC2 including the equations and the coefficients of determination (R2) of cluster-scale fits (colored lines with 95% confidence interval). The transparent mountain catchment point was excluded from the fit.....31

Figure 4-1 a) Satellite view of the Santiago area, the white rectangle outlines the study area. b) Topographic map overlaid with the Parque Nacional del Río Clarillo catchment limits, the drainage system and the streamflow measurement points (numbered in increasing order from P0 to P8 going upstream) c) geological map of the study area overlaid with the ERT profile (blue lines), the gravimetric profile (red triangles), the area covered by the aeromagnetic flights (areas delimited by purple line) and the river flow measurements (white dots surrounded by black). A 23°C perennial thermal spring located at the exit of the Parque Nacional del Río Clarillo is indicated with a red dot. 41

Figure 4-2 Aeromagnetic anomaly map (reduced to the pole) for the Río Clarillo area (Figure 4-1, purple rectangle). Dashed lines represent the limit between magnetic zones. 49

Figure 4-3 Electrical resistivity model for the Río Clarillo transect (A-A', Figure 4-1). Projections of the hydraulic markers on the profile (red dot for the thermal spring and white dots for the river flow measurements) as well as the magnetic zones limits (Figure 4-2) presented over the transect. 51

Figure 4-4 Representation of the gravity study for the Río Clarillo transect (A-A', Figure 4-1) and the associated interpretation derived from geophysical and geological constraints. Top: The black line with crosses represents the data (each cross is one data point), the blue line represents the fit of the model described above. Bottom: Model representing the gravity data based on density variations. For a better understanding, it includes projections of the hydraulic markers on the profile (red dot for the thermal spring

and white dots for the river flow measurements) as well as the magnetic zones limits (Figure 4-2) presented above the transect. 53

Figure 4-5 Streamflow rate during the 2019 recession period (austral autumn) as a function of drainage area. P0 point corresponds to the outlet of the Parque Nacional del Río Clarillo catchment (i.e., downstream at the Andes piedmont) while P8 corresponds to the confluence of the two main affluents, approximately 9 km upstream. Orange square corresponds to March 2019 campaign, blue circle corresponds to April 2019 resampling campaign and grey triangle corresponds to the June 2019 campaign. 55

Figure 4-6 Difference between the mean NDVI of the Carrizal area and the mean NDVI of the entire National Park for the period 2000-2019, included.....56

Figure 4-7 Representation of the Parque Nacional Río Clarillo catchment with river network (blue lines) and river flow measurements (black-circled white dots). Numbers 1 to 3 correspond to the possible drainage areas contributing to the resurgence between points P4 and P5, based on the three models mentioned in sections 4.1.5 and 4.3.1. Grey area within the catchment is not part of any of the proposed models. 59

Figure 5-1 a) Situation and satellite view maps of the study area, the white rectangle corresponds to the modelled area defined on b) and d). b) Topographic map of the modelled area (borders highlighted by a dashed red line). The catchment is delimited by a red line. Faults (black lines), fractures area (black rectangle), the river network (light blue lines) and the constant head boundary condition (blue line) are overlayed. An A-A' cross-section is identified. c) Representation of the A-A' topographic cross-section with the model discretization illustrated. d) Representation of the modelled area with structures (green lines and rectangle) and hydraulic conductivities of modelled units, yellow unit for the sedimentary area ($K_{sediments}=10^{-4}$m/s) and blue for the volcanic unit ($K_{homogeneous}=1.6*10^{-7}$m/s). The corresponding exit zones are overlayed with red text. 68

Figure 5-2 Definition and diagram of the sensitivity study, definition of the three studied scenarios. For each scenario defined according to the fractures area, we iterate 10 times on the $K_{faults}/K_{homogeneous}$ ratio. The arrow with the color gradient represents the different $K_{faults}/K_{homogeneous}$ ratio values, from the most permeable (blue) to the least permeable (red). The arrow will be repeated under results plots for references.....71

Figure 5-3 For each scenario (blue curve for scenario 1, red for scenario 2 and green for scenario 3) we plotted a) the mean relative difference (%) and b) the mean seepage ratio. Both x-axes are the $K_{faults}/K_{homogeneous}$ ranging from the more permeable case to the less permeable case with the associated gradient color arrow. Maps with topography for the more permeable case and the less permeable case of c) head relative differences (null difference is masked) and d) seepage ratio. 74

Figure 5-4 Bar-plot presenting the flow exit zone proportion based on the $K_{faults}/K_{homogeneous}$ ranging from the more permeable case to the less permeable case with the associated gradient color arrow. For each $K_{faults}/K_{homogeneous}$, bars represent one scenario each, scenario 1 to 3 from left to right, representing our 30 simulations. The ratio $K_{faults}/K_{homogeneous} = 10^0$ represents the reference case. The brown bar corresponds to the sMFR proportion of the total flows, the gold to the IB flows and the green one to MBR flows. 77

Figure 5-5 For each scenario (blue curve for scenario 1, red for scenario 2 and green for scenario 3) we plotted a) the particles weighted mean residence time (years) and b) the particles weighted mean flow path length (m). Both x-axes are the $K_{faults}/K_{homogeneous}$ ranging from the more permeable case to the less permeable case with the associated gradient color arrow. The ratio $K_{faults}/K_{homogeneous} = 10^0$ represents the reference case. 78

Figure 5-6 a) Bar-plot presenting the residence times proportion based on the $K_{faults}/K_{homogeneous}$ ranging from the more permeable case to the less permeable case with the associated gradient color arrow. For each $K_{faults}/K_{homogeneous}$. Bars represent one scenario each, scenario 1 to 3 from left to right, representing our 30 simulations. The ratio $K_{faults}/K_{homogeneous} = 10^0$ represents the reference case. The sky-blue bar corresponds to the short times, the greenish blue to intermediate times and the green one to large times. Maps of the study area overlayed with flow paths colored according to their residence times, for the more permeable case (c) and the less permeable case (d). 80

Figure 5-7 Maps zoomed on the fractures area overlayed with flow paths colored according to their length for the scenario 1 (a), the scenario 2 (b) and the scenario 3 (c). Here, the $K_{faults}/K_{homogeneous}$ is fixed at 10^{-1}. For the scenario 1, the fractures area line is dashed as it is plot only for reference perspectives. 83

Figure 5-8 Map of the study area overlayed with flow paths colored according to their residence times for IB flows entering the basin and exfiltrating in the catchment. 84

Figure A-1 Illustration of the 2D hillslope model employed to define the analytical solution, based on Bresciani et al. (2014). 113

Figure A-2 (a) Left upper panel: Topography of the hillslope $Z_{T,}$ with each color corresponding to a different slope value. Left lower panel: Seepage length ratio L_S/L plotted against the ratio R/K for each hillslope case presented on the left upper panel using the same color palette. (b) Right upper panel: Topography of the hillslope $Z_{T,}$ with each color corresponding to a different curvature degree value. Dashed lines represent concave cases, and solid lines represent convex cases. The linear case is represented by a solid red line. Right lower panel: Seepage length ratio L_S/L plotted against the ratio R/K for each hillslope case presented on the right upper panel, using the same color palette and line patterns.....116

Figure A-3 Correlation matrix between topographical parameters (PC1 and PC2) and seepage distribution parameters (λ and n) obtained from the curve fit. The diagonal part represents the distribution of each parameter associated with its name. The upper part indicates the correlation coefficient (r) between two variables, with stars indicating the strength of the correlation on a scale from 0 to 3 (for 3 stars p-value<0.001). The lower part represents the scatter plot between the two corresponding variables using the clusters color scheme. The X-axis is associated with both the scatter plots and the histogram distribution, while the Y-Axis is only associated with the scatter plots. 118

Figure A-4 Kernel Density Estimate (KDE) plot depicting the coefficient of determination (R^2) for parameter estimations of λ and n using a Random Forest algorithm. Each R^2 value corresponds to one of 6500 resampling (with replacements) iterations involving 10 catchments, serving as test data within a 60-catchment dataset, while 50 catchments were utilized for training. The sampling procedure was conducted to assess the estimation's robustness in the presence of random variations. 119

Figure A-5 Electrical resistivity model for the Rio Coipo transect (B-B', Figure 4-1). 122

Figure A-6 Model of the gravity data for the Rio Coipo transect (B-B', Figure 4-1) and the associated interpretation derived from geophysical and geological constraints. Top:

the black line with crosses represents the data, the red line represents the fit of the model described above. Bottom: Model representing the gravity data based on density variations. 123

Figure A-7 Maps with topography of head relative differences (null difference is masked) including the fractures area (Scenario 3) for a) the more permeable case and b) the less permeable case. 124

Figure A-8 Bar-plot presenting the proportion of recharge to the catchment coming from IB flows based on the K_{faults} /$K_{homogeneous}$ ranging from the more permeable case to the less permeable case. For each K_{faults} /$K_{homogeneous}$, bars represent one scenario each, scenario 1 to 3 from left to right, representing our 30 simulations. The ratio K_{faults} /$K_{homogeneous}$ = 10^0 represents the reference case. 125

ABSTRACT

Mountains, often referred to as the world's water towers, play a vital role in global water distribution. They receive significant precipitations and redistribute these waters to lower regions, thereby sustaining a major portion of our planet's water needs. Moreover, in the face of climate change and increasing human water consumption, lowland aquifers are experiencing unprecedented depletion. Thus, there is a crucial need to characterize all recharge sources arriving at the lowland aquifers, including both surface and groundwater contribution. Nevertheless, the complexity of mountain systems and their remoteness impede full comprehension of their functioning.

In this context, this thesis aims to deepen our understanding of mountainous groundwater systems and their crucial connection to lowland basins. The methodology is two-fold, using parsimonious numerical models to grasp the broader hydrogeological dynamics, and secondly, implementing an innovative, interdisciplinary field study to examine local peculiarities.

This study reveals that the topography highly influences aquifer desaturation patterns and hence groundwater-surface water interactions, further determining biogeochemical and ecological processes and impacting groundwater dependent systems. The slope contrast between flat and steep areas exerts the principal control, while landscape shape exerts a secondary control. Regarding geological heterogeneities, at the local scale, using a novel methodology, geological structures were identified and satisfactorily linked them to an increase in streamflow. Finally, in studying regional geological heterogeneities, the study unveils the role of such structures and their hydrodynamic properties on groundwater flows pattern and interbasins exchanges. The studied catchment consistently exchanges between 0 and 20% with surrounding catchments. while characterizing the contribution of mountain systems to lowland areas.

This research by questioning existing groundwater paradigms and their applicability on mountain systems thoroughly study the groundwater flow controls improving paradigms definition in mountain systems. By establishing a robust framework for future research, it underscores the need for multidisciplinary approaches to develop a comprehensive understanding of mountainous regions as vital contributors to global water resources.

RESUMEN

Las montañas, a menudo denominadas las torres de agua del mundo, desempeñan un papel vital en la distribución global del agua. Reciben importantes precipitaciones y redistribuyen estas aguas a regiones más bajas, sosteniendo así una parte importante de las necesidades de agua del sistema terrestre. Además, ante el cambio climático y el creciente consumo humano de agua, los acuíferos aluviales están experimentando un agotamiento sin precedentes. Por lo tanto, existe una necesidad crucial de caracterizar todas las fuentes de recarga que llegan a los acuíferos aluviales, incluyendo tanto la contribución de las aguas superficiales como de las subterráneas. Sin embargo, la complejidad de los sistemas montañosos y su lejanía impiden comprender plenamente su funcionamiento.

En este contexto, esta tesis pretende profundizar nuestra comprensión de los sistemas montañosos de aguas subterráneas y su conexión crucial con las cuencas aluviales. La metodología es doble: por un lado, se utilizan modelos numéricos para comprender la dinámica hidrogeológica en sentido amplio y, por otro, se lleva a cabo un estudio de campo innovador e interdisciplinar para examinar las singularidades locales.

Este estudio revela que la topografía influye en los patrones de desaturación de los acuíferos y, por tanto, en las interacciones entre las aguas subterráneas y superficiales. El contraste de pendientes entre zonas planas y empinadas ejerce el control principal, mientras que la forma del paisaje ejerce un control secundario. En cuanto a las heterogeneidades geológicas, a escala local, nuestra novedosa metodología identificó estructuras geológicas y determinó su influencia en las interacciones entre aguas subterráneas y superficiales. Por último, al estudiar las heterogeneidades geológicas regionales, el estudio desvela el papel de dichas estructuras y sus propiedades hidrodinámicas en el patrón de los flujos de aguas subterráneas.

Esta investigación, al cuestionar los paradigmas existentes sobre las aguas subterráneas y su aplicabilidad a los sistemas montañosos, estudia a fondo los controles del flujo de aguas subterráneas. Al establecer un marco sólido para futuras investigaciones, subraya la necesidad de enfoques multidisciplinarios para desarrollar una comprensión global de las regiones montañosas como contribuyentes vitales a los recursos hídricos mundiales.

DISSERTATION OUTLINE

Chapter 1: Introduction

This chapter presents the importance of mountain block systems in global hydrogeological systems. Then the state of the art regarding the key parameters of groundwater flows in mountain systems and their organization is presented along with the importance of groundwater surface waters interaction. Lastly, research questions, hypotheses and objectives are presented.

Chapter 2: Methodological approach

Here, is presented the general methodological approach used during this thesis. Presenting the numerical and field approaches as well as a description of North-Central Chile climatic and geomorphologic characteristics. Lastly, a correlation is made between the following chapters and the specific objectives of the thesis project.

Chapter 3: From lowlands to mountain peaks: impacts of landforms on the desaturation of groundwater-dependent wetlands

This chapter is a concise letter format currently under review in *Geophysical Research Letters* (AGU, WOS). It explores the impact of topography on groundwater flows and surface water interactions, as well as aquifer responses to different levels of desaturation. This numerical analysis covers 60 catchments over 1,800 km in North-Central Chile, providing insights into groundwater drivers in mountainous areas and simplifying the representation of complex topography.

Chapter 4: Unravelling geological controls on groundwater flow and surface water-groundwater interaction in mountain systems: a multi-disciplinary approach

This section presents a multidisciplinary field study in a catchment south of Santiago, Chile, published in *Journal of Hydrology* (Elsevier, WOS). It focuses on how geological structures influence the hydrogeological functioning of a mountain catchment. Introducing a novel field methodology to identify geological heterogeneities and their effects on groundwater and surface water interactions.

Chapter 5: Geological structures permeability impact on groundwater flows in mountain systems: a numerical sensitivity study

Chapter 5 conducts numerical simulations on the same Chilean catchment studied in Chapter 4, focusing on a sensitivity analysis of the hydraulic conductivity of geological structures like faults and fractures. This analysis, which utilizes real-world topography and structure data, explores the impact of hydraulic conductivity variations on flow paths, particularly examining fault zone conductivity and its effects on Mountain Front Recharge.

Chapter 6: Conclusions and perspectives

The concluding chapter of the dissertation synthesizes the key findings, linking them back to the initial research questions and hypotheses. It also highlights the study's major contributions to the field of mountain hydrogeology and propose recommendations to further advance our knowledge in this area.

1. INTRODUCTION

Climate change significantly impacts the hydrological cycle and water availability (Gleick, 1989; Konapala et al., 2020; Tabari, 2020; Viviroli et al., 2011). This is particularly true in arid areas, which presently cover 30% of the Earth's surface, as they are affected by increasingly longer, more frequent, and more intense periods of drought. Besides climatic considerations, the increasing anthropic pressure in these areas is generating more domestic and agricultural uses (D'Odorico et al., 2013; Scanlon et al., 2006; UN, 2017; Viguier et al., 2019). This escalating situation is pushing towards a critical water shortage, notably affecting traditional groundwater supplies like sedimentary aquifers. (Kummu et al., 2016; Pokhrel et al., 2021; Taucare et al., 2024; Viviroli et al., 2020). Understanding and characterizing these crucial water sources is essential, as they are a primary source of fresh water for humans and ecosystems alike (Amanambu et al., 2020; Scanlon et al., 2023; Taylor et al., 2013).

The role of mountains in the recharge of lowland and sedimentary aquifers is critical, largely due to their ability to capture increased precipitation thanks to their elevated topography, and the large surface involved. This collected water is subsequently distributed to lower regions *via* both surface streamflow and subsurface groundwater movement (Markovich et al., 2019; Somers & McKenzie, 2020; Wilson & Guan, 2004). In arid regions, this distant recharge mechanism constitutes the primary source of replenishment for lowland aquifers (Scanlon et al., 2006). It is estimated that over half the global population relies on mountain hydrosystems (Grêt-Regamey et al., 2012). Consequently, mountain catchments have gained increasing attention for their essential role as key water reservoirs that sustain downstream alluvial catchments (Hayashi, 2020; Immerzeel et al., 2020; Somers & McKenzie, 2020; Viviroli et al., 2020). Additionally, mountain ecosystems serve as unique habitats, supporting a diverse array of endemic and native species (Antonelli et al., 2018; Clarke et al., 2008; Freeman et al., 2007; Hu et al., 2020).

Yet mountain systems are particularly vulnerable to climate changes putting these ecosystems at risk (Adler et al., 2019; Egan & Price, 2017; Kløve et al., 2014; Scott et al., 2019; Siegfried et al., 2012; Vuille et al., 2018). Understanding the organization of groundwater flows in mountain systems remains a challenge due to the complexity and remoteness of these environments. Indeed, continuous hydraulic and hydrogeological monitoring in remote mountain areas is hindered by difficult access, harsh environmental conditions, and lack of infrastructure, leading to challenges in data collection and maintenance. More specifically, a complex interplay between three determining factors controls groundwater flows: topography, geology, and climate (Winter, 2001). In mountain systems characterized by steep relief and high elevations, where soils and unconsolidated sediments are typically scarce and where climate is difficult to forecast, the pronounced topographic, climatic, and geological gradients pose significant challenges in accurately characterizing the circulation of groundwater flows (Condon & Maxwell, 2015; Gleeson & Manning, 2008; Schaller & Fan, 2009; Welch & Allen, 2012) and eventually to propose conceptual hydrogeological frameworks.

1.1. Mountain Front Recharge and mountain block groundwater flows organization

Mountain Front Recharge (MFR) refers to the water that flows into lowland aquifers, originating from the mountain block. MFR is categorized into two distinct components: the surface MFR (sMFR), which is linked to surface streams that emerge from the mountain block and subsequently infiltrate the basin fill, and the mountain-block recharge (MBR). The concept of MBR, initially termed as “hidden recharge” by Feth (1964), encompasses the groundwater that moves directly from the mountain block into the basin aquifer via various pathways such as pores, fractures, or other voids in both consolidated and unconsolidated geological formations (Bresciani et al., 2018; Markovich et al., 2019; Wilson & Guan, 2004) as depicted in Figure 1-1. The MBR constitutes the underground component of recharge, yet not all water infiltrating the mountain block will eventually become MBR, as it can infiltrate and exfiltrate in the mountain block contributing to sMFR.

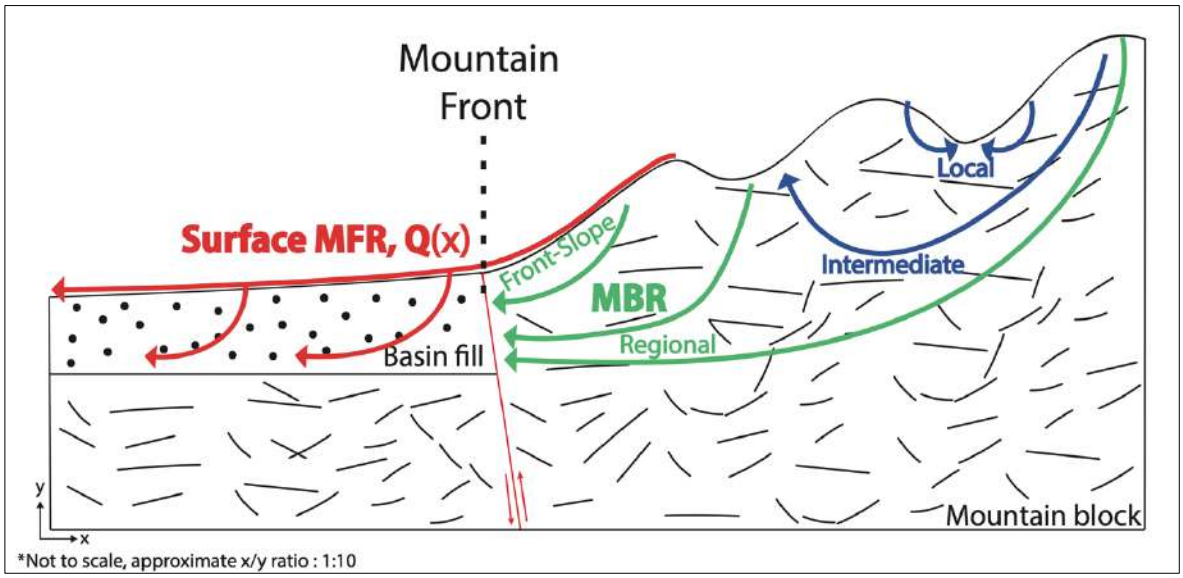

Figure 1-1 Mountain Block settings with groundwater flows organization and MFR components.

Contemporary understanding of groundwater flow in mountain systems draws heavily from early research on regional groundwater systems. Pioneering studies by Freeze & Witherspoon (1967) and particularly by Tóth (1963) continue to be referenced in current research, focusing on how topography shapes groundwater tables. Tóth's groundbreaking study proposed the existence of various nested flow paths, which he categorized into local, intermediate, and regional types. Despite being grounded in a simplified two-dimensional numerical framework, Tóth's insights remain foundational in shaping many current theories and models of groundwater flow.

Recent studies suggest the need for modifications to Tóth's model (1963) to better suit the complexities of mountainous terrains (Bresciani, Gleeson, et al., 2016; Wilson & Guan, 2004). Building upon Tóth's framework, Markovich et al. (2019) introduced the "front-slope flow", to further describe the mountain block systems framework. Front-slope flows originate on mountain front slopes and directly discharge into the basin-fill aquifer (Figure 1-1). Notably, local, and intermediate flows, which occur within the mountain block basin, contribute to sMFR, while only regional and "front-slope flows" contribute to MBR (Figure 1-1). This characteristic indicates that interactions between groundwater and surface water, as well as exchanges between basins, are likely far more intricate in high-relief areas compared to low-relief regions. This multiscale aspect of the flow would certainly determine the hydrological cycle in both its quantitative and

qualitative variables. Tóth's original theory, mainly a two-dimensional approach, may not fully capture the three-dimensional nature of groundwater flow in mountain blocks, which is influenced by the morphology of sub-basins (Gleeson & Manning, 2008; Wang et al., 2017). A significant unknown in this context is the depth and length of groundwater flow paths, as well as the extent to which the mountain block can export water as groundwater (Markovich et al., 2019; Schaller & Fan, 2009; Wilson & Guan, 2004).

1.2. Principal controls of groundwater flows

To better constrain groundwater flow patterns, the focus will be now made on the three drivers of groundwater, which are topography, climate, and geology (Winter, 2001) and their interaction. These primary factors significantly influence the elevation and morphology of the water table, which in turn affects its interaction with topography, serving as the upper boundary of groundwater systems. This interaction plays a crucial role in determining the range of groundwater flows, spanning from local to regional scales.

1.2.1. Topography

Topography is the primary factor in groundwater dynamics, with water naturally flowing from higher to lower elevations due to gravity. By examining a cross-section from the highest to the lowest points of a catchment (Figure 1-2), it can be assessed how the topographic wavelength, λ_T, influences the interactions between the water table and topography, consequently affecting flow length. A catchment with a short topographic wavelength, resembling a sinusoidal shape with incised valleys, tends to have increased interactions between the water table and the topography, leading to a higher proportion of local flows. Conversely, in a catchment with a longer wavelength, such as a more linear profile, and with the same elevation of the water table, there tends to be minimal interaction, favoring regional flows (Condon & Maxwell, 2015; Gleeson & Manning, 2008; Tóth, 1963).

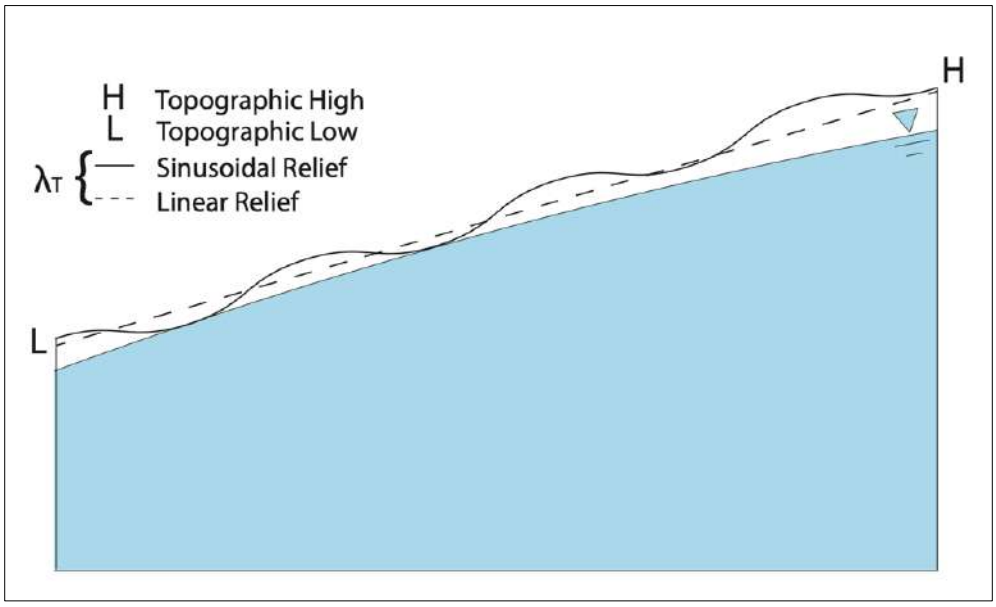

Figure 1-2 Profile between the topographic high and low points of a catchment, with two types of conceptual reliefs and their interaction with the water table.

At the hillslope scale (2D), the slope gradient plays a key role: steeper slopes are typically associated with deeper water tables and fewer interactions, while gentler slopes demonstrate a closer connection between the water table and the surface (Bresciani et al., 2014; Marçais et al., 2017). However, applying these observations to the complexities of mountain systems is challenging due to the diversity of landscapes and their unique topographical characteristics.

1.2.2. Climate

In general, the climate's influence on groundwater systems is often simplified to its impact on the basin's recharge rate. It is typically presumed that there is a direct correlation between the recharge rate and the water table's elevation, where a higher recharge rate leads to a correspondingly higher water table, and vice versa (Figure 1-3). For instance, in humid conditions, the water table tends to be closer to the surface, thereby encouraging local flows. Conversely, in arid conditions, the water table is usually deeper, which is more conducive to regional flows (Cuthbert et al., 2019; Gleeson et al., 2011; Haitjema & Mitchell-Bruker, 2005; Schaller & Fan, 2009; Scibek et al., 2007).

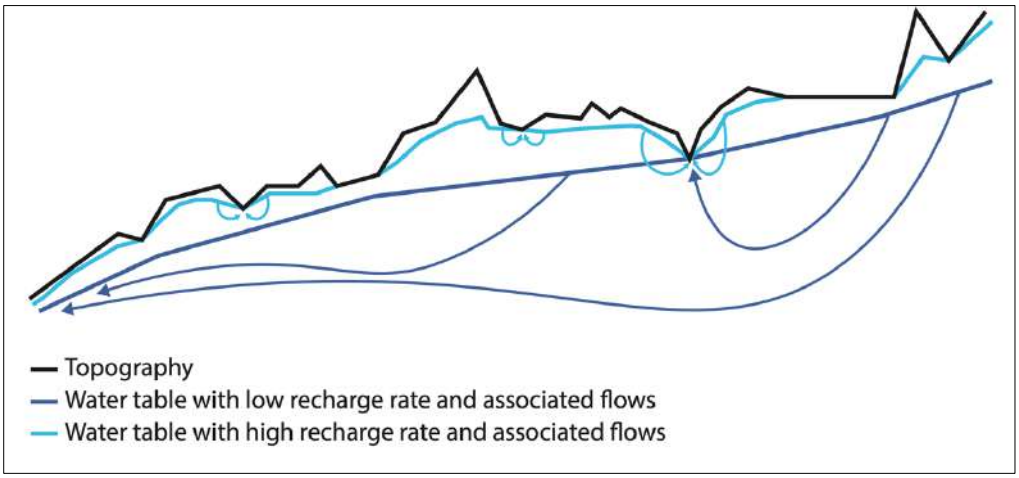

Figure 1-3 Topographical cross section associated with two level of water table. The sky-blue line for a higher recharge rate and the navy-blue line for a lower recharge rate.

1.2.3. Geology

Geological factors, due to their inherently high variability at depth influenced by geological units, weathering and structures like faults and fractures, play a less predictable role in hydrogeology. This variability is often captured through variations in permeability, primarily reflected in changes in hydraulic conductivity (K). Generally, higher K values indicate a greater proportion of groundwater flows, reduced topographic influence, deeper water table levels, and thus, an increased likelihood of regional flows (Gleeson et al., 2011, 2011; Haitjema & Mitchell-Bruker, 2005; Schaller & Fan, 2009; Welch & Allen, 2014). Additionally, the geological context and its corresponding hydraulic conductivity (K) are crucial in determining the active depth of groundwater, which significantly influences the rate and distribution of MBR (Markovich et al., 2019). Recent studies suggest that the active flow depth in bedrock is approximately 100-200 meters, representing the potential depth for fractured bedrock (with K values ranging from 10^{-8} to 10^{-6} m/s) overlying a deeper, low-K zone ($K<10^{-8}$ m/s) (Figure 1-4a) (Welch & Allen, 2014).

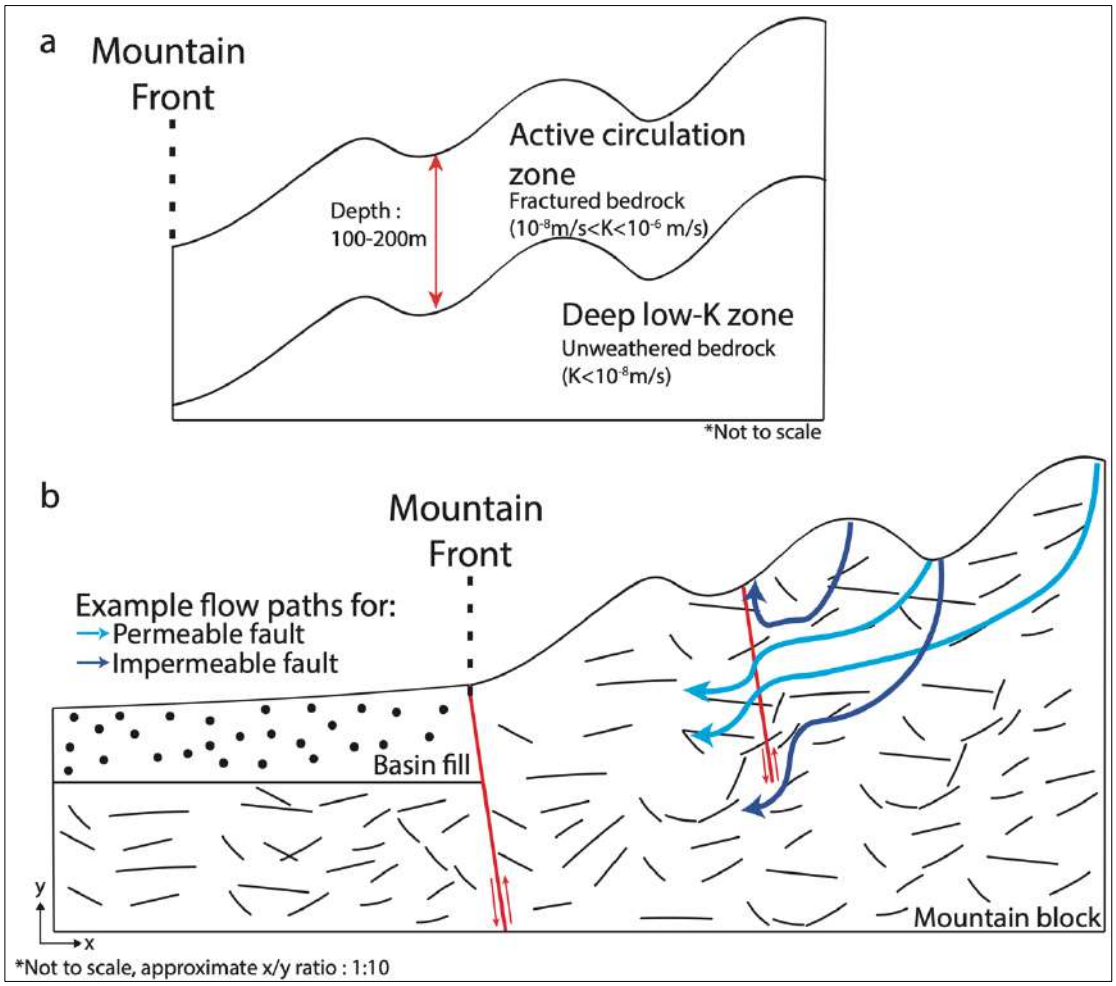

Figure 1-4 a) Active groundwater circulation zone in mountain block according to hydraulic conductivity and estimated depth. b) Impact on groundwater flows of a fault at the mountain block limit with the lowland aquifer. Groundwater flows example for a permeable fault (sky-blue line) or an impermeable fault (navy-blue line).

The presence of faults and fractures at mountain fronts and in the mountain block is well-recognized (Folch & Mas-Pla, 2008; Markovich et al., 2019; Wilson & Guan, 2004). Fault zones, especially those with significant displacement as found in major mountain ranges, can vary in thickness from several meters to tens of meters (Evans, 1990; Tsutsumi et al., 2004). These zones are typically categorized into two distinct permeability domains: the fault core and the damage zone (Caine et al., 1996; Choi et al., 2016; Faulkner et al., 2010). The fault core often contains clay-rich gouge or fault breccias, which tend to decrease permeability, whereas the damage zone is characterized by a high density of fractures that increase the medium's permeability. In terms of water

flow, the damaged zone generally facilitates groundwater movement, while the fault core acts as a barrier. Understanding the dual nature of these zones as either conduits or barriers is a complex task, with sometimes only one of these effects being observable (Scibek et al., 2016). For instance, more permeable fault zones can serve as conduits, creating preferential pathways for groundwater flow (Bense et al., 2013; Figueroa et al., 2021; Leray et al., 2013; Roques et al., 2014), while less permeable zones might redirect flows either upwards or downwards, potentially leading to groundwater resurgence or preferential recharge (Bense et al., 2003; Chowdhury et al., 2008; Figueroa et al., 2021; Rajabpour et al., 2016) (Figure 1-4b). These geological behaviors significantly affect groundwater flow length, with preferential paths or infiltration favoring more regional flow. Conversely, barrier effects that induce resurgence can result in a higher proportion of local flows and an increase in surface MFR due to the groundwater's contribution to streamflow.

1.2.4. Equivalence between recharge (R) and hydraulic conductivity (K)

In practice, unraveling the individual effects of each driver on groundwater dynamics is complex, as these drivers often operate concurrently. Moving beyond Toth's (1963) hypothesis that the water table mirrors the topography, Haitjema and Mitchell-Brucker (2005) expanded the investigation to include additional factors like aquifer geometry and depth, which influence the water table elevation. Their research, conducted along a 2D cross-section with homogeneous hydraulic conductivity and uniform recharge conditions, revealed that the water table does not always precisely replicate topography, particularly in scenarios of lower recharge rates. Crucially, their study highlighted that the determinant of water table elevation is the ratio between hydraulic conductivity (K) and average recharge rate (R). A lower K/R ratio indicates a topography-controlled water table, leading to more prevalent local and intermediate flow paths. Conversely, a higher K/R ratio points to a recharge-controlled water table, typically deeper and associated with more regional flow patterns following the smooth relief slope. This principle was further exemplified in mountainous systems (Gleeson & Manning, 2008) and applied to understanding groundwater-surface water interactions (Abhervé et al., 2023; Bresciani et al., 2014; Bresciani, Goderniaux, et al., 2016). These insights have laid a strong

foundation for conceptual studies, simplifying the initial response of water table elevations to the three principal drivers.

1.3. Groundwater surface water interactions

The interaction between groundwater and surface water serves as a key indicator for deciphering the mechanisms of groundwater flows in the mountain block and the complex relationship between MBR and sMFR. These interactions, often evidenced by areas where the water table intersects with the topography, are direct indicators of the water table elevation (Bresciani et al., 2014; Bresciani, Goderniaux, et al., 2016; Cornette et al., 2022; Sophocleous, 2002). Known as seepage areas, they significantly influence mountain catchments by maintaining the continuity of surface water bodies like streams and wetlands (Brunner, Simmons, et al., 2009; Brunner et al., 2017; Devauchelle et al., 2012; Kløve et al., 2011; Leibowitz et al., 2018; Winter, 1999) and affecting geochemical conditions through the mixing of groundwater and surface water in groundwater dependent ecosystems (Kolbe et al., 2016; Soulsby et al., 2007; Tiwari et al., 2017; Weyer et al., 2014).

Groundwater-surface water interactions are closely tied to water table levels, with seepage areas typically forming in topographic lows. As discussed in earlier sections, various factors impact water table elevation and consequently the length and organization of flow paths. For instance, catchments with significant seepage areas are indicative of a generally high water table that interacts with the topography, thereby promoting local flows. In contrast, a catchment with a low proportion of seepage areas suggests a lower water table that barely intersects with the topography, thus favoring regional flows. This makes seepage areas a critical factor in assessing and differentiating the contributions of MBR and sMFR in catchments.

1.4. Research questions and hypotheses

Given the presented current state of knowledge, it is increasingly vital to thoroughly comprehend recharge processes, including MFR and MBR, along with the boundary conditions of lowland basins for an improved evaluation of water resources. This holds especially true in arid and heavily exploited catchments, which are often significantly

reliant on MFR, particularly in the face of the ongoing climate crisis. Consequently, there is an urgent need to refine the accuracy of MBR estimations, which so far have ranged from indicating a minimal contribution (around 5%) to a substantial impact (up to 50%) on basin-fill recharge (Markovich et al., 2019). This leads to the following questions:

i. How the three main drivers - topography, climate, and geology - influence groundwater flows in mountainous context?
ii. How they conjointly influence the spatial distribution of MBR (regional vs local flows)?
iii. Does a specific driver exert a greater relative influence on groundwater flow in given environments, especially arid regions? And finally
iv. How can a better understanding of these key drivers assist in achieving a more precise estimation of MFR and its relationship to MBR?

The working hypotheses defined in this research project, are various and depend on the described groundwater flows drivers, on the MBR estimation and on the interaction between groundwater and surface water flows. A first general hypothesis linking hydraulic conductivity (K) and average recharge rate (R) is proposed, followed by hypotheses based on topographic and geological heterogeneities.

Given the complexities in disentangling the individual effects of various drivers on groundwater dynamics, this study hypothesizes that the elevation of the water table is predominantly determined by the ratio K/R. It is proposed that in scenarios where the K/R ratio is lower, the water table is primarily controlled by topography, leading to an increased occurrence of local and intermediate flow paths. Conversely, in cases where the K/R ratio is higher, the water table is likely to be recharge-controlled, resulting in a deeper water table associated with more regional flow patterns.

The topography wavelength λ_T has a critical control on the partitioning between MBR and the runoff, Q(x), which is a marker of the interaction between surface flow and groundwater flow. A longer topography wavelength will cause a bigger proportion of regional flows and then a bigger proportion of MBR in the total MFR. That said, in the case of a shorter topography wavelength (more incised valleys), local flows

perpendicular to the valleys will be the majority compared to other groundwater flows. This means that more groundwater will contribute to the sMFR and Q(x), and that Q(x)>MBR.

K(x) the hydraulic conductivity controls the active depth of groundwater flows and therefore also controls the stream discharge Q(x). On one hand, applying a constant recharge rate over the basin, Q(x) will significantly increase (>90% of MFR) if the mountain block presents low values of hydraulic conductivity ($K(x) < 10^{-8}$ m/s) limiting the active depth of groundwater flows. On the other hand, high values of K(x) ($>10^{-8}$m/s) in the mountain block will increase the active depth of groundwater flows. This means a bigger proportion of MBR over sMFR (Q(x)) that can reach 50% of the total MFR.

1.5. Main and specifics objectives

The main objective of this study is to get a better understanding of the groundwater flows in mountainous contexts and its relationship with the lowland basins. The specific objectives (SOs) are:

(SO1) Proposing conceptual hydrogeological models that relate the three drivers of groundwater flows with the available data of the study site and with well-known conceptual models from literature (Markovich et al., 2019; Toth, 1963).

(SO2) Establishing criteria for model parameterization such as topography resolution or heterogeneity representation along with an accuracy-cost trade-off in the numerical estimation of the MBR, and

(SO3) Quantifying the MFR-MBR partitioning and its influence on the flow scales generating MBR (local vs regional) and reducing the uncertainty of MBR estimation.

2. METHODOLOGICAL APPROACH

To tackle these questions and achieve the proposed goals, the methodology is anchored in complementary pillars: numerical modeling of groundwater flows and a multidisciplinary field study. This strategy, combined with hydrogeological interpretation and conceptualization, enables the presentation of an integrated work that encompasses a broad spectrum of numerical and field observations. Although this study is not tied to a single case, observations were primarily conducted in Central and Northern Chile to contextualize the study. The subsequent sections provide an overview of this region's geomorphological and climatic context, along with the approach used for both numerical and field studies. Lastly, a connection is established between the thesis objectives and the ensuing chapters, which comprise three original research papers.

2.1. North-Central Chile geomorphological and climatic context

The considered area is located along the whole width of Northern and Central Chile between Santiago and Arica (~ 1,800 km long) (Figure 2-1). It is an idoneous location for this investigation, presenting a wide range of climatic, topographic, and geological conditions. This section will be focused on characteristics useful to this study.

The geomorphological features of the studied region are shaped by the formation of the Andes mountain range induced by the subduction of the Nazca Plate beneath the South American Plate (*e.g.,* Coira et al., 1982; Yáñez & Cembrano, 2004; among others). These tectonic settings lead to the creation of three major geomorphological units: the Central Depression, flanked by the Coastal Cordillera and the Principal Cordillera, both mostly composed of volcano-sedimentary rocks (Hartley & Evenstar, 2010; Jordan et al., 1983).

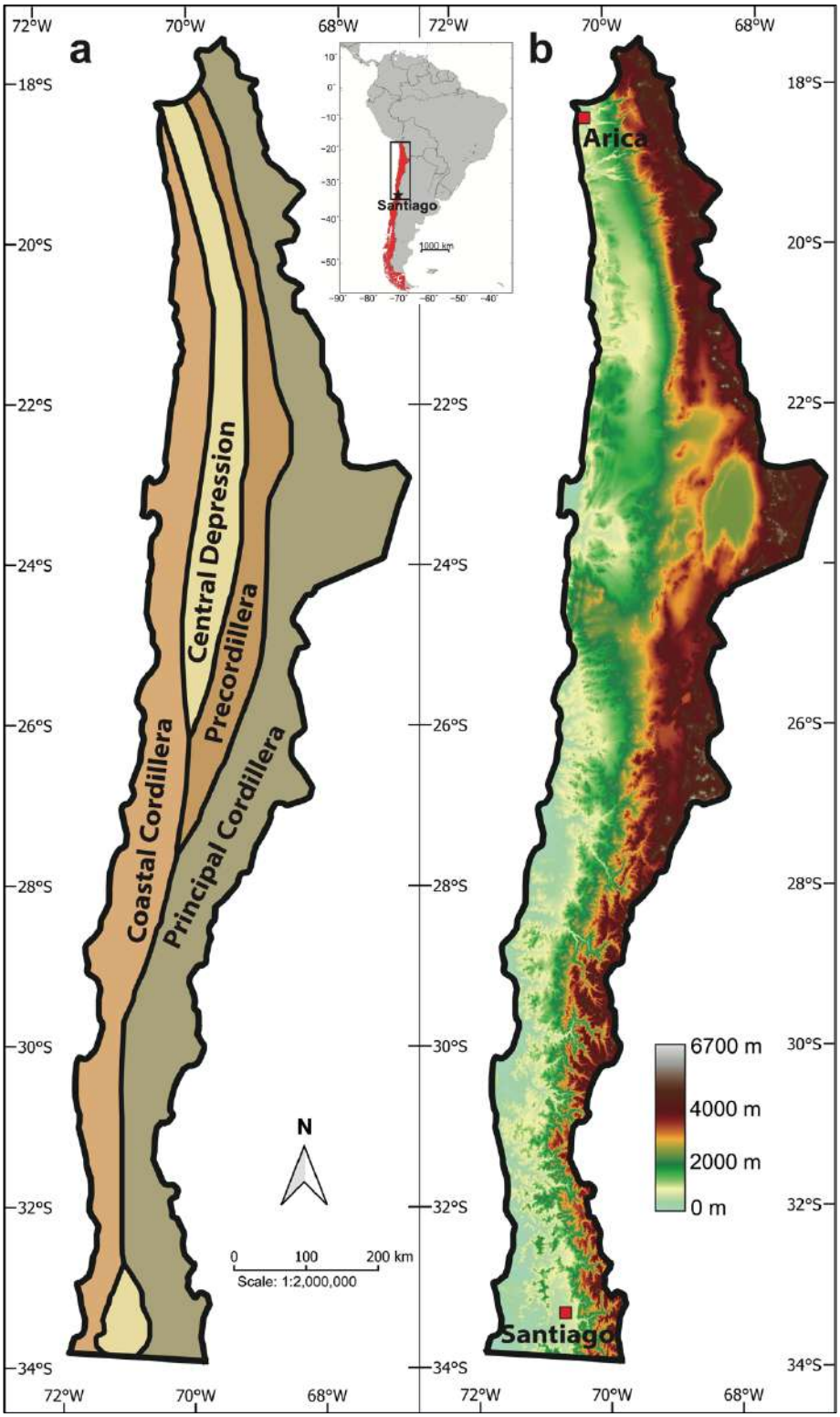

Figure 2-1 a) Morphological settings along the North of Chile. b) Topographic map of Northern Chile (from SRTM data (Farr et al., 2007).

The Coastal Cordillera has elevations between 1,000 and 2,000 meters above sea level, whereas the Principal Cordillera reaches peaks close to 7,000 meters (Armijo et al., 2015; Charrier et al., 2007). The Central Depression itself is a sedimentary basin filled with Quaternary alluvial deposits of varying thickness (Suárez et al., 2021), extending from about 250 meters near Santiago to nearly 1,000 meters in northern Chile (Hartley & Evenstar, 2010; Jordan et al., 2014; Nester & Jordan, 2011). Finally, the Precordillera acts as a transition zone between the Central Depression and the Principal Cordillera. This diversity offers a rich field for exploring various topographical features, from flat catchments and mountain fronts to high mountain peaks particularly useful to this investigation.

The active orogenic processes in these regions significantly influence the defined geomorphological areas, with major faults and structures. The subduction process leads to significant crustal shortening, creating predominant North-South-oriented faults within the mountain block and along the mountain front. These faults act as critical geological boundaries, separating the Central Depression from the Principal Cordillera (Reutter et al., 1996; Santibáñez et al., 2018; Yáñez et al., 2020; Yáñez & Herrera, 2019). Their orientation is especially significant in terms of groundwater dynamics, as they can potentially influence the groundwater flow, which predominantly follows an east-west gradient from the Principal Cordillera towards the lowland areas. This orientation and the resultant structural features can thus play a pivotal role in reshaping recharge and directing and modifying groundwater flow patterns in these complex geological settings.

The climatic conditions in this region vary from hyper-arid to semi-arid from north to south. The northern area, particularly the Atacama Desert (18°S-29°S), is one of the driest places on Earth. Yet, this region also contains significant lowland aquifers, such as the Pampa del Tamarugal situated between 20°S and 21°S in the Central Depression. Despite receiving minimal direct precipitation (< 10 mm/year) (Houston, 2006), this aquifer remains a crucial water source for the area (Viguier et al., 2018, 2019). Its strategic location, nestled between the Coastal Cordillera to the west and the Principal Cordillera to the east, enables it to capture MFR from the Principal Cordillera, which receives approximately 200 mm of precipitation annually (R. Garreaud et al., 2003; Houston, 2006). This precipitation is highly seasonal, occurring mainly between

December and March, known as the austral summer (R. Garreaud et al., 2003; Houston, 2006).

Further south, in Central Chile (~33°S), the historical average precipitation is about 260 mm per year in the Central Depression and around 700 mm in the Principal Cordillera (DMC, 2023). Here too, precipitation is seasonally concentrated, predominantly occurring in the Austral Winter between June and September (R. Garreaud, 2009). However, since 2010, Central Chile has experienced a continuous and severe drought known as the "Megadrought," leading to an approximate 30% reduction in regional precipitations (Aceituno et al., 2021; Alvarez-Garreton et al., 2021; R. Garreaud et al., 2020; R. D. Garreaud et al., 2017).

In both northern and central areas, the interannual climate and precipitation patterns are significantly influenced by the El Niño–Southern Oscillation (ENSO), a common feature across South America (Cai et al., 2020). Interestingly, the impact of ENSO varies between these regions. In the hyper-arid north's Principal Cordillera, precipitation increases during La Niña events (R. Garreaud & Aceituno, 2001), while in Central Chile, El Niño events typically bring increased rainfall (Montecinos & Aceituno, 2003).

2.2. Numerical approach

Numerical models are valuable in representing and understanding phenomena that are not directly observable, such as groundwater flow systems. These models not only elucidate the functioning of such systems but also enable predictions of their future behavior (Anderson et al., 2015). They facilitate the identification of the impact of various parameters on simulated hydrogeological processes via sensitivity analyses and serve as essential tools for effective groundwater management and forecasting. Two modeling approaches in this field are conceptual studies (Bresciani et al., 2014; Carlier et al., 2019; Gleeson & Manning, 2008; Rapp et al., 2020; Schilling et al., 2021) and site-specific calibrated models (Ball et al., 2014; Blin et al., 2022; Ping et al., 2021; Thornton et al., 2022; Yao et al., 2015, 2017).

Site-specific modeling is intensely data-based, aiming to accurately depict the specific conditions of a chosen location (Kresic, 2006). This method entails gathering extensive data on groundwater levels, flow rates, and hydrogeochemical attributes pertinent to the

site. Calibration is a vital part of this approach (Hill & Tiedeman, 2007; Kresic, 2006; Moore & Doherty, 2006), involving the adjustment of model parameters until the outputs align closely with actual observations. Such rigorous calibration ensures the model reliability in representing the distinct hydrogeological characteristics relevant to a specific site (Carrera et al., 2005; Linde et al., 2015). In such a modeling approach, the output is generally a unique calibrated model from which observations are done and decision made.

Conversely, conceptual modeling takes on a wider perspective, seeking to simplify and generalize the complexities of hydrogeological systems. This approach prioritizes understanding fundamental processes and patterns over the detailed accuracy of a particular site. Conceptual models are key to investigating general hydrogeological phenomena and hypothesizing about system behaviors under various scenarios, thereby contributing to the understanding of broader hydrogeological processes and eventually theories. In such a process-based modeling approach, the model may not be calibrated or only partly calibrated and merely an instance among many more possible. If the first approach is historically more common, the equifinality of models (Beven, 2001; Moore & Doherty, 2006; Troldborg et al., 2007) promoted the development of *metamodeling*, a new paradigm in which decision is made based on a representative combination of models obtained by screening a wide range of hydrogeological conditions (Christelis & Hughes, 2018; Fienen et al., 2015, 2016; Starn & Belitz, 2018).

In the context of this study, and considering the aforementioned approaches, the challenges arise from two main aspects: firstly, the scarcity of data in mountainous regions complicates the calibration of groundwater flow models. Secondly, the reliance on synthetic scenarios in conceptual studies introduces limitations due to their inherent assumptions, potentially reducing their applicability to real-world contexts. These factors highlight the need for a balanced approach that navigates between the granular details of specific sites and the broader generalizations of conceptual modeling.

Therefore, in this work, the proposed approach is at the crossroad between these two common aspects of groundwater modelling. It employs real-world topographical data or field-based geological features in numerical experiments to enhance our understanding of hydrogeological systems at large. This methodology allows for the dissection of each

driver's impact on groundwater flow. By setting physically consistent values for some parameters, we can conduct sensitivity studies on the remaining drivers, thus gaining insights into their direct effects across a range of scenarios.

2.3. Field approach

Field studies in hydrogeology are essential for understanding the complexities of groundwater systems, enabling researchers to gather real-world data on aquifer characteristics and water movement. These data can then be confronted to numerical model results to obtain a full understanding of groundwater systems.

In mountainous regions, where continuous data collection is often challenging, localized field studies are crucial in bridging data gaps. Due to the limited availability of direct observation methods like monitoring and pumping wells, indirect techniques are commonly employed. Methods such as hydrogeochemical analysis, stable isotope examination, and the use of environmental indicators, including noble gases and human-derived tracers, have traditionally been used to trace groundwater flow paths and sources in these catchments (Baraer et al., 2015; Gardner et al., 2020; Hilberg, 2016; Manning & Solomon, 2005; Oyarzún et al., 2015; Pincetti-Zúniga et al., 2022; Taucare et al., 2020; Wilske et al., 2020).

Additionally, hydrogeophysics is becoming increasingly valuable for its non-intrusive assessment of physical parameters linked to hydraulic conductivities (Binley et al., 2015; Robinson et al., 2008). Although implementing hydrogeophysical techniques in mountainous terrain can be challenging due to terrain conditions, the results are often enlightening (Ball et al., 2010; Figueroa et al., 2021; Glas et al., 2019; McClymont et al., 2011; Pérez-Estay et al., 2022; Vignoli et al., 2012; Vittecoq et al., 2019).

Yet, the need for studies that integrate a wide array of observations is becoming increasingly urgent. The constructive interaction of different methodologies and interdisciplinary collaboration greatly enhances the overall understanding of hydrogeological systems (Christensen et al., 2020; Manning et al., 2021; Markovich et al., 2021; Ruiz Pereira et al., 2023; Somers et al., 2016).

The methodology developed in this study, as detailed in Chapter 4, adopts an iterative and collaborative approach. It combines hydraulic and geological data (field geology and geophysics) to create a comprehensive hydrogeological conceptual model. Field campaign designs were tailored to the project's specific needs and evolved as results from various disciplines were integrated. The focus was on characterizing hydraulic singularities and adapting geological investigations to specific areas rather than attempting to describe an entire catchment. This innovative approach is crucial for developing effective methods to understand hydrogeological processes in mountain contexts, considering the challenges posed by their remote locations.

2.4. Establishing a link between presented publications and specific objectives

Chapter 3, the initial study of this thesis, adheres to the letter format of brief communications, emphasizing concise yet significant findings. It investigates the influence of topography on groundwater flows, particularly the interactions between groundwater and surface water. Additionally, it examines the response of aquifers to various degrees of desaturation under different climatic conditions. This numerical analysis serves as a framework for understanding key groundwater drivers in mountainous areas (SO1) as well as establishing criteria to describe complex topography in a more straightforward manner (SO2). This study extends across 60 catchments over 1,800 km in Northern and Central Chile, offering a comprehensive global perspective.

Chapter 4 details a multidisciplinary field study conducted in a specific catchment south of Santiago, Chile. This collaborative effort yields insights into how defining geological structures can elucidate the hydrogeological functioning of a mountain catchment (SO1). A novel field methodology is employed to identify geological heterogeneities that affect groundwater and surface water interactions, laying the groundwork for developing hydrogeological criteria to assess their impact (SO2).

Finally, Chapter 5 presents numerical simulations conducted on the same catchment as the field study. Using observations from chapter 4 on geological structures, such as faults and fractures, and calibrating the homogeneous model based on the K/R ratio defined in chapter 3, it proposes a sensitivity study on the permeability of such structures. It is anchored in the numerical approach defined above, using real case catchment topography

and structure's location while defining the impact of a varying hydraulic conductivity on flow paths. Among the various metrics studied is the characterization of sMFR and MBR to give a first approximation of these important parameters in mountain systems (SO3). It also explores criteria for fault zone permeability and its impact on groundwater flows (SO2).

Together, these three studies contribute to understanding groundwater flows in mountainous regions at varying scales, employing complementary methodologies to create a comprehensive body of research.

3. FROM LOWLANDS TO MOUNTAIN PEAKS: IMPACTS OF LANDFORMS ON THE DESATURATION OF GROUNDWATER-DEPENDENT WETLANDS

3.1. Introduction

Groundwater seepage occurs when the water table intercepts the topography, hence features and forms of the landscape impact groundwater seepage distribution (Bresciani et al., 2014; Bresciani, Goderniaux, et al., 2016; Cornette et al., 2022; Sophocleous, 2002). Streams, wetlands, springs, and other surface water bodies, often reflect groundwater seepage distribution and depend on its perennity (Brunner, Simmons, et al., 2009; Brunner et al., 2017; Devauchelle et al., 2012; Leibowitz et al., 2018; Scanlon et al., 2023). Climate change is expected to reshape groundwater recharge and seepage areas, possibly with more intense, more frequent and more extended droughts (Amanambu et al., 2020; Dai, 2013; Gleick, 1989; Pokhrel et al., 2021; Scibek et al., 2007; Viviroli et al., 2011).

Topography, hydrodynamic properties of the aquifer (hydraulic conductivity K), and recharge rate (R) stand as the main drivers of groundwater flows architecture, water table depth and thus seepage areas distribution (Condon & Maxwell, 2015; Cuthbert et al., 2019; Gleeson et al., 2011; Goderniaux et al., 2013; Schaller & Fan, 2009; Tóth, 1963; Zhang et al., 2022). A certain equivalence of effects between R and K has been evidenced (Bresciani et al., 2014; Haitjema & Mitchell-Bruker, 2005; Jamieson & Freeze, 1982) allowing to conveniently focus on the dimensionless R/K ratio and the topography. Nevertheless, the characterization of the impact of topography remains a more intricate endeavor. Water table is intuitively close to the surface in regions of lower relief and/or humid regions and deepens in rugged terrains and/or arid regions. Still, the hydrogeological response and seepage dynamics to the variety of landscapes and their corresponding topographical attributes is far from straightforward.

Two-dimensional analytical solutions have been proposed to estimate seepage length at the hillslope scale, or water table outcrops at the cross-section scale (Bresciani et al., 2014; Bresciani, Goderniaux, et al., 2016). Nevertheless, these solutions are based on the Dupuit-Forchheimer assumption and limited to a constant slope hillslope or to a

longitudinal elevation profile along a cross section. Marçais et al. (2017) developed a seepage estimation model at the hillslope scale in 2D deriving an equivalent hillslope representing the main topographical features of the catchment. Albeit improving the hillslope representation, it does not render the complexity emerging from the 3D nature of groundwater flow. A few topographical 3D models have been developed mainly aiming at supporting sensitivity studies (Carlier et al., 2019; Gauvain et al., 2021; Gleeson & Manning, 2008; Welch & Allen, 2012). Still, their parametrization (hillslope complexity, boundary conditions, arbitrary scale, etc.) remains limiting. Consequently, a pressing requirement emerges for the development of 3D seepage distribution models that consider the intricate topographical nuances inherent in real-world conditions to provide more accurate predictions of seepage area development.

We aim at quantifying which topographical features of landscapes strongly controls the evolution of groundwater seepage areas under different groundwater saturation regimes. This pursuit is intricately directed towards discerning identifiable features and patterns in topography that wield notable influence over hydrogeological responses in complex environments. In fine, we aim at proposing topographical indicators that adeptly capture the intricate variations inherent in geomorphological settings. Our approach involves the utilization of parsimonious 3D numerical models at regional scale (~ 1,000 km^2) with open boundaries to unarbitrary simulate groundwater flow under complex topographies. We deployed those models on 60 catchments along the 1,800 km of the northern Chilean Andes. The choice of the Andean Mountain range was motivated by its rich diversity of geomorphological contexts. The similarities with other orogenic structures offer the potential to extend our findings to other study areas.

3.2. Material and methods

3.2.1. Geomorphological context

The study area is located along the whole width of Northern Chile between Santiago and the Peruvian border (~ 1,800 km long). The geomorphological characteristics in the region are a result of the Andes formation due to the ongoing subduction of the Nazca Plate beneath the South American Plate. This process led to the formation of a longitudinal valley called the Central Depression demarked by two cordilleras, the Coastal Cordillera and the Principal Cordillera both composed mainly by volcano-sedimentary rocks (Hartley & Evenstar, 2010; Jordan et al., 1983). The Coastal Cordillera forms an intermediate mountain range with an average elevation between 1,000 and 2,000 m.a.s.l., while the principal Andes Cordillera boasts maximum peak elevations close to 7,000 m.a.s.l (Figure 3-1a) (Armijo et al., 2015; Charrier et al., 2007). The Central Depression delineates a sedimentary basin replete with Quaternary alluvial deposits, exhibiting varying thicknesses, from approximately 250 meters near Santiago (Yáñez et al., 2015) to nearly 1,000 meters in the northern regions of Chile (Hartley & Evenstar, 2010; Jordan et al., 2014; Nester & Jordan, 2011). Specifically, the Precordillera has a typical mountain front geomorphology as it is the transition zone between the Central Depression and the Western Cordillera with catchment characteristics varying from nearly flat terrains to mountainous regions with steep slope gradients (Figure 3-1a). The diversity of these environments presents an excellent opportunity to explore a wide variety of topographical settings, including flat catchments, mountain front areas, incised mountain catchments, volcanoes, and high mountain peaks.

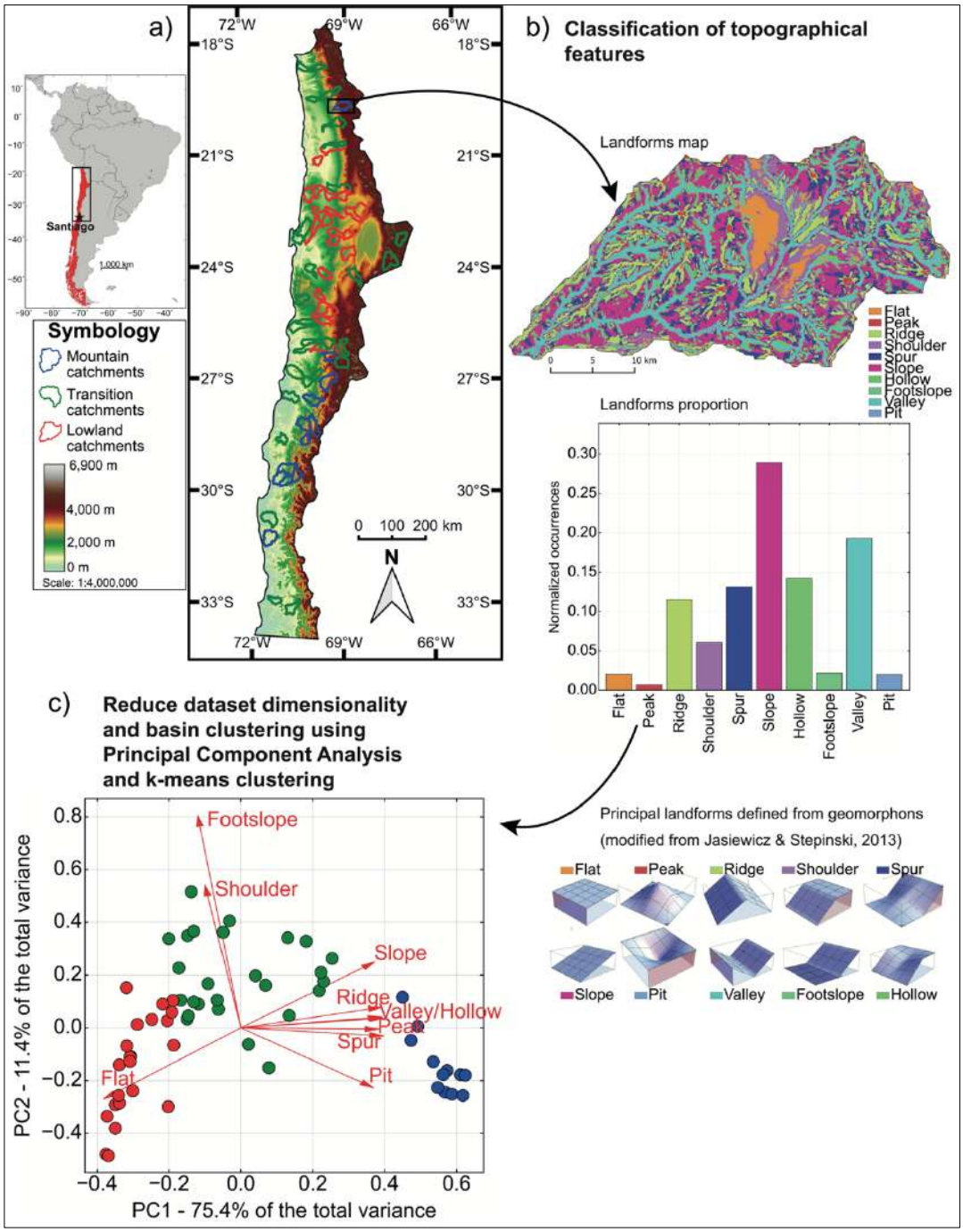

Figure 3-1 Workflow for topographical classification: a) Situation and topographic maps of the study area in which the 60 studied catchments are delimited by a colored line. The color scheme corresponds to the three clusters obtained after applying the classification methodology (section 3.2.2) and is maintained throughout. b) Classification of topographical features exemplified in one catchment: the landforms map, landforms proportion, and a reminder of principal landforms. c) PCA plot, displaying PC2 against PC1 with the percentage of variance in the dataset explained by each component. Each red arrow represents the landform eigenvectors.

3.2.2. Classification of catchment topographies

We consider the catchment boundaries of HydroATLAS global catchments database (Lehner & Grill, 2013). We chose to work at sub-regional scale, constraining the size of the catchments to fall within the range of 500 and 1,500 km^2. Covering diverse geomorphological and tectonic settings, we identified a total of 60 catchments within our study area (indicated by colored boundaries in Figure 3-1a) for which we extracted the topography based on the digital elevation model (DEM) from the SRTM (Shuttle Radar Topography Mission, 90 m resolution).

The geomorphons classification proposed by Jasiewicz & Stepinski (2013) presents a landscape description approach by categorizing the terrain into ten distinct landforms, listed in Figure 3-1b, based on elevation differences in eight directions relative to the reference cell. This operation is reproduced for each cell of the DEM, identifying a form for each of these cells (Figure 3-1b). Unlike direct cell neighbor's method (e.g., slope, curvature or roughness), the geomorphons method allows us to define a search radius (look-up distance) around the reference cell, capturing landforms at larger scales. To capture hillslope-scale landforms, the look-up distance is defined here as the catchment characteristic length L as estimated from the drainage density D formula:

$$L = \frac{1}{2D} \rightarrow L = \frac{1}{2 * \frac{l}{A}}, \qquad \text{Equation 3-1}$$

with l the river network length in the catchment and A the catchment area. The river network is defined using a surface flow accumulation routine available in the Whitebox tool Python package (Lindsay, 2016). We combined Principal Component Analysis (PCA) and k-means clustering (Figure 3-1c) to explore the catchments by their dominant topographical characteristics based on landforms proportions (Figure 3-1b) and categorize the landscape patterns found in the dataset. PCA reduces the dataset to two dimensions PC1 and PC2 while a k-means clustering approach identifies groups of catchments with topographical similarities (Figure 3-1b and c).

3.2.3. Numerical modelling of seepage area

To investigate the influence of topography on groundwater flows and seepage distribution, a three-dimensional numerical groundwater flow model is developed for each catchment. The models are built and run with MODFLOW-2005 software suite (Harbaugh, 2005) with the NWT solver (Niswonger et al., 2011) and handled with the Python-based interface FLOPY (Bakker et al., 2016).

The horizontal discretization follows the DEM resolution, i.e., 90 meters (Figure 3-2a) while the vertical one is composed of ten layers with exponentially increasing thickness (Figure 3-2b). The modeled area includes a buffer zone around the catchment, increasing the modeled domain area by 20%, thus preventing any potential impact of boundary conditions on seepage distribution within the studied catchment (Figure 3-2a). The model bottom is flat (Figure 3-2b) and set as:

$$Bottom = E_{min} - 0.5 * (E_{max} - E_{min}), \quad \text{Equation 3-2}$$

where E_{min} and E_{max} the minimum and maximum altitudes in the catchment, respectively (Figure 3-2b). A flat bottom is employed to mitigate the influence of high topographic gradients that could affect regional groundwater flow with constant thickness depth (Gleeson & Manning, 2008). This value was then chosen to allow for deep flows (Ball et al., 2014; Yao et al., 2017) while limiting computational times. The side and bottom boundaries of the buffer box are set as no-flows. Potential recharge is set uniformly at the water table and a drain is set on the topography using the eponym packages in Modflow, which conjointly allows the water to either infiltrate (recharge) or exfiltrate (seepage) at the surface. To focus solely on topographic effects, hydraulic conductivity K is set homogeneous and isotropic. We consider 25 logarithmically spaced values of $\frac{K}{R}$ ranging from 10^{-2} to 10^{2} allowing us to simulate humid to arid conditions (Figure 3-2c), i.e., by exploring various water table positions with respect to the topography. The diffusivity equation is solved in steady-state conditions. In total, 1,500 models were simulated, considering 60 catchments and 25 different $\frac{K}{R}$.

To enhance the quantitative analysis and capitalize on the characteristic "inverse S" shape of the seepage vs log ($\frac{K}{R}$) relationships, we perform a power law fit of seepage area for each catchment, further mentioned as the desaturation function (red curve on Figure 3-2c):

$$normalized\ seepage\ area\ = \left(1 + \left(\frac{\frac{K}{R}}{\lambda}\right)^2\right)^n . \qquad \text{Equation 3-3}$$

Indeed, the evolution of normalized seepage area regarding $\frac{K}{R}$ is representative of catchment desaturation. The desaturation function is driven by the desaturation threshold λ, i.e., the critical $\frac{K}{R}$ value at which catchment saturation decreases, and the desaturation rate n beyond λ. n being negative, the lower n, the fastest the desaturation and inversely.

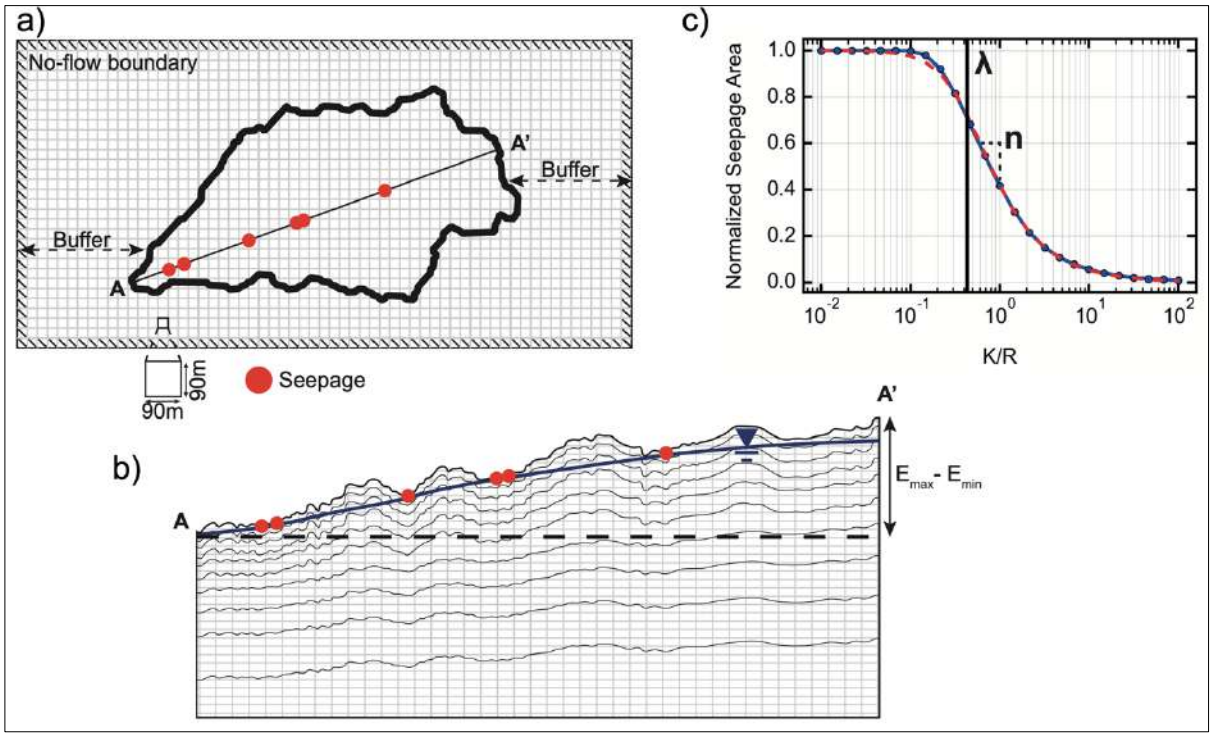

Figure 3-2 Model features for one example catchment: a) Horizontal discretization and buffer zone beyond catchment limits, b) AA' cross-section including vertical discretization and an arbitrary water table intercepting the topography creating seepage areas (red dots), c) Sensitivity study results (blue dotted curve) with the power law fit (dashed red curve).

3.3. Results

3.3.1. Typology of catchments topography

The PCA performed on the landforms of our 60-catchment dataset (Figure 3-1c) resulted in a first component (PC1) explaining 75.4% of the total variance, and the first two components (PC1 and PC2) combined explaining 86.8% of the total variance. This indicates a strong relation between the landforms description in the catchments and the reduction into 2 dimensions. PC1 is mostly controlled by the flat and slope landforms, with eigenvector magnitudes of -0.4 for the flat landform and 0.4 for the slope landform. Along PC1, slope landform is associated to the peak, ridge, valley, hollow, spur, and pit forms, all showing 0.4 eigenvectors magnitudes. Regarding PC2 the footslope and shoulder forms are the main control with an eigenvector magnitude of respectively, 0.8 and 0.5. Flat and slope forms show eigenvectors magnitudes of -0.2 and 0.2 along the PC2 axis.

To further support and illustrate this description, the catchments are grouped into three clusters (colored dots in Figure 3-1c and colored catchments contour on Figure 3-1a). The red cluster is highly influenced by the flat landform as lowland catchments would. Conversely, the blue cluster is strongly influenced by slope and associated landforms (ridge, valley, peak) representative of mountain catchments with incised valleys, and narrow valley bottoms. The green cluster exhibits more dispersion in the represented catchments. This cluster acts as a transition between the red and blue clusters. It contains catchments most influenced by footslope and shoulder forms. Positioned centrally between the two extreme clusters, this cluster serves as a transition zone between flatter areas and mountain catchments, possibly including catchments showing both flat and mountainous characteristics, as observed at mountain fronts.

To facilitate comprehension and illustration, these clusters are referred to as *lowland catchments cluster* for the red cluster, mountain catchments cluster for the blue cluster and *transition catchments cluster* for the green cluster thereafter.

3.3.2. Seepage distribution evolution with increasing $\frac{K}{R}$

Figure 3-3a illustrates the evolution of seepage area, normalized by the catchment area, as a function of $\frac{K}{R}$ for all 60 catchments. Four specific catchments are highlighted with sharper lines for further discussions. As expected, lower $\frac{K}{R}$ values result in fully saturated catchments, while as $\frac{K}{R}$ increases, all catchments progressively desaturate according to a wide range of rates. For instance, at a normalized seepage area of 20%, the corresponding $\frac{K}{R}$ values range from 0.5 to 70.

Like the clear definition of landforms clusters, the distinct desaturation behavior of the clusters stands out (Figure 3-3), confirming that the variations in seepage distribution are predominantly driven by topographical effects. On the one hand, the *mountain cluster* shows lower critical $\frac{K}{R}$ values and exhibits faster desaturation rates. On the other hand, the *lowland cluster* shows higher critical $\frac{K}{R}$ values and presents slower desaturation rates. The *transition cluster* demonstrates intermediate behavior, reaching higher critical $\frac{K}{R}$ values than the *mountain cluster* but lower critical $\frac{K}{R}$ values than the *lowland cluster*. The variability in desaturation slopes for the *transition cluster* is more pronounced, causing a mixing of various behaviors within this zone.

The power law fit of seepage distribution (Equation 3-3) for each of the 60 catchments results in λ ranging between 0.29 and 8.19 and n ranging between -0.50 and -0.18 (λ and n for all catchments are presented in Supplementary Material). The fit presents minimal RMSE values between 0.003 and 0.034 indicating that seepage evolution with increasing $\frac{K}{R}$ can be parameterized with only two parameters, λ and n.

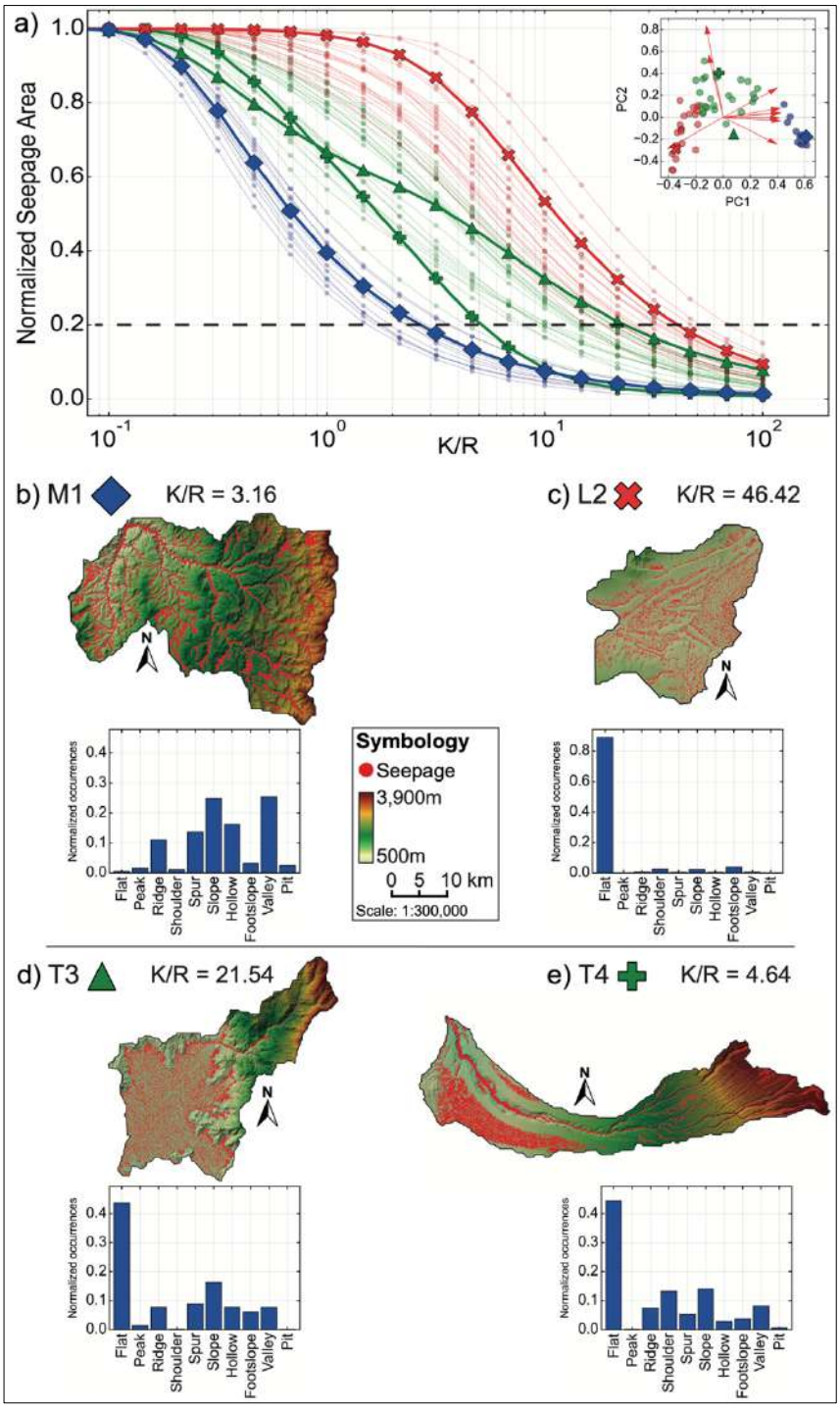

Figure 3-3 a) Normalized seepage area against K/R for the 60 catchments (colored lines with markers), including PCA results on the upper-right corner. Four illustrative catchments are highlighted: mountain type M1 (blue diamond, b)), lowland type L2 (red cross, c)), transitory type T3 (green triangle, d)) and T4 (green cross, e)). Details include the topographic map overlayed by the seepage area at an arbitrary value of 20% (red mask) with corresponding K/R value followed by the landforms histogram.

3.3.3. Seepage patterns in representative catchments

Figure 3-3 spotlights four distinct catchments, M1, representative of the *mountain cluster*; L2, representing the *lowland cluster*; and T3 and T4, serving as outliers within the *transitory cluster*. We present the seepage distribution over the topographic map and the landforms proportion for each catchment (Figure 3-3b, c, d, and e).

In the case of M1 (Figure 3-3b), characterized by low λ and n values, it exhibits the hallmark seepage distribution of mountainous regions. At a normalized area of 0.2, seepage primarily congregates in topographic lows, i.e., river valleys, while ridges and peaks undergo desaturation due to their substantial elevation compared to the surrounding terrain. Conversely, L2 (Figure 3-3c), featuring high λ and n values, suggests that the water table remains in closer proximity to the topography in lowland settings.

Regarding the outliers T3 and T4, their landforms proportion (Figure 3-3d and e) reveal similar values for most forms, except for a higher proportion of shoulder and footslope forms in T4. This heightened prevalence of the shoulder landform in T4 is attributed to a prominent incised river valley situated in the eastern part of the catchment.

Delving into T3's seepage distribution, it initially aligns with the *mountain cluster* with low desaturation threshold (λ). Then, in the range of $1 < \frac{K}{R} < 10$, a substantial change in slope is observed, with the distribution intersecting that of the *lowland cluster* for high $\frac{K}{R}$ values. This behavior can be explained looking at the spatial distribution of seepage for T3 (Figure 3-3d). A clear demarcation exists between the flat western area and the mountainous settings to the east. At higher elevations, desaturation occurs for lower $\frac{K}{R}$ values, resulting in a low value of desaturation threshold (λ). Subsequently, for a normalized area of 0.2, the catchment behaves like the *lowland cluster* under the influence of the western part of the catchment.

Conversely, T4's seepage distribution exhibits an opposing pattern, initially mirroring the behavior of the *lowland cluster* with a higher λ value, then shows a quicker desaturation rate (n), ultimately resembling the characteristics of the *mountain cluster* (tending toward zero). Seepage spatial distribution for T4 (Figure 3-3e) shows that higher elevation zones have already undergone desaturation (in the western part of the

catchment) and tends to develop exclusively within topographic lows, specifically at the bottom of the singular river channel.

3.3.4. Linking topographic features and desaturation behavior

We computed the correlation matrix between the principal components (PC1 and PC2) and the desaturation parameters (λ and n) to get an appraisal of the strength of the topographical control on desaturation behavior. Figure 3-4a shows the strong anti-correlation between λ and PC1 with a spearman coefficient r equal to -0.98 ($p<0.0001$), while Figure 3-4b shows a good correlation between n and PC2 with a coefficient r equal to 0.53 ($p<0.0001$). No other significant correlation is identified (the entire correlation matrix between all four parameters (λ, n, PC1 and PC2) is available in Supplementary Data).

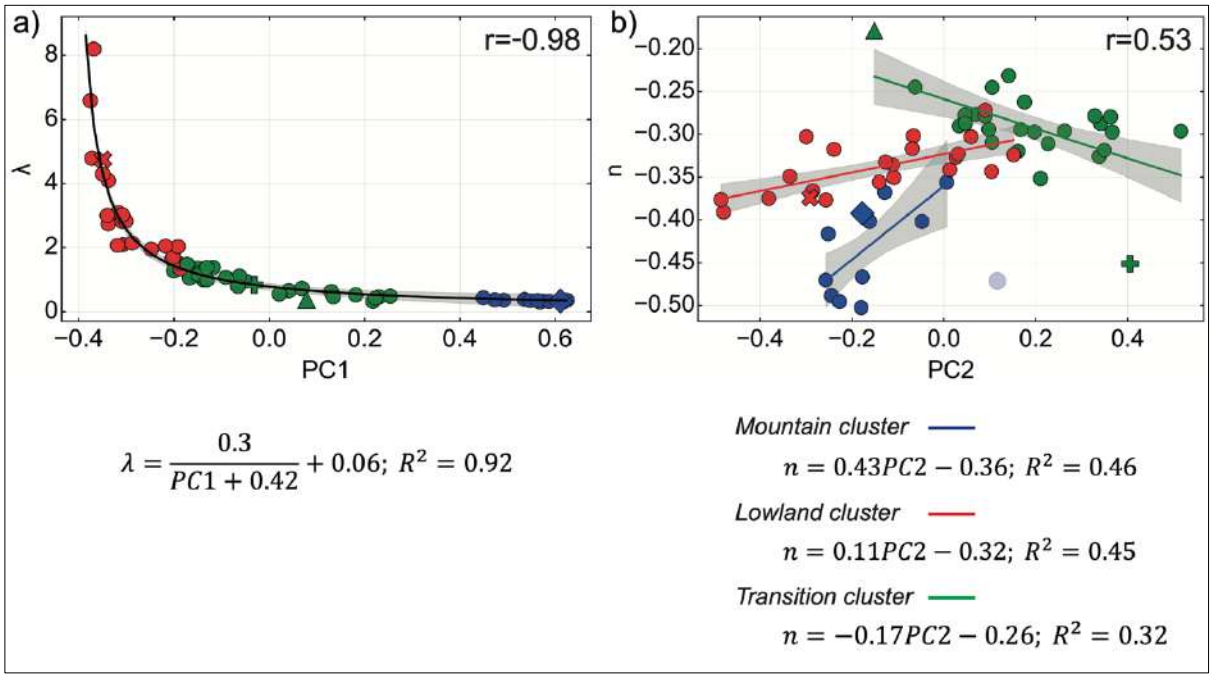

Figure 3-4 Scatter plots for the 60-catchment dataset with spearman correlation coefficient r. a) λ against PC1 including the equation and the coefficient of determination (R2) coefficient of a global fit (black line with 95% confidence interval) and b) n against PC2 including the equations and the coefficients of determination (R2) of cluster-scale fits (colored lines with 95% confidence interval). The transparent mountain catchment point was excluded from the fit.

The clusters on Figure 3-4a are well distinguishable. The *mountain cluster* is isolated with low λ values and small variance on the λ values. The *transition cluster* forms the elbow part of the exponential decay. Finally, the *lowland cluster* is clearly identified as well showing the higher λ values, yet the variations for possible λ values in this cluster are higher. The depicted inverse relationship is further robustly quantified by fitting an inverse function (R^2=0.92) that facilitates a quantitative correlation between λ and PC1, as illustrated in Figure 3-4a. The three clusters reveal more distinctive behaviors in the relationship between n and PC2 (Figure 3-4b), which reasonably prevents from proposing a common fit to the three clusters. Still, linear fitting to each cluster independently yielded satisfactory results as evidenced by R^2 values ranging from 0.32 for the *transition cluster* and 0.45 and 0.46 ($p<0.001$) for the *lowland cluster* and *mountain cluster* respectively. In particular, the *lowland cluster* shows a rapid increase in n as PC2 increase, with a high dispersion along PC2, while the *mountain cluster* displays less dispersion on PC2. In contrast, the *transition cluster* is concerned by high PC2 values, with significant variation in n.

To further explore the relationship between the shape of the desaturation function with the landscape forms, we employed a Random Forest regression on the dataset to predict λ and n based on topographic parameters (PC1 and PC2). This analysis involved 6,500 iterations of sampling with replacement, each using 10 test catchments from a dataset of 60 catchments, with the remaining 50 catchments used for training. This resampling approach was adopted to assess the robustness of the estimations in the presence of random variations within the selected test and training data. We calculated the coefficient of determination (R^2) for the 6,500 iterations to demonstrate the accuracy of the predictions (see supplementary data for Kernel Density Estimate (KDE) plot of R^2 distribution). For the prediction of λ, we obtained an R^2 mean value of 0.87 within a 95% confidence interval defined as [0.87-0.88] and a median value of 0.90. As for n, we obtained an R^2 mean value of 0.40 within a 95% confidence interval defined as [0.39-0.41] and a median value of 0.49.

3.4. Discussion and perspectives

The incorporation of three-dimensional data has greatly enhanced our understanding of catchment topography singularities providing a more comprehensive definition of seepage distribution and groundwater-dependent wetland desaturation. As evidenced by our results, the distribution of seepage areas is primarily influenced by landscape forms, the hydraulic properties of the aquifer and the recharge rates. The slope of the topography (PC1) plays a primary control on the desaturation function for increasing $\frac{K}{R}$ conditions. The footslope and shoulder landforms, *i.e.,* concave- or convex-type (PC2) also plays a critical role in the desaturation function, although its influence is not as straightforward as for the slope.

To better constrain the physical mechanisms involved, we evaluated our results against the ones obtained from a simple hillslope scale analytical solution (Bresciani et al. 2014) (Supplementary Material). Results from our 3D modeling approach exhibit consistency with the analytical solution at high saturation, when the hillslope is the groundwater flow length. It confirms that the slope angle exerts the main influence on the desaturation function defining the groundwater seepage distribution. Steep slopes show low critical $\frac{K}{R}$ values at which desaturation initiates compared to gentler slopes which show higher critical $\frac{K}{R}$ values. Additionally, the 2D shape of the hillslope, whether it is concave or convex in the analytical framework, slightly influences the rate of desaturation with concave hillslope showing slower rates and convex ones showing quicker rates, mostly resembling the influence of PC2 on n. Therefore, the steeper the slope, the quicker the water table will disconnect from the topography as desaturation increases. For similar slopes, the desaturation rate shows a noteworthy effect of the curvature degree of the hillslope, as the water table remains closer to the topography in the concave case.

Our analysis has revealed that steep topographies encompass various features controlling seepage distribution and desaturation functions. These features, such as ridges and valleys, are prominent in mountainous environments. Furthermore, when examining secondary controls, subtle changes are evidenced by the landforms analysis, in overall similar catchment slope (*i.e* similar PC1), explaining differences within the same cluster. This underscores the complexity of defining the hillslope's overall shape and highlights

the influence of abrupt topographic transitions, especially pronounced at the fronts of mountains or within incised valleys, in governing desaturation rate (n). In terms of resilience, mountains emerge as particularly vulnerable due to quick desaturation rates occurring at lower critical $\frac{K}{R}$, which are directly related to the intricate nature of their landscapes, emphasizing the heightened susceptibility of such areas, along with arid regions, to the impacts of climate variability.

Our study has established a robust correlation between topographic parameters, specifically landforms categorized based on the relative proportion of geomorphons (PC1 and PC2) , and the parameters essential for estimating the evolution of seepage areas under varying desaturation (λ and n). These insights open opportunities for estimating seepage evolution based solely on topographic variables. Notably, the remarkably strong inverse relationship between PC1 and λ empowers us to discern the general S-shaped pattern of each seepage distribution curve concerning $\frac{K}{R}$. This allows us to make predictions using machine learning techniques for automated training. While the connection between PC2 and n is somewhat less well-defined, it still presents promising results. The linear fits by clusters (Figure 3-4b) show increasing relation for the *lowland* and *mountain clusters* while the *transition cluster* shows a decreasing trend. This opposite behavior underscores that landscapes retain a level of complexity that defies complete characterization using simpler proxies. Our Random Forest algorithm predictions, although influenced by outliers, remain acceptable.

3.5. Acknowledgments

We acknowledge funding from the Agencia Nacional de Investigación y Desarrollo (ANID) through grant Fondecyt Regular n◦1210221 and Anillo n◦ATE220055.

3.6. Open Research

The HydroATLAS global catchments database is freely available at https://www.hydrosheds.org/hydroatlas. The SRTM Digital Elevation model is available on NASA website (https://www.earthdata.nasa.gov/sensors/srtm). The data used to generate results and figures in this manuscript is publicly available at Marti et al. (2023),

including landfoms proportion, PCA, cluster information, λ and n values, and seepage area distribution for each catchment. Catchments ID correspond to the HydroATLAS identification.

4. UNRAVELLING GEOLOGICAL CONTROLS ON GROUNDWATER FLOWS AND SURFACE WATER-GROUNDWATER INTERACTION IN MOUNTAIN SYSTEMS: A MULTI-DISCIPLINARY APPROACH

4.1. Introduction

Interest in mountain catchments has been growing recently (Markovich et al., 2019 and references within). Mountains serve as water reservoirs for downstream alluvial basins due to the heavy precipitation they receive (Immerzeel et al., 2020; Somers & McKenzie, 2020). More than half of humanity depends on mountain hydrosystems for their water supply (Grêt-Regamey et al., 2012). Snow- and glacier-dominated hydrosystems supply more than one-sixth of the world's population (Barnett et al., 2005). Human dependence on these systems is all the more critical as they are particularly vulnerable to climate change (Beniston, 2003; Huss et al., 2017; Viviroli et al., 2011). Understanding the functioning of mountain blocks and their hydraulic connectivity with anthropized basins downstream is thus critical for water resource management (Kamenik et al., 2001; McDonnell, 2003; Soulsby et al., 2007), as well as for society's resilience to climate change (Hayashi, 2020; Viviroli et al., 2020). Furthermore, mountain catchments constitute preserved spaces and biosphere reserves, in some cases harbouring endemic or native species (Clarke et al., 2008; Freeman et al., 2007; Meyer et al., 2007) and providing various ecosystem services (Egan & Price, 2017).

However, despite their importance, mountain hydrogeological systems remain poorly understood (Bishop et al., 2008) owing to their inherent complexity stemming from significant topographic, climatic, and geological gradients. In particular, the interplay of geology, geomorphology, and climate on groundwater flow and related variables is barely understood (Condon & Maxwell, 2015; Gleeson & Manning, 2008; Winter, 2001): for example, groundwater-flow scale, depth, distribution (Markovich et al., 2019; Roques et al., 2014), and recharge (McCord et al., 1997; Nicolas et al., 2019; Sanford, 2002; White & Burbey, 2007), groundwater-surface water interaction (Brunner, Cook, et al., 2009; Fleckenstein et al., 2010), groundwater timescales (Jasechko et al., 2016), and river ecology and biogeochemistry (Kolbe et al., 2016; Weyer et al., 2014). The

geological heterogeneity of mountain blocks related to multiscale fracturing, lithological discontinuities, weathering, etc., is likely to substantially control groundwater flow as significant gradients of the hydraulic conductivity induce flow anisotropy (Leray et al., 2012, 2013), flow channelling, intercatchment flow (Y. Fan, 2019), and possibly groundwater exfiltration (Bense et al., 2013; Caine et al., 1996; Scibek et al., 2016).

Although studies indicate that geological structures substantially impact groundwater-surface water interaction (Schaller & Fan, 2009) and stream flowrate and regime, most studies have focused on the role of climate and geomorphology (Condon & Maxwell, 2015; Cuthbert et al., 2019; Gleeson & Manning, 2008; Welch & Allen, 2012). The geological complexity of hydrogeological systems strongly impedes the generalization of in situ observations and site-specific results and accordingly limits the development of unified hydrogeological frameworks (Markovich et al., 2019; Wilson & Guan, 2004). Worse, mountain hydrogeological systems remain mainly uncharacterized as their steep topographic gradients and remoteness strongly limit access and site instrumentation. The scientific bottleneck regarding the understanding of the hydrogeological functioning of mountain groundwater systems is therefore above all a methodological gap, the filling of which requires the improved characterization of their subsurface geologic framework (Bense et al., 2013; Markovich et al., 2019).

Groundwater flow paths and origins in mountain catchments have traditionally been inferred using hydrogeochemistry, water stable isotopes, and environmental tracers such as noble gases and anthropogenic tracers (Alvarez-Campos et al., 2022; Baraer et al., 2015; Hilberg, 2016; Jung et al., 2021; Ma et al., 2018; Manning & Solomon, 2005). As they directly derive from flow processes, these methods can theoretically compensate for the lack of direct observations of hydraulic conductivity and hydraulic gradients from standard hydraulic methods (boreholes, pumping tests) (Ginn et al., 2009). However, because of water mixing processes, they constitute integrative methods that remain poorly effective to differentiate between hydrogeological models at the local scale (Troldborg et al., 2007) and to identify hydrogeologically pertinent structures in complex systems (Leray et al., 2012). Hence, in the absence of end-member waters with significantly different chemical signatures, the deconvolution of tracers and hydrogeochemical data is extremely challenging.

Water balance analysis is a straightforward method that has been mainly used for the estimation of water balance components and for closing the water balance (Andermann et al., 2012; Cochand et al., 2019; Hood & Hayashi, 2015; McClymont et al., 2010). However, closing the water balance may be strongly impaired in small ungauged catchments where the large amount of data required is not satisfied as ground data are rarely available and remote sensing data are often too coarse (Acharya et al., 2021; Hobouchian et al., 2017; Longuevergne et al., 2010; Zambrano-Bigiarini et al., 2017). Besides, addressing the role of geological structures on groundwater flow and surface water-groundwater interaction implicitly requires the selection of characterization methods that are able to image geological discontinuities, that is, those with a relatively fine resolution (tens of meters). In this context, geophysics has emerged as a non-destructive method to survey the subsurface at various scales and depths and in some occasions hydrogeological processes (Binley et al., 2015; Robinson et al., 2008). Electrical Resistivity Tomography (ERT) has been widely used (Samouelian et al., 2005) for soil moisture studies (Araya Vargas et al., 2021), the identification of groundwater aquifer geometry, and the study of geological structures (Ball et al., 2010; Martos-Rosillo et al., 2019; Robert et al., 2011). ERT cross-sections can be aligned to reveal resistivity contrasts resulting from geological structures and to construct a 3D representation based on previous geological knowledge (Figueroa et al., 2021). Gravity surveys can be performed at different spatial scales, from local to regional, and can identify tiny changes in gravity to obtain structural information (Telford et al., 1990). Gravity surveys are generally used to delineate the basement depth of sedimentary basins (Abbott & Louie, 2000; Figueroa et al., 2021; Murty & Raghavan, 2002; Yáñez et al., 2015); however, they can also be used to identify geological contacts and discontinuities that do not outcrop (Ruelleu et al., 2010). While they can be used to image geological structures, the abovementioned methods and many more geophysical methods are unable to image hydrogeological features without an additional hydraulic-based constraint such as groundwater level, water resurgences, etc. Besides, ground geophysical surveys of mountain catchments are limited by their remoteness, which has raised interest in the use of aerial surveys. So far, aerial geophysical surveys have been conducted by helicopter or airplane for large-scale studies (>1,000 km^2) focusing on major regional geological structures (Dumont et al., 2021; Hussien et al., 2017; Lopez Loera et al., 2015; Reeves,

2005; Vittecoq et al., 2019). Yet, the recent emergence of drones (UAV) has offered a potential means to explore the subsurface framework at much smaller scales and more systematically, thanks to their smaller clearance distances (less than 50 m) and closer profiles.

Hydrogeology is fundamentally at the cross-roads of various disciplines and multidisciplinary approaches have naturally shown their value for characterizing, understanding and managing groundwater as the joint use of various methods makes it possible to more widely cover the parameters space (Kreamer et al., 2021). Regarding mountain catchments, studies based on various methods became essential to develop a more in-depth knowledge of hydrogeological systems and to propose new conceptual models of their hydrogeological functioning (Christensen et al., 2020; Manning et al., 2021; Markovich et al., 2021; Ruiz Pereira et al., 2023; Somers et al., 2016). However, the choice of data that are informative and complementary enough and the interaction between disciplines that may not share the same approaches and perceptions are in itself challenging. The main objective of this study is to develop a novel multi-disciplinary approach to assess the hydrogeological role of geological features at the catchment scale in ungauged mountain catchments. To do so, we perform a thorough geological characterization through a multiscale geological mapping and ground and aerial geophysical instrumentation to accurately outline both the surface and the subsurface geological framework. To clearly establish the impact of geological features and heterogeneity on hydrogeological structures, hydrogeological information is retrieved from various sources and various data types, including spatially-distributed baseflow measurements, the Normalized Difference Vegetation Index (NDVI), and a thermal spring location and temperature. The multidisciplinary methodology is designed to get a comprehensive understanding of the system and establish a causal link between geological and hydrogeological features which cannot be achieved by each of the methods separately. The scope of this study is functional and pragmatical aiming to identify the key geological structures for groundwater flow but not the entire geological framework and focusing on a key hydrological variable which is the streamflow.

In the following section, we present the application of the methodology to the Parque Nacional del Río Clarillo, an ungauged mountain catchment in Chile whose large

geological heterogeneity is illustrative of both the scientific and methodological challenges to the analysis of mountain groundwater systems. After presenting the results in section 4.2, we discuss the capacity of various hydrogeological conceptual models to explain the observed streamflow variations and hydric singularities as well as the differentiating aspects and novelty of the proposed approach.

4.1.Study site and methodology

4.1.1. Study site

4.1.1.1. Climatic context

The Parque Nacional del Río Clarillo is an ungauged catchment with an area of 130 km² located 35 km southeast of Santiago (-33.72°, -70.49°, Figure 4-1 a and b). Situated in a semi-arid climate, the park is suffering from the uninterrupted drought that has been affecting Central Chile since 2010 and had led to a decrease in precipitation of about 30% in this region (R. Garreaud et al., 2020). Though presenting significant interannual variability, the average annual precipitation downstream of the park historically amounted to approximately 700 mm during the period 1990-2010 (DMC, 2023). However, since the beginning of the drought, it very often does not exceed 300 mm and reached 400 mm on very few occasions (DMC, 2023). Accordingly, observations by park rangers and technical studies (Niemeyer, 2002) point at a severe reduction of the Río Clarillo baseflow of close to 75%. Still, these observations should be interpreted with caution as they remain very sparse. The Río Clarillo regime is pluvionival with streamflow maintained by snowmelt in the upper part of the catchment. While snowmelt historically lasted up to the end of March, the past few years have shown an earlier melting, which rarely persists after January according to observations by park ranger.

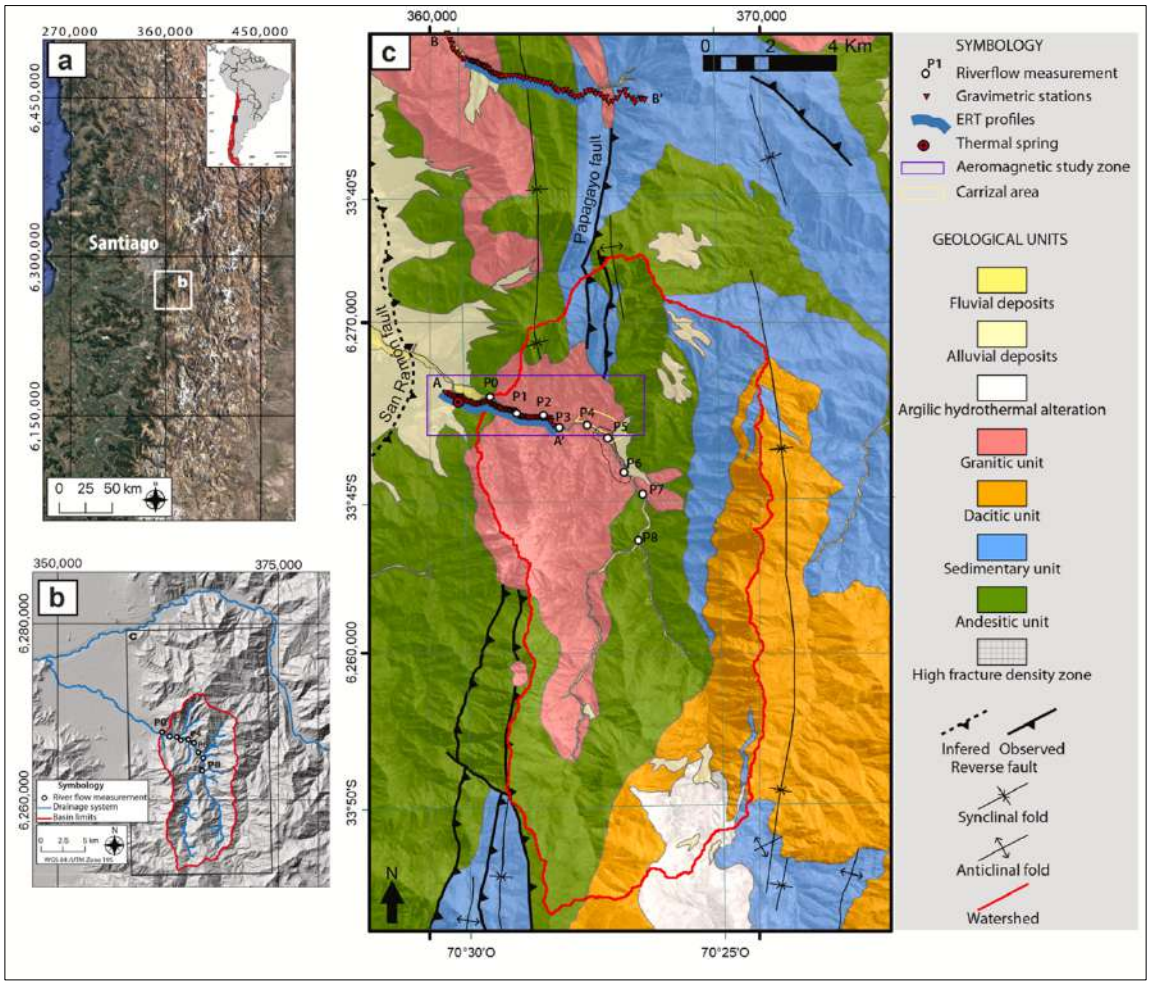

Figure 4-1 a) Satellite view of the Santiago area, the white rectangle outlines the study area. b) Topographic map overlaid with the Parque Nacional del Río Clarillo catchment limits, the drainage system and the streamflow measurement points (numbered in increasing order from P0 to P8 going upstream) c) geological map of the study area overlaid with the ERT profile (blue lines), the gravimetric profile (red triangles), the area covered by the aeromagnetic flights (areas delimited by purple line) and the river flow measurements (white dots surrounded by black). A 23°C perennial thermal spring located at the exit of the Parque Nacional del Río Clarillo is indicated with a red dot.

4.1.1.2. Geological context

The present-day configuration of the Andes of Central Chile is marked by the development of two margin-parallel ranges, the Coastal Cordillera to the west and the Principal Cordillera to the east, separated by the Central Depression alluvial plain. The study area is located on the western margin of the Principal Cordillera (Figure 4-1a), and

is uplifted by more than 2,000 m over the Central Depression by the cumulative displacement of the west-vergent San Ramón-Pocuro Fault System (SRPFS)(Armijo et al., 2010; Rauld, 2002).

The geology of the Río Clarillo catchment records the evolution of the western margin of the Eocene-Miocene Abanico Basin (Figure 4-1c). This includes the volcanic and sedimentary rocks of the extensional phase of the Abanico Basin, the Abanico Formation (Oligocene-Miocene), and the volcanic rocks that represent the tectonic inversion of the basin, that is, the Miocene Farellones Formation (Charrier et al., 2002). These stratified units are intruded by granitic rocks of the La Obra pluton (c.a. 21 Ma), (Figure 4-1c). However, at the scale of this work, there is no consensus on whether the rock bodies outcropping in the Río Clarillo catchment should be assigned to these formal units (Fock, 2005; Piquer et al., 2017, 2021; Thiele, 1980).

At the regional scale, the Abanico Formation shows intense deformation of tight west-vergent folds in the westernmost outcrops that gradually decreases towards the east to wide and open folds. The Farellones Formation lies unconformably over the tight folds affecting the Abanico Formation in the westernmost outcrops, showing less intense folding, and becomes gradually parallel to the underlying Abanico formation towards the east (Charrier et al., 2002; Fock, 2005).

Scarce Pliocene to Holocene alluvial and fluvial deposits are preserved in the main fluvial valley and in tributary ravines. From the mouth of the Río Clarillo valley, alluvial deposits show a strong increase in thickness towards the Central Depression, reaching a thickness of up to 500 m (González et al., 2018; Yáñez et al., 2015).

4.1.2. Geological methodology

The geological survey consisted of a regional geological mapping (1:100,000 scale) of the whole Río Clarillo catchment (Figure 4-1c), refining the previous geological maps in the area. To assess controls on primary permeability, since there is no consensus on the assignment of these rock units to the formal lithostratigraphic units in the area (Fock, 2005; Piquer et al., 2021; Thiele, 1980), strictly lithological units were defined and mapped. As for the controls on structural features on secondary permeability, faults, folds, and fracture zones were surveyed at a finer scale, focusing on fracture systems along the riverbed and on hilltops where rock outcrops are observed.

4.1.3. Geophysical methods

The geophysical study involves the joint use of a UAV-based aeromagnetic system (with only limited previous applications in the Andes (Sanhueza et al., 2022; Yáñez et al., 2020)) and on-ground transect data obtained from ERT and gravimetry. As shown in Figure 4-1c, transect (A-A') and the drone coverage are oriented east-west to perpendicularly intersect the main structures present in the study site as the SRFPS is N-S oriented (see section 4.1.1.2 for a description of the geological context). As shown in Figure 4-1c, a second roughly E-W transect (B-B') is also performed. This transect is located 10 km northeast of the Río Clarillo catchment, in the Río Coipo valley, and was performed to gain insights on the geological structures on the eastern flank of the La Obra pluton, where the rough topography prevents the use of ground-based geophysical methods along the primary transect A-A'. Furthermore, having two parallel profiles allows a 3D view of the geology to be obtained (N-S along strike variations). We use the same methodological approach in both transects. The results of this second transect are presented in the supplementary material; nevertheless, their contribution to our geological interpretation of the study area is included in the discussion.

4.1.3.1. Electrical Resistivity

Electrical Resistivity Tomography is an exploration method that measures the subsurface distribution of electrical resistivity with high resolution (Dahlin, 2001). It can be used to detect water-saturated areas and the depth of the contact between the sediment surface layer and the basement unit, as well as to identify fracture and fault zones in the basement

unit, which show lower resistivity compared to the surrounding unfractured rock. As the ERT method has optimal definition in the shallow subsurface, it is limited to depths of around 250-300 m, depending on the dipole separation.

Data were acquired using an ABEM Terrameter LS2 (Guideline Geo, Stockholm, Sweden). The measurement protocol involved a Dipole-Dipole array with 48 electrodes and a 20 m inter-electrode spacing. Each profile was 1 km long with an investigation depth of about 250-350 m. The Dipole-Dipole array was chosen for its particularly good definition of the vertical structures typically present in faults and geological layers (Loke, 2004; Samouelian et al., 2005).

The Río Clarillo and Río Coipo transects are respectively composed of six and seven profiles (the former having fewer profiles due to field conditions). Both profiles present a 500 m overlap between each profile to obtain a better characterization of the structures. The apparent resistivity datasets obtained in the field for each profile were inverted separately to obtain 2D resistivity cross-sections. The data were inverted using the ZonRes2D software (Kaminsky, 2010). Each profile was then "stitched" to the adjacent one to obtain the full transect using the stitching tool in the Oasis Montaj software (Seequent, Christchurch, New Zealand). This stitching method is necessary to obtain the full-length transect without noticeable edge effects at the extremes of the profiles.

4.1.3.2. Gravimetry

Gravimetry measures the gravity field caused by differences in mass distribution below the surface. Variations in the residual gravity anomaly i.e. the difference between properly corrected gravity observations and the regional field (see a description of this process later in this section) can be indirectly associated with the subsurface density distribution, which can in turn be used to infer geological information along the measured profile. We used a CG-5 Autograv relative gravimeter (Scintrex, Concord, ON, Canada) with a resolution of 5 μGal and a Trimble R4 GNSS (Trimble, Westminster, CO, USA) receiver that gives the position and altitude with a precision of less than 30 cm. The Río Clarillo transect (A-A') has 56 gravimetric stations spaced ≈50 m apart along a 2.5 km long profile (Figure 4-1c). The Río Coipo transect (B-B') presents 72 gravimetric stations spaced ≈100 m apart along a 7 km long profile (Figure 4-1c).

Gravity data were corrected using standard procedures (Telford et al., 1990): (1) The tidal correction is computed by the instrument during all the measurements and the drift correction is estimated as a linear function during the day with measurements at the base station at the beginning and end of the day; (2) The latitude correction was computed using the WGS84 reference ellipsoid; (3) The absolute gravity value was obtained using the base station at the Department of Geophysics of the University of Chile (Universidad de Chile) (Gravity DGF: 979,416.07 [mGal]); (4) The Free-air and Bouguer corrections were computed using the altitude obtained from the differential GNSS and assuming a mean subsurface density of 2.67 g/cm^3; and (5) The Terrain correction was calculated with a high-resolution digital terrain model with a 5 m resolution (AW3D Standard product, acquired from NTT DATA Corporation). Finally, the regional effect was removed to obtain the residual anomaly along the profile due to the effect of the low-density bodies under the Principal Cordillera at deeper crustal levels: for this purpose, the Bouguer anomaly of Santiago obtained by Yáñez et al. (2015) was removed from our data. Then, the result was processed using the rock measurement performed at a point of zero-anomaly as a constraint. After correcting the gravity observations, we obtained a residual gravity anomaly suitable for geologically constrained gravity modelling. The modelling process consisted of a forward modelling using the ModelVision software (Encom), with the model output being compared to the residual gravity anomaly.

4.1.3.3. UAV-based magnetic survey

In the magnetic method, the magnetic properties of rocks are measured using a magnetometer. It provides a valuable tool to map geology and structural networks if they involve magnetic contrasts. The operational simplicity of total field magnetometers, in which the magnetic field is recorded almost instantaneously regardless of the sensor or platform orientation, make them very suitable for use in mobile platforms, such as airplanes, ships, or UAVs. We used a Bartington MAG03 fluxgate magnetometer (Bartington Instruments, Oxon, United Kingdom) with three orthogonal components mounted on a UAV system. We surveyed one block (see spatial distribution in Figure 4-1c, purple polygon). The polygon is 6,600 m long and 1,800 m wide, covering large parts of the reserve and both side contacts of the intrusive unit. Lines were flown in the

N-S direction with a line separation of 200 m and a flight altitude of 50-80 m above terrain level. The location was recorded with a standard GPS with an accuracy of 5m.

The following corrections were applied to the raw magnetic field observations: (1) removal of diurnal variations; (2) removal of the Earth's magnetic field (IGRF, International Geomagnetic Reference Field); and (3) recovery of the total magnetic field from the three-component fluxgate magnetometer (for details see Sanhueza et al., (2022)). After data correction, we obtained a residual magnetic field dominated by magnetic sources in the shallow crust. The data were then reduced to the magnetic pole (RTP), an approach which aims to centre anomalies over their source (Blakely, 1995). The magnetic data were then interpreted qualitatively by comparing the RTP map with geological, hydraulic, and additional geophysical information.

4.1.4. Streamflow measurements, remote sensing data, and hydric markers

The streamflow rate was measured from the outlet of the national park up to the confluence of the two main tributaries of the Río Clarillo, 9 km further upstream (Figure 4-1b). The measurements were carried out at least every kilometre and when possible at smaller intervals in the sectors of interest, that is, where the flow exhibited significant variation. Data were acquired with an Acoustic Doppler Velocimeter (FlowTracker, SonTek). Three campaigns were completed during the 2019 recession period (austral autumn) to better evidence the contribution of groundwater to the baseflow. The first and third campaigns are complete campaign from the outlet P0 to the confluence P8 while the second campaign is simply a small-scale campaign between points P4 and P5. If the streamflow measurements can be quantitatively compared between each campaign, the three campaigns exhibit similar trends and features and can serve as cross-validation. Some data points are missing due to technical, logistical or staff complications on site (e.g., point P5 during the third campaign). We also considered different types of soft hydric data (i.e., qualitative data), which are essential in ungauged catchments (Seibert & McDonnell, 2015). The soft data were mainly obtained from the knowledge of the nearby community of Pirque, the testimony of park rangers, and the authors' observations during field campaigns.

To complement the streamflow analysis and to obtain a long-term assessment of the streamflow dynamics and the persistence of possible resurgence zones, we analysed NDVI time series. The NDVI measures the difference between infrared and red light to quantify vegetation presence and density using reflectance bands. It is the most common index used in remote sensing to understand drought processes (Gu et al., 2007, 2008), related plant water stress (Ballester et al., 2019; Katsoulas et al., 2016), and to evaluate groundwater fluctuation and vegetation cover (Pan et al., 2008; Seeyan et al., 2014). The NDVI was obtained from the MODIS/MCD43A4 product (Schaaf & Wang, 2015) through the Google Earth Engine (Gorelick et al., 2017) from 24 Feb 2000 to 31 Dec 2019, that is, covering the drought period and the previous decade.

4.1.5. Conceptual hydrogeological models

We develop various conceptual hydrogeological models and discuss hypotheses in relation to the streamflow evolution through the catchment. As argued later in section 4.2.4, the groundwater-surface water interaction is highly likely to be related to geological discontinuities. Geological controls on groundwater-surface water interaction are further reinforced by a parallel sensitivity study (not shown here) of baseflow evolution through the catchment to varying uniform recharge rates on homogeneous numerical models in which topography-driven groundwater flows do not reproduce the streamflow measurements carried out in our catchment. Therefore, the conceptual models differ mostly in terms of the drainage surfaces and geological structures involved in the groundwater-surface water interaction. The conceptual models are presented in detail in section 4.3.1 following the joint interpretation of data presented in section 4.2.4.

To offer a more quantitative point of view, the proposed conceptual models can be segregated by simple mass balance. Assuming steady-state conditions with no storage in the soil nor in the aquifer, a relatively low direct runoff coefficient considering the forest cover and relatively constant baseflow over the year, the effective precipitation in each catchment (defined as total rainfall minus actual evapotranspiration) can be directly compared to the baseflow per drainage area, *i.e.,* what goes in goes out. A mean yearly value for effective precipitation is estimated from ground-based meteorological data for the period 1985-2013, as acquired by the park administration in the vicinity of the

catchment outlet P0 (Figure 4-1). The estimated effective precipitation over the catchment in this period is close to 120 mm.

4.2. Results

We successively present the results of the geological mapping for hydrogeological considerations, the geophysical results, and the results related to streamflow measurements and remote sensing analysis.

4.2.1. Geology

Strictly based on lithological characteristics (Figure 4-1c), four rock units were defined and mapped in the studied area, some of which were recognized in more than one stratigraphic position. The first is an “Andesitic unit” composed mainly of andesitic lava flows and hypabysal porphyritic intrusives, with minor andesitic tuffs and sandstones. This unit was recognized west of the newly identified Papagayo fault presented in the next paragraph and at the base and in the middle of this fault hanging wall. The second is a “Sedimentary unit”, which is a sandstone-dominated unit that also includes conglomerate, lithic tuff, and andesite intercalations and crops out discreetly in the footwall of the Papagayo fault - extensively in the middle section of its hanging wall and as a small wedge within its upper section. The third is a stratified “Dacitic unit”, which is composed of brightly coloured dacitic lavas and tuffs recognized in the upper section of the Papagayo fault hanging wall. The fourth unit is a “Granitic unit” composed of monzogranites, syenogranites, and granodiorites, which outcrops in the western flank of the Principal Cordillera, intruding the stratified volcanic and sedimentary rocks.

The structural features of the study area allow the recognition of two distinct structural domains. The first is a western domain limited by the main trace of the west-vergent San Ramón fault and a newly identified N-S reverse fault, which here is called the Papagayo fault (Figure 4-1c). This domain shows tight short-wavelength (2-4 km) folds and minor inverse faults, generating highly dipping strata. The second domain is located to the east of the Papagayo fault and shows low dips on the flanks of long-wavelength (6-8 km) folds. However, 2 km east of the Papagayo fault, a west-vergent anticline is recognized in the hilltops affecting the andesitic and sedimentary units. Directly beneath the

anticline, faulting and fracturing is recognized affecting the granitic rocks outcropping along the riverbanks. A detailed structural survey in this area showed a zone with a high fracture density with vertical and closely spaced NS- and EW- striking sets and minor inclined NW- and NE-striking sets (criss-crossed zone in Figure 4-1c).

4.2.2. Geophysical study

Figure 4-2 presents the magnetic field reduced to the magnetic pole. The advantage of this representation is that it tends to show a direct correlation between the magnetic anomaly and the causative magnetic source (i.e., a positive correlation when the magnetic source is more magnetic than the surroundings, and a negative correlation for the opposite case).

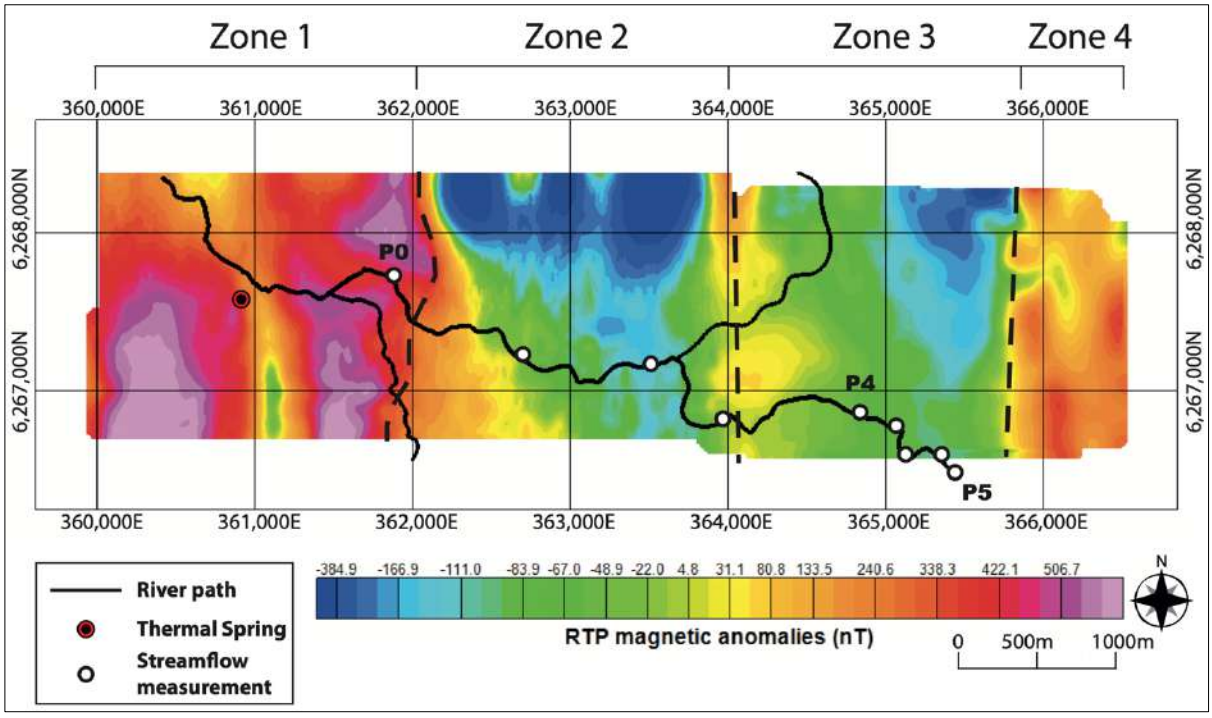

Figure 4-2 Aeromagnetic anomaly map (reduced to the pole) for the Río Clarillo area (Figure 4-1, purple rectangle). Dashed lines represent the limit between magnetic zones.

On this map, we identify four zones, mainly oriented north-south. Going from west to east, the first 2,000 m of the profile (zone 1) presents a strong positive magnetic anomaly that is relatively homogenous in the NS direction. Inside this zone, a short-wavelength (less than 200 m) but persistent negative anomaly is observed at longitude 361,000E. Secondly, in zone 2, between 362,000E and 364,000E, we observe a negative anomaly

with its larger amplitude in the northern half, and tapering off southward. This broad negative domain is followed to the east by another negative domain (zone 3) of the same length and signal amplitude (-60 to -80 nT) but decreasing southward and westward. The limit between zone 2 and zone 3 is a fairly linear positive NS anomaly around 364,000E. Finally, zone 4 extends east of 366,000E, and is characterized by a broad positive anomaly that seems to extend beyond the study area.

In agreement with the geological map, the mineralogical composition of geological units and susceptibility samples taken from outcrops (Table 4-1), the magnetic sources associated with zones 1 and 4 represent volcano-sedimentary units, with mid-to-high contents of ferromagnetic minerals. In contrast, the negative magnetic anomaly of zones 2 and 3 can be associated with the intrusive body mapped in the geology. This intrusive has a consistently more felsic mineralogy and low magnetic susceptibility with a clear negative contrast compared with the volcanic units in the flanking domains (Table 4-1).

	Measured density (g/cc)	Measured magnetic susceptibility (SI)
Intrusive rocks	2.64 +- 0.03	0.04 +- 0.01
Volcanic rocks	2.73 +- 0.09	0.27 +- 0.18

Table 4-1 Mean measured density (g/cc) and mean magnetic susceptibility (SI) for rock samples collected on the field (20 samples)

The sharp transition between magnetic zones 3 and 4 can be associated with the mapped contact between the intrusive unit and the volcanic unit at the eastern border of the intrusion. Meanwhile, at the western limit of the study area, we can identify a similarly sharp transition between zones 1 and 2, in good agreement with the contact between the intrusive and volcanic rocks. We postulate that the positive anomaly at 364,000 E (which separates zones 2 and 3) represents a fault that provided room for the emplacement of more mafic magmatism (the andesites of the flanking zones 1 and 4) and/or a path for hydrothermal circulation and secondary magnetic enhancement due to contact

metamorphism. This anomaly is hence associated to the newly identified Papagayo fault which appears to be a large-scale regional fault according to the gravimetric survey carried out in the Río Coipo catchment. Looking at the path of the river entering zone 2 going west, we see a change in direction from E-W to S-N, which may be another sign of the influence of this fault on the river network. Finally, in zone 1, the relative negative anomaly at 361,000E may be related to a demagnetization of the volcanic rocks caused by the hydrothermal fluid circulation at the piedmont fault zone.

The Río Clarillo ERT profile (Figure 4-3) can be separated into two well-defined zones, identified as zones 1 and 2 on the aeromagnetic map. Zone 1 is defined at distances of between 0-1,300 m along the profile, where the environment is much more conductive than the other part of the profile (100-500 ohm.m versus more than 1,000 ohm.m eastward). In this zone there are some small-wavelength heterogeneities (100-200 m) that are relatively positive and tabular (along-profile distances of 200-400 m and 800-1,000 m) and a shallow sub-horizontal negative anomaly (along-profile distance of 100-500 m). Magnetic zone 2 is partially represented between 1,300 – 3,600 m on the ERT profile. It contains a shallow (~ 50 m depth), almost continuous and relatively conductive layer (<300 ohm-m) above a resistant body (> 1,000 ohm-m).

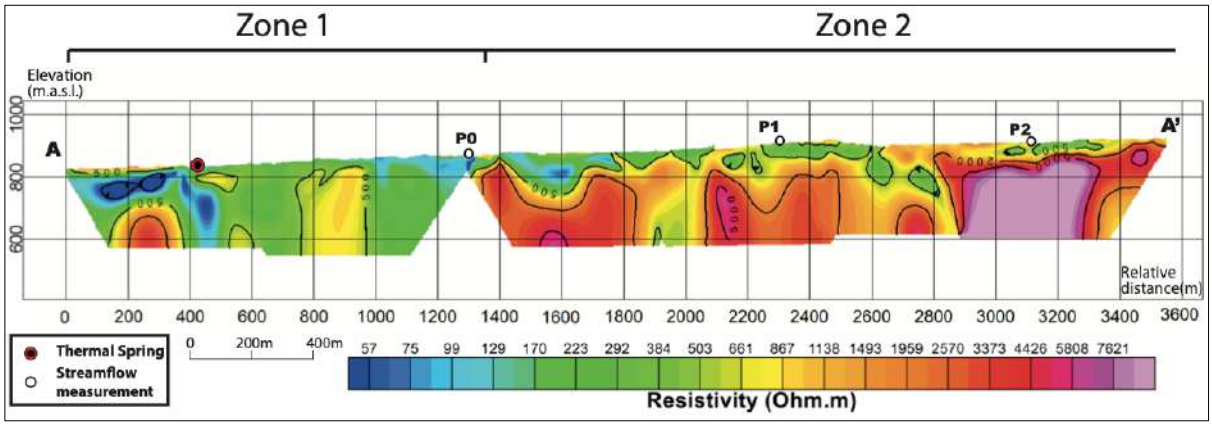

Figure 4-3 Electrical resistivity model for the Río Clarillo transect (A-A', Figure 4-1). Projections of the hydraulic markers on the profile (red dot for the thermal spring and white dots for the river flow measurements) as well as the magnetic zones limits (Figure 4-2) presented over the transect.

The geological interpretation is based on the locations of the two aeromagnetic zones. The higher resolution of the ERT profile compared to the magnetic data suggest the presence of a shallow layer of sediments overlying the volcanic and intrusive units.

Zone 1 evidences a more conductive layer which likely represents the alluvions that cover the volcanoclastic rocks of the western flank of the study area. The magnetic signal in this zone cannot be used to discriminate this sedimentary unit, probably due to its low magnetic content. The vertical conductive structure between 400-500 m and the horizontal thin layer between 0-400 m are likely to be associated with the location of the thermal spring, as this really low resistivity can be associated with saturated sediments. Zone 2, between distances of 1,300 and 3,600 m the eastern portion of the ERT profile, occurs within the granitic intrusion and is covered by a thin layer of alluvial material. The high and rather homogeneous resistivity underneath the thin conductive cover suggests that this intrusive is a relatively homogeneous unit that is probably cut by structures at distances of 2,000 m and 2,800 m along the ERT profile. Even though no regional large-scale structures are defined in this area, Piquer et al. (2021) observed and mapped secondary structures inside the granitic intrusion at similar locations, which supports our working hypothesis on the discontinuity of the granitic body. These results indicate that these heterogeneities represent faults or fold axes in the geology associated with the domain of high electrical resistivity.

The gravity anomaly along the Río Clarillo valley transect (Figure 4-4 upper panel) shows two distinctive sectors, a western sector characterized by a relative negative anomaly (-5 mGal) between distances of 0-500 m along the profile. To the east is a wide zone with a relatively steep gradient (2 mGal/km) between distances of 500-1,500 m along the profile. The remainder of the profile, between distances of 1,500-3,500 m, shows a relatively flat gravimetric response at -2.5 mGal. The proposed density model considers a background density of 2.67 gr/cc, as well as the structures and layers defined at the subsurface by ERT and magnetic interpretations. Densities for intrusive and volcanic rocks are based on in-situ rock sample measurements (Table 4-1), while sediment density is obtained from Yáñez et al. (2015).

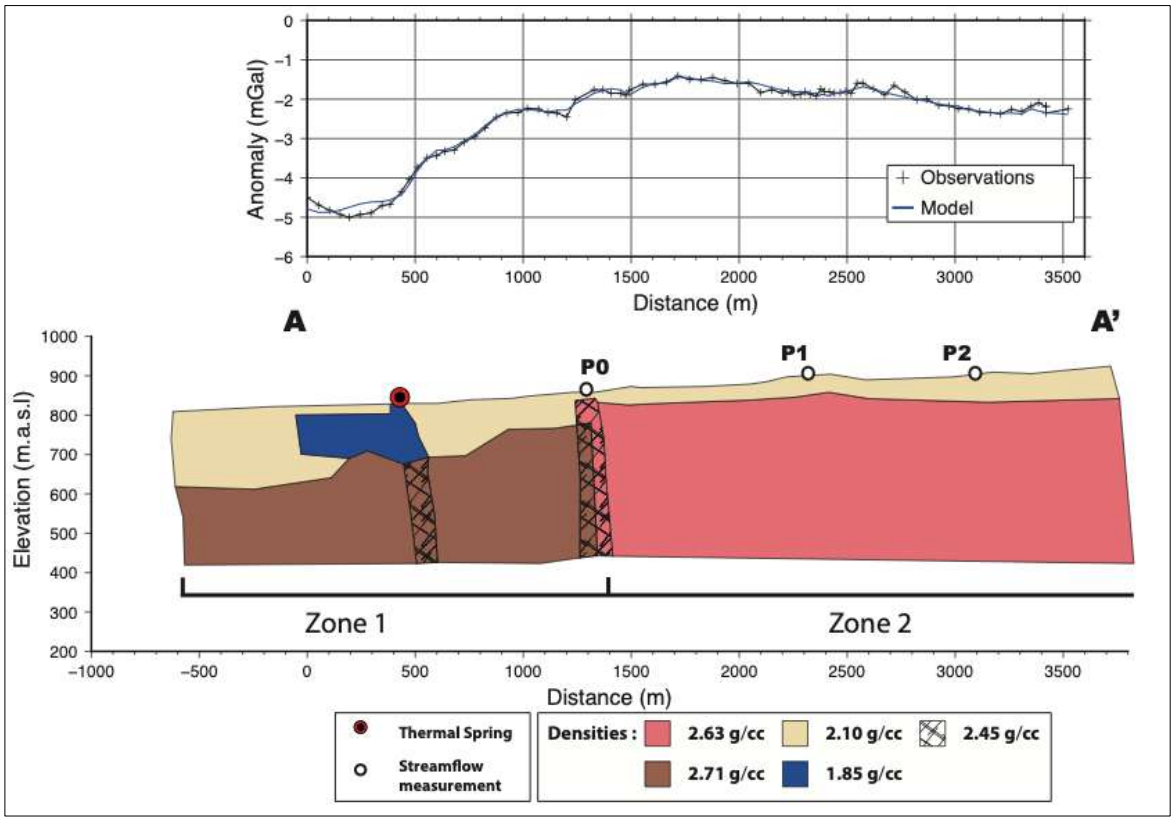

Figure 4-4 Representation of the gravity study for the Río Clarillo transect (A-A', Figure 4-1) and the associated interpretation derived from geophysical and geological constraints. Top: The black line with crosses represents the data (each cross is one data point), the blue line represents the fit of the model described above. Bottom: Model representing the gravity data based on density variations. For a better understanding, it includes projections of the hydraulic markers on the profile (red dot for the thermal spring and white dots for the river flow measurements) as well as the magnetic zones limits (Figure 4-2) presented above the transect.

As shown in Figure 4-4 upper panel, the model response is in good agreement with observations, and is thus a plausible solution that is consistent with geological observations. Low density and thick sedimentary cover above the volcanic basement explain the lower gravity of the western side. The thickness of the sedimentary unit decreases eastward in line with the decrease of the amplitude in the negative gravity signal. This sedimentary body represents the alluvial fan at the piedmont. Considering the interpretation of the ERT profile, the low-resistivity zone at a distance of around 500 m is here represented as a fractured area in the volcanic unit and a low-density area in the sediment layer (1.85 gr/cc). As seen on the ERT profile as a low-resistivity zone

(below 50 ohm.m), this low-density zone extends between distances of 0 and 400 m, in the sediment layer, and probably represents a clay-dominated body associated with the thermal spring zone recognized in the area. Towards the east (zone 2), an almost flat signal is modelled as the gravimetric response of the more felsic intrusive body (2.63 gr/cc) covered by a relatively thin layer of sediments. In this zone, the sediment cover is approximately 50 m, which agrees well with the ERT transect, which shows a covering of intermediate-resistivity material of a similar thickness. At the contact between the two zones, at a distance of around 1,300 m, there is a small decrease in the gravity anomaly. This negative anomaly is associated with a low-density fractured zone. This contact zone is associated with the fractures induced by the intrusive emplacement. The fracture zone identified at a distance of 500 m could favour groundwater exfiltration, creating a preferential upwelling flow, according to the location of the thermal spring over this fault. The proximity of the two fracture zones (which are located at along-profile distances of 500 m and 1,300 m) and their similar vertical structure indicate that a joint fault system may be connected at depth and act as listric faults.

4.2.3. Streamflow measurements and remote sensing analysis

Streamflow measurements acquired during the 2019 recession are displayed with regards to drainage (or upslope) area (Figure 4-5).

A few interesting features are observed. First, we observe a significant increase of the streamflow at point P1 (grey triangles in Figure 4-5). However, this increase is not systematically observed within the same recession period (orange squares in Figure 4-5). Second, and most notably, it exhibits a significant increase of approximately 50% within a 1km distance (between P5 and P4-P3). We interpret this variation as groundwater exfiltration as there is no significant increase of the drainage area and there is no affluent observed in the area or a superficial supply of any type (snowmelt, water bodies). Groundwater exfiltration has been observed in the Carrizal area (Figure 4-1c) by park rangers, who have noted that “water is usually seen disappearing in the river” while they are going back up the Río Clarillo which is consistent with the lower streamflow rate from P4 to P5. Additionally, some hydric features are observed downstream of point P5,

such as a permanent puddle about 50 m uphill and a curtain of dripping water on the east at the riverbank.

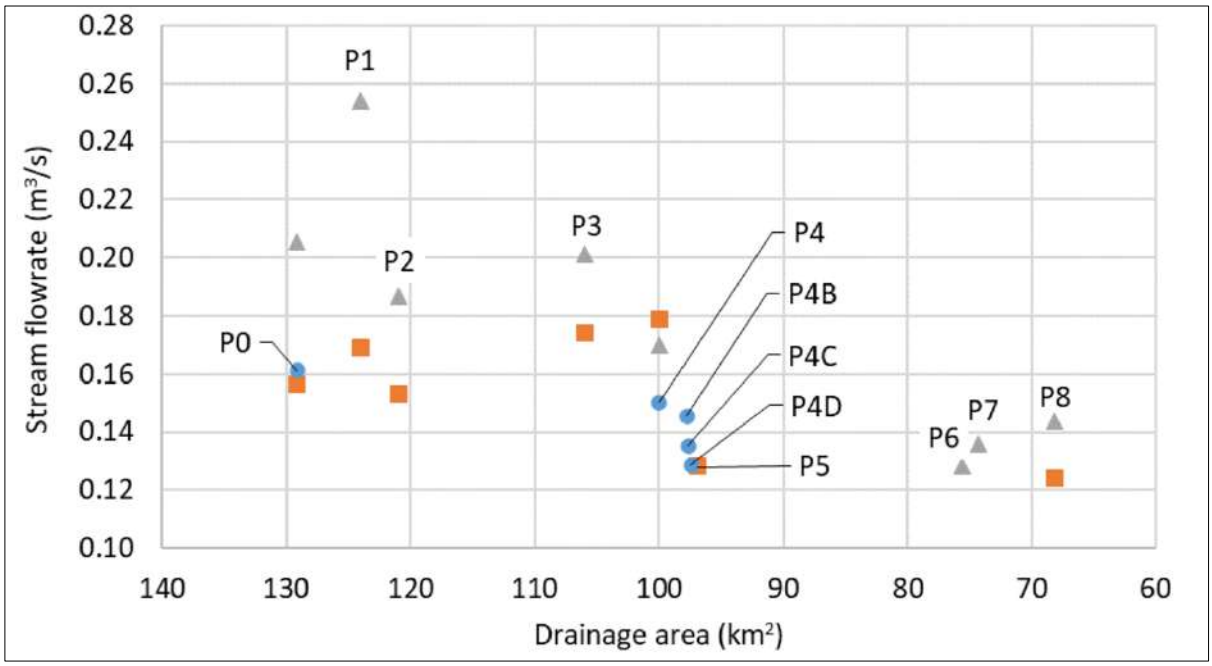

Figure 4-5 Streamflow rate during the 2019 recession period (austral autumn) as a function of drainage area. P0 point corresponds to the outlet of the Parque Nacional del Río Clarillo catchment (i.e., downstream at the Andes piedmont) while P8 corresponds to the confluence of the two main affluents, approximately 9 km upstream. Orange square corresponds to March 2019 campaign, blue circle corresponds to April 2019 resampling campaign and grey triangle corresponds to the June 2019 campaign.

The persistency of the groundwater exfiltration is confirmed by the difference in NDVI between the Carrizal area and the entire national park. The Carrizal area is displayed here as a strip 1,000 m in length and 500 m in width along the east side of the river where geological and hydric features have been observed. Over the period 2000-2019, the mean NDVI in the Carrizal area was 0.57, while it was 0.36 in the entire national park. The difference in NDVI between the Carrizal area and the entire national park is almost systematically positive (Figure 4-6), indicating that the Carrizal area has denser vegetation due to a higher water availability. In conclusion, both qualitative observations and quantitative data indicate that the groundwater exfiltration between P5 and P4 has persisted for at least the last two decades.

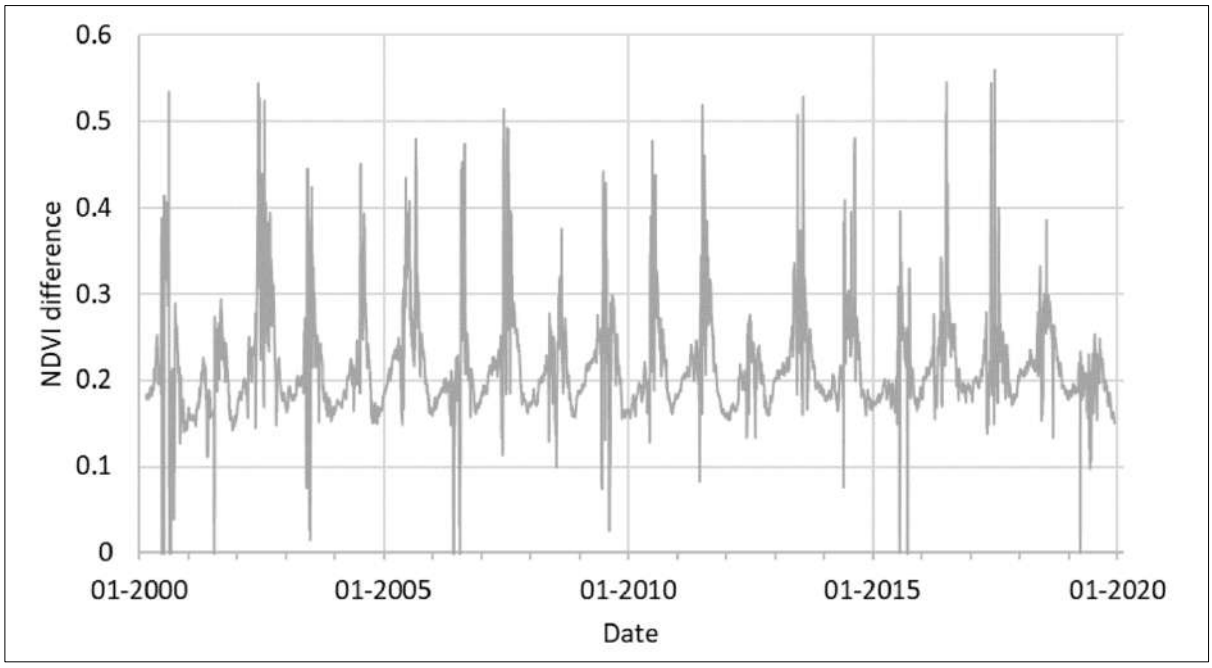

Figure 4-6 Difference between the mean NDVI of the Carrizal area and the mean NDVI of the entire National Park for the period 2000-2019, included.

4.2.4. Joint interpretation of geophysical and geological results and hydraulic markers

The interpretation of the magnetic map allows us to describe four north-south zones. The ERT and the gravity transects overlap zones 1 and 2 and indicate a similar spatial extent of these zones, which reinforces our results and interpretations. Moreover, the thermal spring is identified using each of the geophysical methods, indicating a relationship between this feature and the presence of a fault inside the volcanic unit. The temperature of the thermal spring is about 23°C. As the geothermal gradient is about 3°C/100 m in this region (Muñoz & Hamza, 1993; Valdenegro et al., 2019), it is possible to approximate at first order that this thermal source is fed along a 300 m deep structure at least, which is supported by the ERT interpretation and the gravity modelling. Both methods indicate that the thermal spring is likely associated to upwelling flow along a fault or fractures zone as seen on other locations along the Andes in Central Chile (Figueroa et al., 2021). Our second hydraulic indicator is the increase of baseflow that was measured between points 5 and 4. This area was only monitored with a UAV-based magnetic study. The contact between the volcanic unit at the eastern end of the reserve

and the intrusive unit might be of significance for the increase of the river baseflow. Nevertheless, the location of the increase in the river flow is not exactly located over the contact defined on the aeromagnetic map (Figure 4-2). According to the geological map, the resurgence area close to the contact, presents a pattern of local east-west fractures (criss-crossed zone in Figure 4-1c). As seen at the western edge of the contact between the intrusive unit and the volcanic unit (Figure 4-4), a highly damaged zone engenders the structural control of water flows.

4.3. Discussion

Based on the various observations described in the previous section, we first discuss the capacity of various conceptual hydrogeological models to explain the observed streamflow variations and hydric singularities. We then discuss the differentiating aspects and novelty of the proposed multi-disciplinary approach for characterizing groundwater flow patterns in mountain catchments and for identifying structural controls on groundwater flow patterns and surface water–groundwater interaction.

4.3.1. Conceptual hydrogeological models

We propose three different conceptual models based on the observed geological features. First, groundwater exfiltration between P5 and P4-P3 could simply originate from the local drainage of lateral hillslopes in the Carrizal area, which are partly composed of alluvial deposits (Model 1 of Table 4-2, Figure 4-7).

However, the Carrizal area offers a very small drainage area (3 km^2 from P4 to P5 and 9 km^2 from P3 to P5), which we argue is likely insufficient to explain the full extent of the resurgence. Second, as the exfiltration occurs in the vicinity of the contact between the intrusive and volcanic units, it could be related to a reduction of the groundwater seepage area, that is, a reduction of the active depth of the system due to a much less permeable underlying unit outcropping (Model 2 of Table 4-2, Figure 4-7), consistent with the results from section 4.2.2. In that case, the drainage area could be the entire catchment area upstream of point P5, which is close to 100 km^2.

Model	Main process	Surface drained (km^2)	Main geological structures involved
1	Local drainage from lateral hillslope	3-9	Alluvial deposits
2	Upstream groundwater exfiltration deriving from groundwater seepage area reduction	97	Pluton-volcanic rocks contact
3	Water export from Los Bueyes catchment	12	Papagayo N-S regional fault, including secondary E-W local fault system

Table 4-2 Summary of possible conceptual models associated with their main process and the geological structure involved. Contribution surface values corresponds to Figure 4-7 area.

Finally, as shown on the geological map (Figure 4-1c) and described in section 4.2.1, the Carrizal area shows a large number of heterogeneities inside the intrusive unit. It is described as highly fractured in relation to a local E-W steeply dipping fault zone (criss-crossed zone in Figure 4-1c) and close to the N-S major Papagayo fault This local fault zone and the associated water resurgence may be a local effect of the E-W faults and the fracture network in this area with no influence of regional structures. Still, it is likely that the principal N-S structure is directly related to these E-W faults forming a fault network with secondary structures perpendicular to the major one. Supporting evidence for this last model is provided by the very low streamflow from the nearest downstream tributary, Los Bueyes (green catchment in Figure 4-7), with no significant streamflow increase measured at P2. The catchment contributing to this tributary is directly stroke by the N-S fault identified by both the geological mapping and UAV-based magnetic results. This N-S structure likely exports groundwater of the contributing subcatchment to the identified resurgence area (Model 3 of Table 4-2, Figure 4-7).

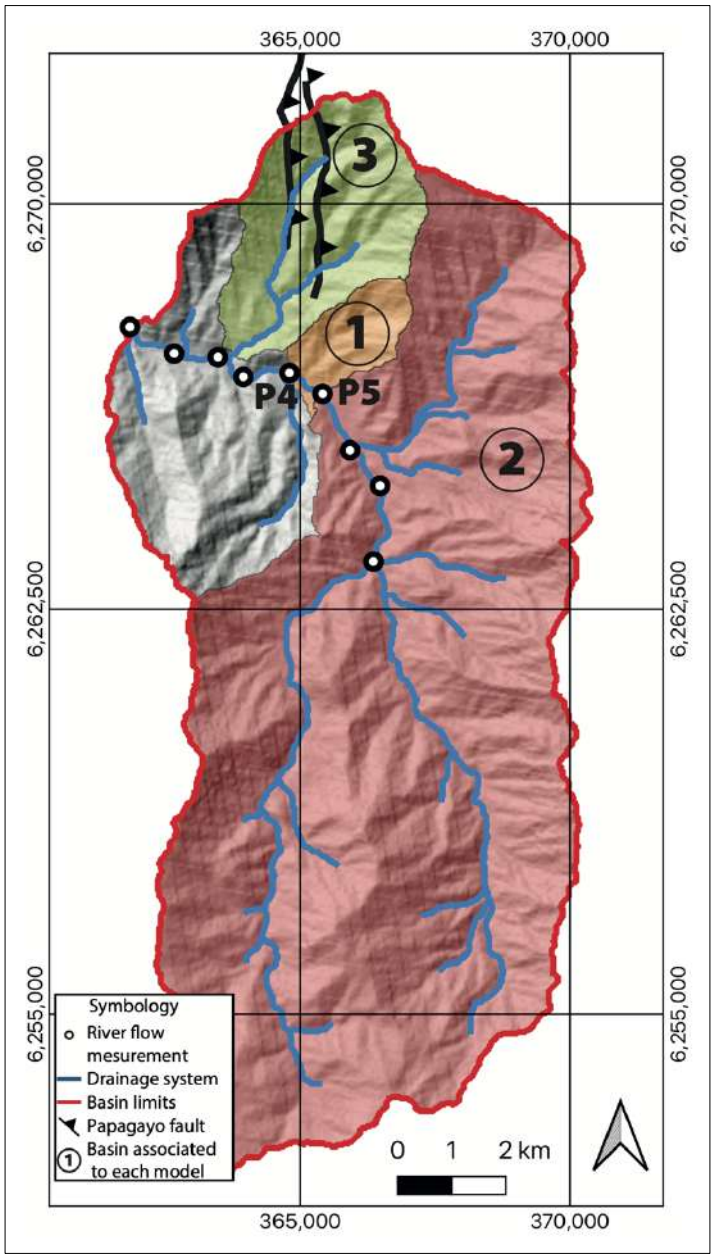

Figure 4-7 Representation of the Parque Nacional Río Clarillo catchment with river network (blue lines) and river flow measurements (black-circled white dots). Numbers 1 to 3 correspond to the possible drainage areas contributing to the resurgence between points P4 and P5, based on the three models mentioned in sections 4.1.5 and 4.3.1. Grey area within the catchment is not part of any of the proposed models.

As presented in Table 4-2 and above, each conceptual model corresponds to significantly different drainage areas. Model 2 can be discarded as the estimated flow from simple mass balance (as presented in section 4.1.5) is seven times larger than the resurgence

flow. In model 1 and model 3, the estimated flow is 0.22 and 0.90 times the resurgence flow, respectively. Thus, model 3 is the most likely scenario considering the drainage area of each sub catchment. Hypothetically, a combination of models 1 and 3 might as well explain the resurgence processes considering the uncertainty in the simple hydrological balance presented in section 4.1.5.

4.3.2. Differentiating aspects and novelty of the approach

This work presents a methodology to identify structural controls on groundwater flow patterns and surface water–groundwater interaction. The scope of the methodology is above all functional in the sense that it aims to identify the key geological structures for groundwater flow but in no way to characterize the entire geological framework. This functional scope necessarily impacts the scale of the study which is neither at the fault scale (for example, there is no topological analysis of the faults zone), nor at the catchment scale as the elementary bulk unit. This functional scope besides impacts the methodological choices made, following the informational content of well-known data and technics. As the current approach aims at linking geological structures to hydrogeological structures, it is inevitable to acquire hydraulic-related data. For that aspect, widely-used methods based on dissolved elements (environmental tracers, water isotopes, hydrogeochemistry) are directly related to transport processes and hence to groundwater flow and hydraulic gradient. However, their inability to clearly identify local scale processes mainly due to mixing, limits their use when addressing problems related to groundwater flow architecture as it is the case here. On the contrary, baseflow measurement is an easily accessible data that can be related to local flow processes as the resolution of spatially-distributed measurements can be arbitrary fixed. Beyond this consideration, streamflow is a variable of interest in various disciplines including hydroecology. In that sense, the comprehensive methodology proposed here could be easily extended to hydroecology or hydrobiology.

The novelty of the proposed methodology lies mainly in the innovative implementation of classical methods from various disciplines that are conjointly designed and iteratively carried out. The geological study has been indeed conducted at multiple scales: at a traditional main scale (1:100,000) and at a finer scale to incorporate some elements (e.g.,

the N-E secondary fracture zone) that would confirm hydraulic observations. It results in a hybrid geological map partly fed by hydrogeological considerations. Regarding geophysical surveys, they significantly compliment the multiscale geological mapping. The inclusion of a second geophysical transect in the north of the study area (transect B-B' in Figure 4-7c) confirms the general N-S orientation and regional scale of some structures (results presented in supplementary material). Meanwhile, the UAV-based magnetic study, performed here at high-resolution in comparison to previous studies, does not only provide valuable information in remote areas but also constitutes a unifying method allowing the creation of a coherent geological model thanks to its fast and large covering.

Finally, while spatially-distributed streamflow campaigns are not commonly used in hydrology, they have shown here to be valuable to identify and confirm critical features of the baseflow evolution within the catchment. If spatially-distributed flow measurements may seem tedious, low-cost instrumentation and recently-developed optical methods could allow a systematization of measurements.

4.4. Conclusions

We propose a comprehensive methodology to unravel geological controls on groundwater flow and surface water-groundwater interaction in mountain catchments. Geological mapping, on-ground and aerial geophysics, and hydraulic data are acquired to simultaneously image geological structures and their hydrogeological manifestations.

Using the novel methodology, we identify peculiar hydric behaviours in an ungauged Andean catchment, including a significant and localized groundwater exfiltration that seems to be imported from a neighbouring subcatchment and related to the presence of a regional N-S fault and a secondary set of E-W local faults.

The novelty of the methodology mainly lies in the innovative implementation of classical methods: multi-scale geological mapping, spatially distributed streamflow measurements, high-resolution aerial geophysics. This novel methodology is distinguished by its pragmatism in that it focuses on the geological structures that are the most significant for flow without aiming to characterize the entire geological framework.

The findings have significant implications for the management and monitoring of the study site as flow singularities such as the abrupt streamflow change that may strongly affect the biogeochemical conditions in the river, like biogeochemical hotspots.

4.5. Acknowledgments

This study received financial support from the project ANID-Conicyt/Fondecyt de Iniciación n°11170380. The authors would like to thank the Pirque community for their incredible kindness, their constant support and their interest in the *HydroPirque* project. Miles y miles de gracias a la CONAF: Don Carlos, Don Luis P., Don Luis C., Doña Catalina y todos los guardaparques de la reserva. Miles de gracias también al comité de Agua Potable Rural El Principal: a la señora Nora y a Erik, a la municipalidad de Pirque y a Nicolas. Thanks to Mr. Carlos Uribe del Río Coipo: sometimes research hangs by a thread, or rather by a padlock key. The authors are thankful to the two anonymous reviewers and the associated editor for their fruitful comments that significantly improved the manuscript.

5. GEOLOGICAL STRUCTURES PERMEABILITY IMPACT ON GROUNDWATER FLOWS IN MOUNTAIN SYSTEMS: A NUMERICAL SENSITIVITY STUDY

5.1. Introduction

In recent years, there has been a growing interest in mountain catchments from the scientific community and stakeholders, acknowledging their pivotal role as crucial water reservoirs for downstream alluvial basins, as they receive substantial precipitation (Hayashi, 2020; Immerzeel et al., 2020; Somers & McKenzie, 2020; Viviroli et al., 2020). Against the backdrop of global warming, the identification of water inflows into lowland catchments becomes imperative due to increasing anthropic pressures (Amanambu et al., 2020; Gleick, 1989; Pokhrel et al., 2021; Scanlon et al., 2023; Taucare et al., 2024; Viviroli et al., 2011). Nevertheless, the intrinsic complexity of mountain systems poses challenges in their characterization and, consequently, in understanding their hydrodynamic connection to lowland aquifers. This connection, known as Mountain Front Recharge (MFR), consists of two distinct components: Surface MFR (sMFR), encompassing both perennial and ephemeral streams exiting the mountain block and subsequently infiltrating the basin fill, and Mountain Block Recharge (MBR), representing all groundwater directly entering the basin aquifer from the mountain block (Bresciani et al., 2014; Feth, 1964; Markovich et al., 2019; Taucare et al., 2020; Wilson & Guan, 2004). Moreover, groundwater flows in mountain blocks do not necessarily lead to Mountain Block Recharge (MBR). Water can both infiltrate and exfiltrate inside the mountain block, resulting in a diverse range of flow path lengths and depths, theoretically spanning from local to regional scales (Gleeson & Manning, 2008; Goderniaux et al., 2013; Tóth, 1963; Wilson & Guan, 2004). Large scale flows resulting in inter-basin exchanges can significantly impact the water balance of basins, especially in complex mountain systems (Alvarez-Campos et al., 2022; Belay et al., 2023; Fan et al., 2023; Fan, 2019; Schaller & Fan, 2009). This complexity poses a challenge in disentangling flow paths and quantifying the mountain's contribution to lowland catchments.

The intricacy of mountain systems is largely rooted in their topographical and geological heterogeneities (Condon & Maxwell, 2015; Manning & Solomon, 2005; Rapp et al.,

2020; Winter, 2001). Moreover, the inherent remoteness of these environments poses challenges to the availability of observations, particularly in characterizing the subsurface medium (Healy, 2010; Markovich et al., 2019; Viguier et al., 2018). Additionally, it is widely acknowledged that the interplay between recharge and hydraulic conductivity predominantly governs groundwater flow systems (Bresciani et al., 2014; Gleeson & Manning, 2008; Haitjema & Mitchell-Bruker, 2005), underscoring the need to enhance our understanding of subsurface conceptualization.

In the context of mountain blocks, geological heterogeneities are typically manifested as lithological discontinuities or regional-to-local scale structures, such as faults and fractures. These features give rise to significant gradients and variations in hydraulic conductivities (K) within the medium, exerting a direct influence on the circulation of groundwater flows creating for instance preferential flow paths or recharge, groundwater rerouting and flow anisotropy (Bense et al., 2013; Caine et al., 1996; Y. Fan, 2019; Leray et al., 2012; Markovich et al., 2019; Roques et al., 2022; Scibek et al., 2016; Welch & Allen, 2014).

In data-scarce and complex groundwater systems, numerical studies are a means to widely screen groundwater systems and enhance the understanding of groundwater flow processes and Mountain Front Recharge (MFR) dynamics (Markovich et al., 2019). However, in the absence of direct subsurface observations, hydraulic conductivities are often assumed to be homogeneous in more conceptual studies (Gleeson & Manning, 2008; Welch & Allen, 2012) or estimated based on surface lithology and extrapolated for the subsurface (Ball et al., 2014; Engdahl & Maxwell, 2015; Yao et al., 2017). Other studies may also consider that K typically decreases with depth in consequence to the increasing gravitational stresses (Cardenas & Jiang, 2010; Welch & Allen, 2014). Rapp et al. (2020) proposed a sensitivity study of shallow subsurface conceptualization (10 m) designed to assess the effects of such assumptions on groundwater flow circulation. They found that introducing layers with higher conductivity (K) in the shallow subsurface leads to a concentration of flow paths near the surface. However, the impact of discrete and deep structures such as faults or lithological discontinuities remains largely unknown.

Field evidences of the presence of faults and fractures at the mountain front that may influence groundwater flow is widely acknowledged (Folch & Mas-Pla, 2008; Markovich et al., 2019; Wilson & Guan, 2004), exerting a direct impact on the generation of Mountain Front Recharge (MFR) and Mountain Block Recharge (MBR). These geological features act on fluid flow as a barrier, a conduit, or a combination of both (Bense et al., 2013; Caine et al., 1996). Specifically, they can affect groundwater flow, groundwater discharge and water-table elevations (Anderson & Fairley, 2008; Bense et al., 2019; Gleeson & Novakowski, 2009; Hsu et al., 2022; Izbicki et al., 2015; Keegan-Treloar et al., 2022) with the hydraulic conductivity acting as a key parameter. Indeed, a more permeable fault zone can act as a preferential path for groundwater flows (Bense et al., 2013; Figueroa et al., 2021; Folch & Mas-Pla, 2008; Leray et al., 2012, 2013; Roques et al., 2014) while a less permeable fault zone may redirect flows, either upwards or downwards, potentially leading to groundwater resurgence or preferential infiltration (Bense et al., 2003; Chowdhury et al., 2008; Figueroa et al., 2021; Rajabpour et al., 2016). Recent studies have focused on characterizing the hydraulic conductivity of these structures to determine its impact on groundwater flows. To achieve this, diverse methodologies, including direct observations (Ameli et al., 2018; Fu et al., 2022; Xue et al., 2013), pumping test results (Dewandel et al., 2014; Lu et al., 2021; Roques et al., 2014; Yihdego et al., 2015) or geophysical methods (Ball et al., 2010; Barnes et al., 2021; Figueroa et al., 2021; Pérez-Estay et al., 2022), have been employed. However, due to the intricate nature of mountain blocks, efforts focused on specific sites pose challenges in extrapolating findings to other contexts.

To address this challenge, studies have developed numerical frameworks focusing on analytical solutions for idealized faults (Haneberg, 1995), anisotropic fault zones in multilayer aquifers (Anderson & Bakker, 2008), or heterogeneous fractures networks (Toller, 2022). However, the local scale and the dimensionality of the results pose difficulties in applying these findings to regional natural systems. While Folch and Mas-Pla (2008) explored the permeability effect of a fault zone in a defined study area using numerical modeling, the study remained in two dimensions, limiting the ability to derive more complex insights for three-dimensional natural systems. Considering this, there is

a growing need for a systematic study that investigates the influence of faults and fractures permeability on groundwater flows in real mountain systems.

The main goal of this study is to decipher how structural features and their permeability influences local to regional processes in mountain catchment. More specifically, evaluating their impact on groundwater flows at the mountain front, with a specific focus on the potential generation of Mountain Block Recharge and inter-basins exchanges. To achieve this, we propose a sensitivity study exploring a wide range of structures hydraulic conductivities, spanning from drain to barrier for groundwater flows. We investigate how those hydro-structural parameters influence key hydrological parameters such as groundwater surface water interactions, flow path lengths and residence times within an idealized study area.

Our approach employs a 3D numerical groundwater flow models deployed on the catchment of Rio Clarillo national park, located 35 kilometers southeast of Santiago, Chile (Figure 5-1a). It has been previously shown that this catchment, located at the mountain front, is influenced by faults and fractures, as evidenced by deviations in groundwater flows and interactions with surface waters (Marti, Leray, Villela, et al., 2023).

In the following section, we will first detail the distinctive characteristics of the Rio Clarillo catchment. Then we will identify the hydrological parameters for our sensitivity analysis. Following this, we will present the outcomes of our analysis drawn about the characteristics of groundwater flows in mountain front basin environments. Additionally, we will engage in a comprehensive discussion regarding the local permeability's effects on groundwater flow organization and examine how inter-basin flows within mountain catchments play a significant role in shaping hydrogeological dynamics.

5.2. Material and methods

5.2.1. Study site and modeled domain

The Rio Clarillo catchment serves as an ideal location for our study due to its strategic positioning at the mountain front, it facilitates the definition of flow scale dynamics entering the sedimentary basin (MFR). Spanning an area of 130 km^2, the catchment is situated in a semi-arid climate region.

The San Ramon fault (SRF), a major north-south (NS) structure located at the Mountain Front, has been extensively studied for its geographical significance, close to Santiago further north of the study area (Armijo et al., 2010; Díaz et al., 2014; Pérez et al., 2014; Yáñez et al., 2020). Yet in our study area, no field evidence exists for its trace. Such structures generally characterize the limit between the sedimentary aquifer and the deformed mountain block. Thus, we extend the recognized fault trace, following the mountain front, to define the inferred SRF in our study area studying its impact on groundwater flows (inf. SRF on Figure 5-1b). Two other important NS structures are identified in the study area, which defined two branches of the Papagayo fault (PGF): at the North of the catchment and limiting the southwest border of the catchment (Marti et al., 2023) (Figure 5-1b). In addition, inside the catchment, an EW fractures area (Figure 5-1b) is identified (Marti et al., 2023). Spanning across the primary river and predominantly occupying the eastern riverbank, this area holds a strategic position at a topographic low point. This location is significant as the river shifts its course from a South-North to an East-West direction. These structures may directly influence groundwater flows organization based on their potentially variable permeability contrast with the host rock (across and along strike).

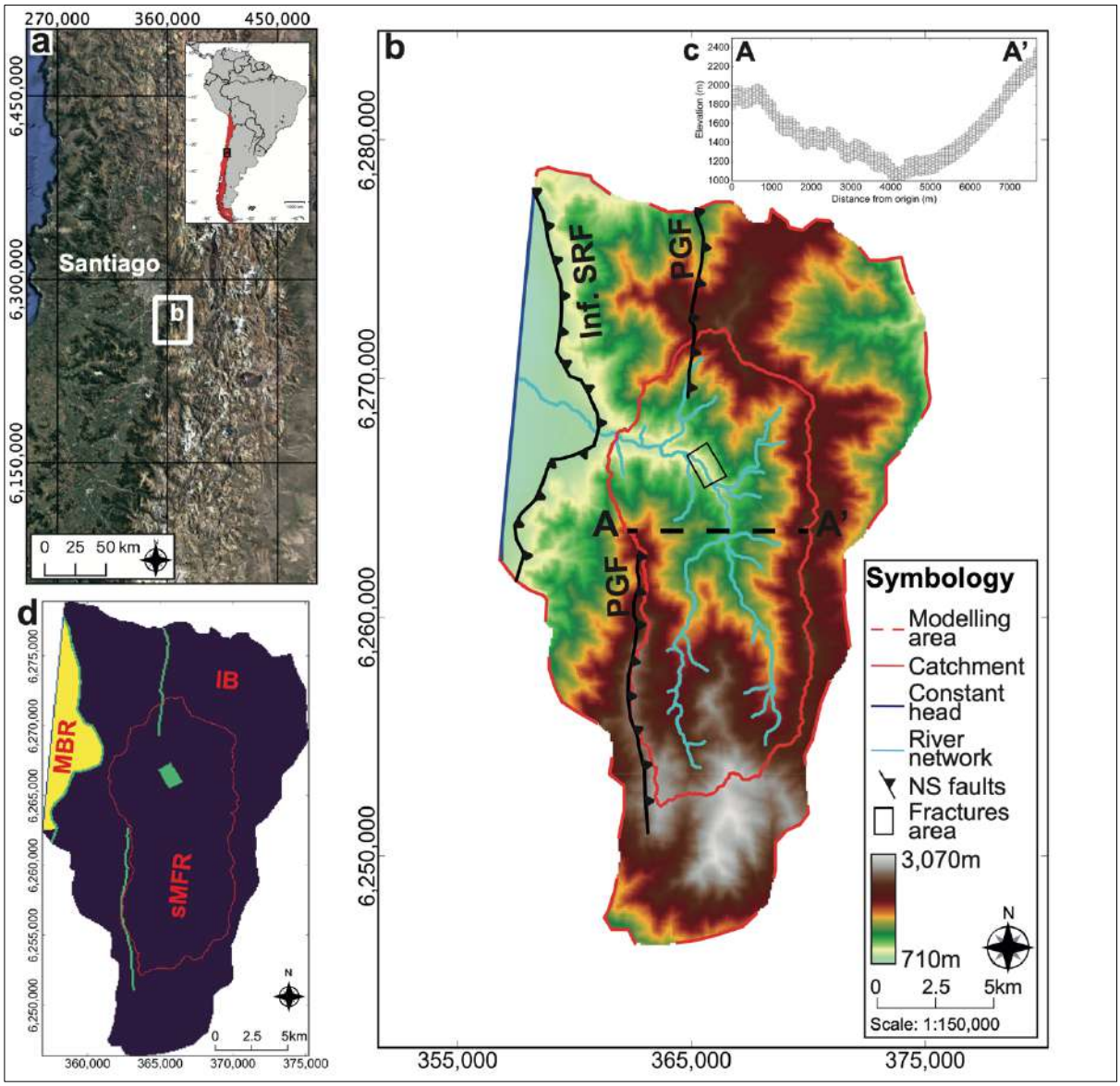

Figure 5-1 a) Situation and satellite view maps of the study area, the white rectangle corresponds to the modelled area defined on b) and d). b) Topographic map of the modelled area (borders highlighted by a dashed red line). The catchment is delimited by a red line. Faults (black lines), fractures area (black rectangle), the river network (light blue lines) and the constant head boundary condition (blue line) are overlayed. An A-A' cross-section is identified. c) Representation of the A-A' topographic cross-section with the model discretization illustrated. d) Representation of the modelled area with structures (green lines and rectangle) and hydraulic conductivities of modelled units, yellow unit for the sedimentary area ($K_{sediments}=10^{-4}$m/s) and blue for the volcanic unit ($K_{homogeneous}=1.6*10^{-7}$m/s). The corresponding exit zones are overlayed with red text (MBR: Mountain Block recharge, sMFR: surface Mountain Front Recharge and IB inter-basins).

5.2.2. Numerical modelling

To comprehensively investigate the behavior of faults and fractures within the catchment, we developed a three-dimensional numerical groundwater flow model using MODFLOW 6 (Langevin et al., 2017) and handled the model with the Python-based interface FLOPY (Bakker et al., 2016). The horizontal discretization aligns with the spatial resolution of the Shuttle Radar Topography Mission (SRTM) digital elevation model (DEM) with a 90 m resolution. For vertical discretization, we implemented ten layers of equal thickness. The overall thickness of the model is set to a constant value of 200 m so as model bottom mirrors topography. This constant thickness value is based on the generally accepted active depth for groundwater flows (Condon et al., 2020; Rapp et al., 2020; Welch & Allen, 2014). A visual representation of the model is provided in Figure 5-1c) and d), including a cross-section.

The modelled area incorporates a buffer zone (see Figure 5-1b) surrounding the catchment, located at topographic lows, functioning as groundwater divides. This design aims to alleviate the impact of no-flow boundary limits that are imposed to the south, southwest, east, and north of the buffer zone (Figure 5-1b). In the sedimentary filled area to the northwest, the boundary condition is defined as a constant head, serving as the natural outlet of our catchment. This constant head is precisely set at 40 m below the lowest topographic point, guided by piezometric data.

To simulate natural processes, we introduced a uniform potential recharge rate (R) of 100 mm/year at the water table based on the estimations made by Marti et al. (2023). Additionally, a drain was strategically positioned on the topography over the entire modelled area, employing MODFLOW's dedicated package. This drain serves a dual purpose, enabling water to either infiltrate (recharge) or exfiltrate at the surface, contributing to a more realistic representation of the groundwater dynamics in the studied catchment.

5.2.3. Establishing a reference case for the sensitivity study

In characterizing the permeability distribution within the modeled area, our initial step involved establishing a reference case devoid of considerations for faults and fractures. This foundational case serves as a reference for comparing and evaluating the impact of

geological structures. Within this reference case, we adopted a simplified dual hydraulic conductivities framework (see Figure 5-1d).

In this context, we treated the mountain block as a homogeneous volcanic unit, and its hydraulic conductivity was calibrated utilizing the methodology proposed by Abhervé et al. (2023). This method involves defining the hydraulic conductivity (K), by comparing the river network to groundwater exfiltration areas (seepage) with varying values of K/R. For our study area, the optimal match was found to be $K_{homogeneous}$= $1.6*10^{-7}$m/s, assuming a recharge of 100 mm/year. This value is found consistent with the characteristics of a fractured bedrock in volcanic mountain block unit (Freeze & Cherry, 1979; Voeckler & Allen, 2012; Welch & Allen, 2012, 2014).

Moving on to the second hydraulic conductivity, it was determined for the sedimentary area situated at the base of the mountain block (depicted as the yellow area in Figure 5-1d). The head change in the sedimentary unit between the lower head elevation at the constant head boundary and the highest point is known to be 0.5%. Consequently we can define $K_{sediments}$= 10^{-4} m/s, in accordance with general definition of the hydraulic conductivity of sedimentary layers (Freeze & Cherry, 1979).

5.2.4. Parameters space

Building upon the reference scenario, we incorporate faults and fractures identified in Figure 5-1b into the model, depicted by green lines and rectangle in Figure 5-1c. The inferred San Ramon fault is positioned at the interface between the volcanic and sedimentary units, while the Papagayo fault and the fractures area follow their respective map traces on the topographic map. Faults structures are defined as punctual and vertical, discretized along one cell on surface discretization and along the 10 layers at depth. The fractures area is defined according to its area reaching the bottom of the model.

To evaluate the role of these geological structures on groundwater flows, a sensitivity study on the contrast of hydraulic conductivities (K) is proposed as the permeability can be associated with K. We consider two ratios representing the hydraulic conductivity contrast between the fractures area and the surrounding volcanic unit: $K_{fractures}$ /$K_{homogeneous}$, and the hydraulic conductivity contrast between the faults zone and the surrounding volcanic unit K_{faults} /$K_{homogeneous}$. The iterative process of the sensitivity study

is outlined on Figure 5-2. The first step is to define the scenario related to the fractures area, three scenarios are defined: Scenario 1 excludes the fracture area, Scenario 2 incorporates a ratio $K_{fractures}/K_{homogeneous} = 10$, and Scenario 3 employs a ratio $K_{fractures}/K_{homogeneous} = 10^2$. Then for each scenario, we investigate 10 ratios of $K_{faults}/K_{homogeneous}$, spanning from 10^5 to 10^{-5}.

In total, this sensitivity study encompasses 31 simulations including the reference case.

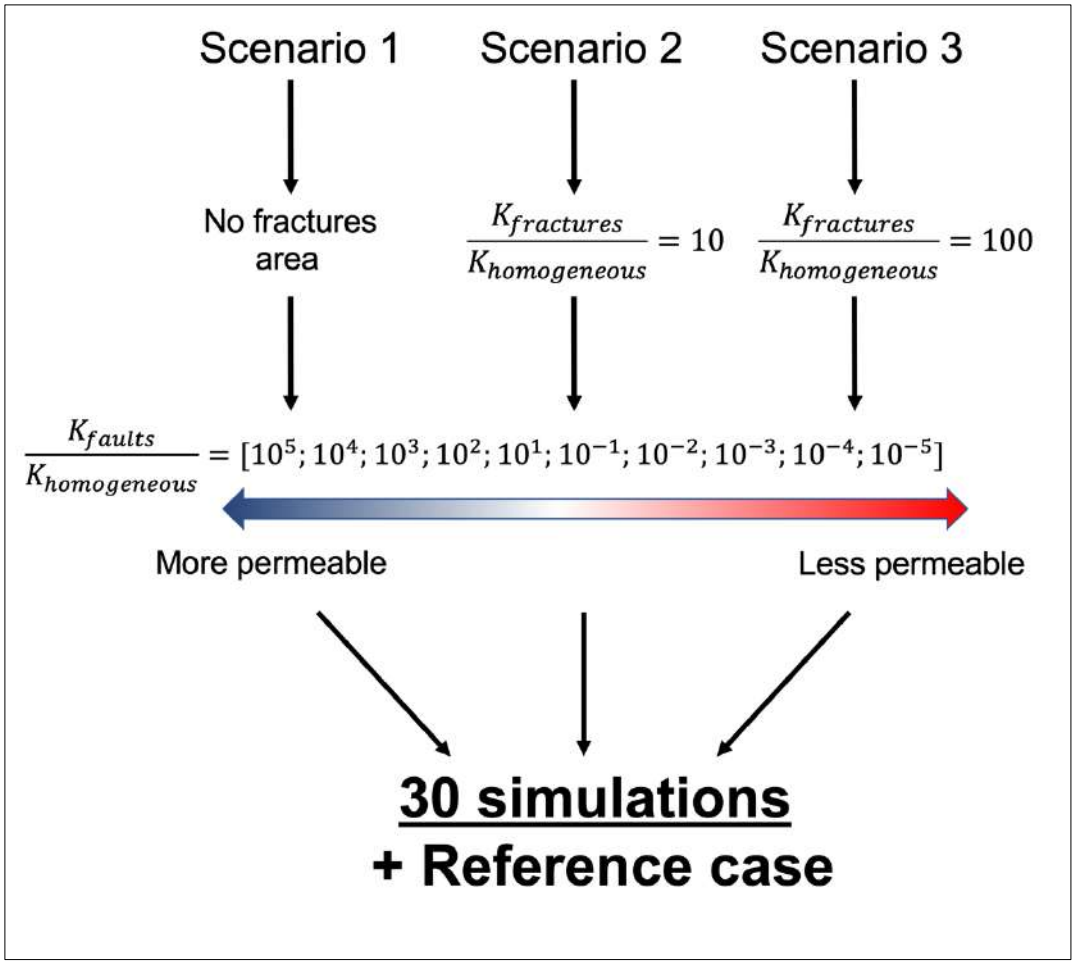

Figure 5-2 Definition and diagram of the sensitivity study, definition of the three studied scenarios. For each scenario defined according to the fractures area, we iterate 10 times on the $K_{faults}/K_{homogeneous}$ ratio. The arrow with the color gradient represents the different $K_{faults}/K_{homogeneous}$ ratio values, from the most permeable (blue) to the least permeable (red). The arrow will be repeated under results plots for references.

5.2.5. Hydrological indicators

The metrics considered in the subsequent section are derived from the groundwater model and particle tracking simulations facilitated by MODPATH 7 (Pollock, 2016). MODPATH uses the outputs generated by the groundwater flow model to trace the trajectory of each injected particle. In our methodology, a systematic approach was adopted: for each simulation, particles were introduced for every cell where water infiltrated within our catchment. Five particles were randomly injected within each cell to capture all possible flows. Particles were not injected where groundwater exfiltrates, as such instances would result in null time and length. The porosity was set at 0.15.

This particle injection strategy ensures a comprehensive framework to understand the dynamic of pathways and behaviors of groundwater, offering valuable insights into the model's responses and contributing to the robustness of our findings.

To capture the full extent of permeability effects, our analysis first focuses on relative differences (RD) between the hydraulic head in the catchment. RD will be calculated for each simulation against the reference case for each cell of the model and defined as:

$$RD = \frac{|h_{simulation} - h_{reference}|}{h_{reference}}, \qquad \text{Equation 5-1}$$

Then we defined a metric called "*Seepage Ratio*" comparing the groundwater exfiltration for each simulation against the reference case. As the relative difference it is defined for each cell of the model as:

$$Seepage\ ratio = \frac{Seepage_{simulation}}{Seepage_{reference}}. \qquad \text{Equation 5-2}$$

The seepage ratio will be >1 if the seepage flow in the cell is higher for the simulation and will be <1 if the seepage flow is higher for the reference case.

The mean relative differences and seepage ratio are calculated for representation perspectives. Head differences with the reference case will give insight on the fault zone effect on water levels, inducing local effects based on the permeability. Seepage ratio will determine how the faults and fractures impacted groundwater seepage area in the

catchment in comparison to the reference case. This will be representative of the redirection of the flows and generating potential new exfiltration or infiltration areas.

In addition, using the results of particle tracking, we investigate the path followed by the particles and therefore the flows. The particle arrival zone is defined as where each particle that infiltrate in the model will exfiltrate. We categorize the particles that ended within the catchment as sMFR; particles that travels from the catchment to the sedimentary unit as MBR; and finally, particles that exfiltrates into another nearby catchment as Inter-Basins (IB). The corresponding arrival zones are depicted on Figure 5-1d.

Finally, weighted residence times and flow paths are explored. To avoid bias, each particle is weighted by the recharge magnitude over the cell it infiltrates. Results for weighted residence times are categorize in three ranges of age that can be compared to ranges covered by commonly used environmental tracers used for field characterization: short times (0 - 70 years), characterized by CFCs or tritium/helium (Chambers et al., 2019; Cook & Solomon, 1997; Leray et al., 2012; Oster et al., 1996), intermediate ages (70 - 1,000 years) covered by ^{39}Ar dating techniques, and large ages (> 1,000 years), which can be estimated by ^{14}C dating (Cartwright et al., 2017; Geyh, 2000; Loosli & Oeschger, 1980; Mace et al., 2017).

5.3. Results

Following the described sensitivity study, we will showcase the findings from the 30 simulations using the designated metrics. To ensure clarity, the metrics and accompanying figures aim to encapsulate the comprehensive scope of the sensitivity study, with each figure presenting an aggregate result of the 30 simulations. The results will commence with an examination of head relative differences and seepage ratios, followed by an exploration of particle arrival zones, and the mean values of weighted residence times and weighted path lengths. It will be concluded with an analysis of the sorted residence times according to their category (short, intermediate, and large) and a description of pathlines behavior in the study area.

5.3.1. Head relative differences and Seepage ratio

Figure 5-3 depicts the mean head relative difference expressed as a percentage (Figure 5-3a) and the seepage ratio (Figure 5-3b) for all three scenarios and the 10 values of K_{faults} /$K_{homogeneous}$.

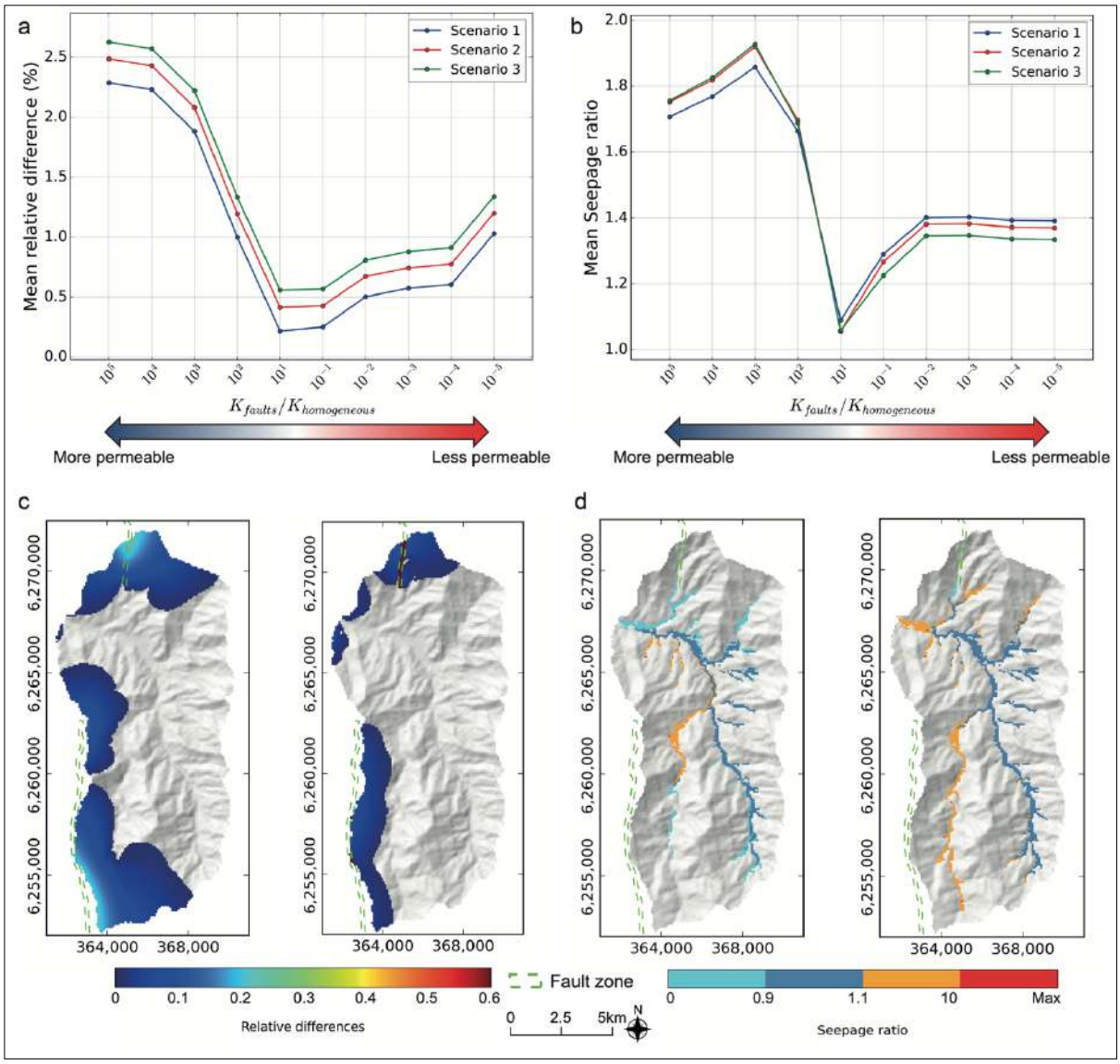

Figure 5-3 For each scenario (blue curve for scenario 1, red for scenario 2 and green for scenario 3) we plotted a) the mean relative difference (%) and b) the mean seepage ratio. Both x-axes are the K_{faults} /$K_{homogeneous}$ ranging from the more permeable case to the less permeable case with the associated gradient color arrow. Maps with topography for the more permeable case and the less permeable case of c) head relative differences (null difference is masked) and d) seepage ratio.

The relative differences plot shows that the fractures area has a direct influence on the head level in the catchment, as the mean relative difference is slightly higher for scenario 3 compared to scenario 2 and surpasses that of scenario 1 (Maps illustrating the effect of the fractures area on head relative differences for both the permeable and the impermeable case is available in the Supplementary Material). Examining the permeability of the fault zones, there is a notable increase in the mean relative difference for simulations with a more permeable fault zone (>2%), which decreases rapidly for K_{faults} /$K_{homogeneous}$ between 10^3 and 10^1. For less permeable cases, the mean relative difference increases but remains below 1.5%.

Figure 5-3c presents a map of the relative differences for the most permeable case (K_{faults} /$K_{homogeneous}$ =10^5) and the less permeable case (K_{faults} /$K_{homogeneous}$ =10^{-5}) of scenario 1, elucidating the contrast in the mean relative difference between these two cases. The most permeable case exhibits a diffusive effect on the head relative differences with overall low values, while the less permeable case demonstrates a localized effect in the fault zone with a higher value. In the permeable case, the water table elevation around the fault zone is influenced at a larger distance, but the impact is gradual with a smooth transition. Conversely, in the less permeable case, the barrier behavior of the fault zone results in a sharp change, with a high relative difference observed only in the fault zone.

In terms of the seepage ratio results (Figure 5-3b), a similar trend emerges compared to the head relative differences, with higher values observed for permeable cases compared to less permeable ones. However, in this context, the influence of the fractures area is less discernible, as the three scenarios yield similar outcomes. The seepage ratio attains a maximum value of 1.9 for the more permeable cases and maintains a stable value of 1.4 for the more impermeable cases. The stabilization of the seepage ratio suggests that further reducing the K_{faults} /$K_{homogeneous}$ ratio beyond 10^{-2} yields no additional effects. Seepage ratios exceeding 1 across all simulations confirm that introducing permeability heterogeneities in a homogeneous model modifies flow paths and generates an increase in groundwater resurgences, irrespective of permeability.

Figure 5-3d depicts a seepage ratio map for the most permeable case (K_{faults} /$K_{homogeneous}$ =10^5) and the less permeable case (K_{faults} /$K_{homogeneous}$ =10^{-5}) of scenario 1, illustrating preferential exfiltration areas in each case. Cyan color indicates a reduction in

groundwater resurgence compared to the reference case, while blue denotes no significant difference. The orange and red areas signify preferential exfiltration compared to the reference case. In the most permeable case, notable areas exhibit less seepage than the reference, with localized regions displaying increased seepage. For instance, the secondary branch of the river network in the western part of the catchment demonstrates significant groundwater resurgence before converging with the principal river branch. Upstream of this region, the loss of seepage indicates a redirection of flows influenced by the fault zone. Additionally, along the northern fault branch, seepage loss occurs due to the high permeability of the fault zone. These seepage hotspots, combined with the absence of seepage in other areas, confirm the presence of preferential paths in the more permeable case, redirecting groundwater flows to low elevation. Conversely, in the less permeable case, there is nearly no area showing lower seepage flow than for the reference case. However, parallel to the fault zones, an increase in seepage is observed. Thus, water infiltrating near the fault zone at topographic high points necessarily exfiltrates more rapidly than in the reference case, supporting the barrier effect.

Correlating both observations from Figure 5-3b and d, the higher seepage ratio for permeable cases indicates that preferential paths for groundwater flows contribute to distributing water to lower elevations, ultimately leading to exfiltration. Conversely, for impermeable cases, as observed in head relative differences, a more localized effect around the fault is expected, inducing groundwater exfiltration primarily near the contact between the fault and the surrounding unit.

5.3.2. Flows arrival zones

The subsequent results will offer an insight into the organization of groundwater flows within the mountain block by categorizing the arrival zones of injected particles. Referring to the three defined zones in the methodology (section 5.2.5), this categorization provides a glimpse into how flows rearrange due to fault zone permeability. Figure 5-4 depicts the results in bar plots, with each bar representing one simulation and results grouped based on the $K_{faults}/K_{homogeneous}$ ratio for each scenario. A map of the zones is located in the upper right corner of Figure 5-4 as a reference.

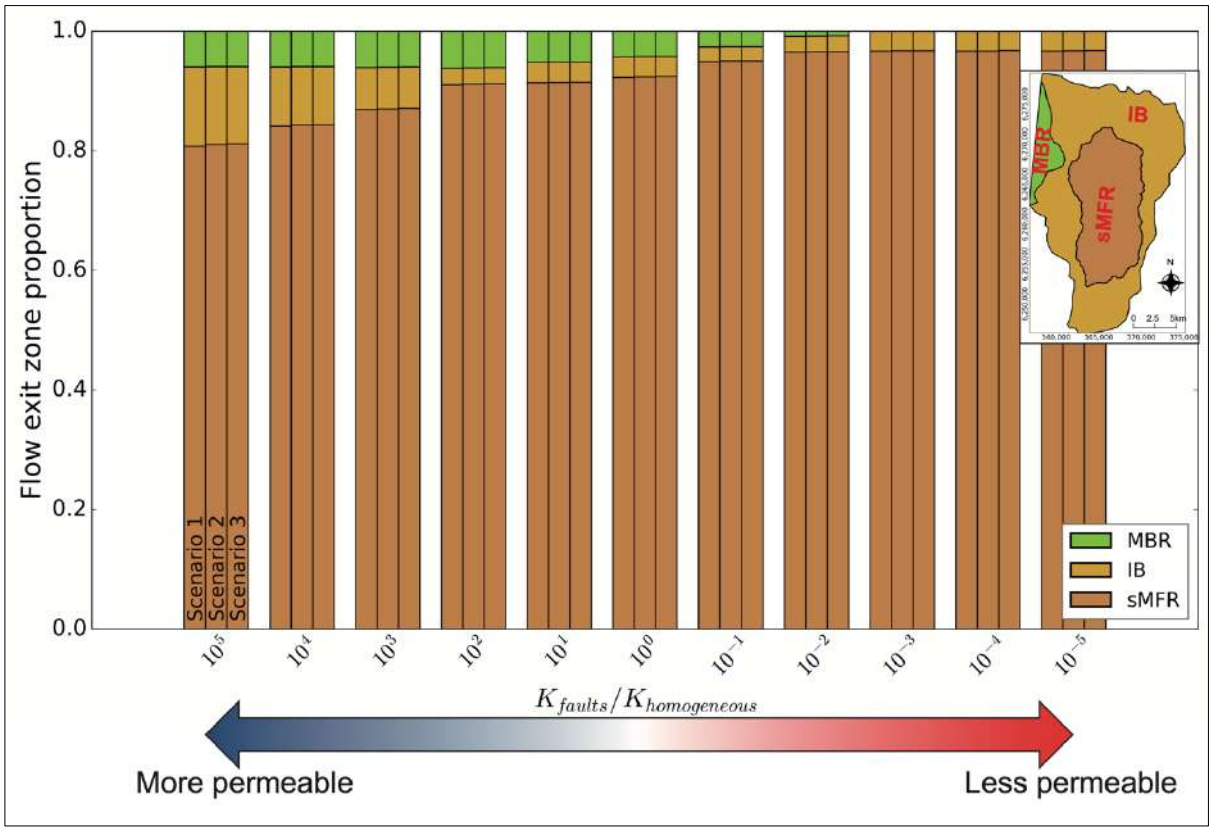

Figure 5-4 Bar-plot presenting the flow exit zone proportion based on the $K_{faults}/K_{homogeneous}$ ranging from the more permeable case to the less permeable case with the associated gradient color arrow. For each $K_{faults}/K_{homogeneous}$, bars represent one scenario each, scenario 1 to 3 from left to right, representing our 30 simulations. The ratio $K_{faults}/K_{homogeneous} = 10^{0}$ represents the reference case. The brown bar corresponds to the sMFR proportion of the total flows, the gold to the IB flows and the green one to MBR flows.

Upon observation, it becomes apparent that scenarios, and consequently the localized fractures area, exhibit no noticeable effect, indicating that the flow arrival zone is influenced more by regional effects than at the local scale. However, examining the less permeable cases reveals a trend similar to that observed in the seepage ratio (Figure 5-3b). For $K_{faults}/K_{homogeneous} < 10^{-2}$, no significant differences are noted between simulations, with approximately 98% of sMFR, around 2% of IB flows, and no MBR. In contrast, MBR predominantly occurs in permeable cases, with no discernible impact from the $K_{faults}/K_{homogeneous}$ ratio maintaining a proportion of around 5% across all permeable cases. The majority of flows infiltrate and exfiltrate within the catchment, with the sMFR proportion oscillating from 80 to 98%. Notably, the proportion of IB

flows gradually decreases with permeability reduction, ranging from around 15% to 2% for less permeable cases. The remaining 2% of IB flows are representative of catchment delineation being different from groundwater flows system limits. These observations affirm the conduit behavior for permeable fault zones and the barrier behavior for impermeable fault zones.

5.3.3. Particles residence time and flow length

To further elucidate the impact of permeability on flow paths, we present mean weighted residence times (Figure 5-5a) and flow lengths (Figure 5-5b) based on the K_{faults} /$K_{homogeneous}$ ratio for each scenario. These two metrics exhibit a correlated pattern, with more permeable cases showing longer mean residence times and flow lengths, while less permeable cases exhibit lower values. This pattern aligns with previous findings, where more permeable fault zones generate longer flow paths, acting as preferential pathways. In contrast, the barrier effect of less permeable fault zones induces shorter flow paths.

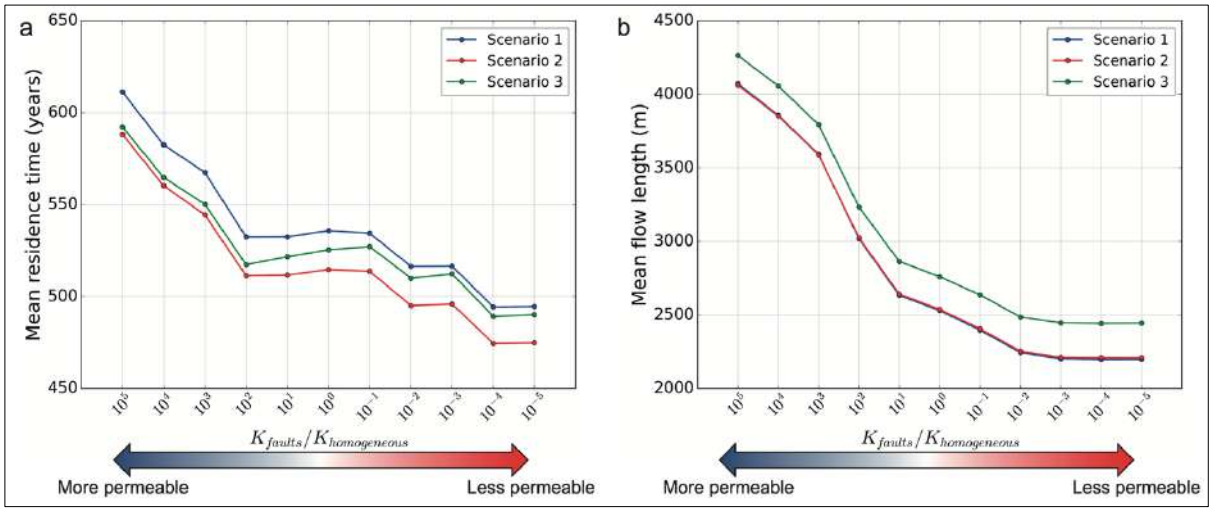

Figure 5-5 For each scenario (blue curve for scenario 1, red for scenario 2 and green for scenario 3) we plotted a) the particles weighted mean residence time (years) and b) the particles weighted mean flow path length (m). Both x-axes are the K_{faults} /$K_{homogeneous}$ ranging from the more permeable case to the less permeable case with the associated gradient color arrow. The ratio K_{faults} /$K_{homogeneous}$ = 10^0 represents the reference case.

Mean residence times range between 610 and 475 years, exhibiting a consistent decrease, yet the difference remains small. However, examining mean flow path lengths reveals a

consistent decrease until reaching the $K_{faults}/K_{homogeneous}=10^{-2}$, indicating a stabilization effect similar to that observed for the seepage ratio and flow arrival zone proportion in impermeable cases. This stabilization corresponds to a mean flow length of 2,000 m, a significant decrease from the maximum of 4,000 m in the most permeable case. To provide context, we calculated the hillslope length in our catchment to be 940 m. Flows are considered local if they are shorter than the hillslope length. In our simulations, the mean flow lengths are at least twice the hillslope length, indicating that our system is embedded in more intermediate to regional processes, with common flow between sub-catchments.

In terms of scenarios, for the more permeable cases, we observe a similarity in mean residence times (Figure 5-5a) between scenarios 2 and 3, with approximately 20 years less than scenario 1. However, as the $K_{faults}/K_{homogeneous}$ ratio decreases, scenario 3 diverges from scenario 2 and approaches scenario 1. This shift in the pattern for scenario 3 suggests a relationship between the permeability of the fractures area and the fault zones permeability. Upon closer examination of each scenario mean flow path lengths (Figure 5-5b), identical curves are observed for scenarios 1 and 2. However, for scenario 3, a constant difference of 100 m is noted for permeable cases and approximately 200 m for impermeable cases. The higher permeability of the fractures area in scenario 3 leads to longer flow lengths, locally influencing groundwater flow patterns.

5.3.4. Residence times proportion and flows organization

To delve deeper into the distribution of residence times for each scenario, we categorized them into three groups, namely short, intermediate, and large times, as outlined in section 5.2.5. The outcomes are presented through bar plots (Figure 5-6a). Consistent with previous findings, short times make up a relatively small proportion, ranging from 5 to 10% across all scenarios. Large residence times constitute between 10 and 20% of the total flows, with a higher proportion observed in the most permeable cases. Nevertheless, the predominant share of flows, approximately 70%, falls within the intermediate residence times category. The proportion of larger residence times in the more permeable cases aligns well with the arrival zone proportions (Figure 5-4), where longer residence times correspond to extended flow paths contributing to IB flows or MBR.

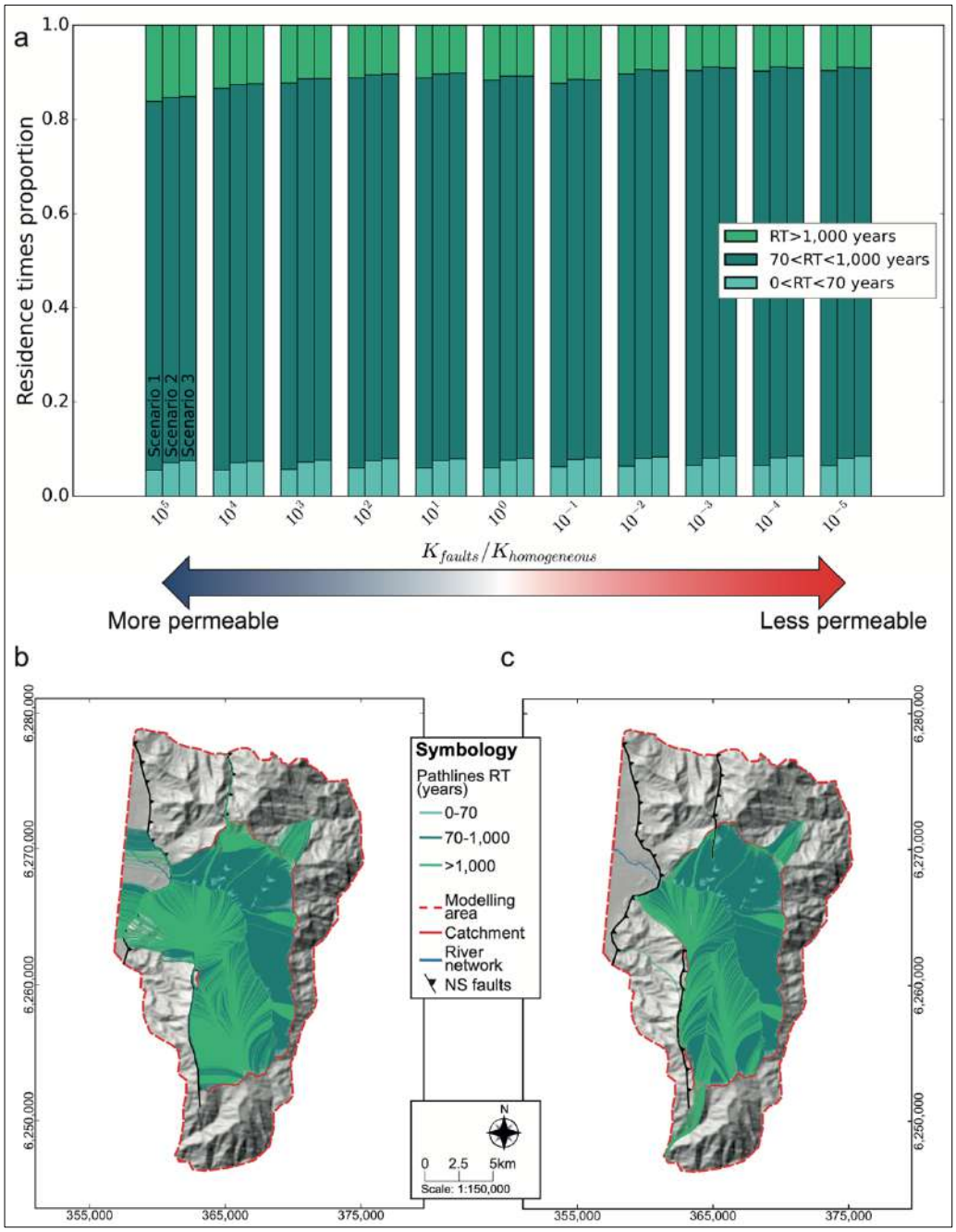

Figure 5-6 a) Bar-plot presenting the residence times proportion based on the $K_{faults}/K_{homogeneous}$ ranging from the more permeable case to the less permeable case with the associated gradient color arrow. For each $K_{faults}/K_{homogeneous}$. Bars represent one scenario each, scenario 1 to 3 from left to right, representing our 30 simulations. The ratio $K_{faults}/K_{homogeneous} = 10^{0}$ represents the reference case. The sky-blue bar corresponds to the short times, the greenish blue to intermediate times and the green one to large times. Maps of the study area overlayed with flow paths colored according to their residence times, for the more permeable case (c) and the less permeable case (d).

For a more nuanced understanding of these observations, Figure 5-6b and c depict pathlines for the more and less permeable cases, respectively. The color of the pathlines corresponds to their associated residence times, using the same color scale as the bar plots. As a general observation, in both cases, a clear demarcation between the eastern and western parts of the catchment is evident, with the primary river serving as the boundary between the two systems. The eastern region exhibits intermediate and short residence times, while the western part is predominantly characterized by large residence times. Yet, significantly different flow organizations between the two cases highlight the role of barriers or conduits formed by the fault zones.

The permeability of fault zone north of the catchment has a direct influence on residence times. For the more permeable case, the fault acting as a preferential path for groundwater flows, will export water out of the catchment and shows large residence times close to the fault. In the less permeable case, same flows are redirected to the surface generating short to intermediate residence times. Fault zone bordering the catchment at east, influences flow paths for the less permeable case, as it impedes larger flows following the regional East-West topographic gradient and redirects water inside of the catchment. Indeed, for the more permeable case, once flows reach the tip of the fault zone at its northern point, they redirect at topographic low in the sedimentary unit increasing the MBR and IB proportion. Finally, the fault zone perpendicular to the flows at the contact between the volcanic and sedimentary units, shows a barrier effect for the less permeable case, impeding flows to enter the sedimentary unit delimiting two distinct systems. For the more permeable case, flows arriving in the zone are deviated by the fault zone until entering the sedimentary unit.

Figure 5-5 presents a consistent trend of decreasing mean residence times and mean flow path lengths. While it might seem intuitive to expect longer path lengths in more permeable areas, the longer residence times in the more permeable case may appear counterintuitive at first glance. One might assume that if the flow follows a preferential path in the fault zone, which is more permeable than its surroundings, the fluid velocity should increase. However, Figure 5-6b, which illustrates flow organization in the most permeable case, sheds light on the behavior of fault zones as preferential paths without exfiltration occurring at the fault zone boundaries.

Fault zones in our study case, primarily located at topographic high points, redirect the flows along their strike. However, the flows passing through the fault zone then continue their paths and exfiltrate further downstream. This overall elongation of flow paths leads to higher mean residence times in our study case.

5.4. Discussion

Our results strongly evidenced the conduit or barrier behavior of the fault and fractures area based on the permeability. Here we discuss, the effect of the fractures area on flow path lengths and the possibility of IB flows entering the catchment to compare it to the evidenced exfiltrated IB and MBR flows.

5.4.1. Local effects – How the fractures area affects flow path lengths

In section 5.3.3, we analyzed the mean flow path lengths for each simulation (Figure 5-5b). Notably, we observed a peculiar behavior in scenario 3, where the mean flow paths consistently exceeded those of the other scenarios by 100 to 200 m in each case. This prompted us to hypothesize a local effect, potentially associated with the fractures area. Figure 5-7 presents a map of pathlines colorized based on their lengths, focusing specifically on the fractures area for each scenario.

Pathline lengths were categorized as local (hillslope length (0 – 1,000 m)), intermediate (two times the hillslope length (1,000 – 2,000 m), and regional for longer flows (> 2,000 m). Scenarios 1 and 2 exhibited similar results, with no notable influence from the absence or increased (10-times higher) permeability of the fractures area, the topographic gradient remains the main controlling factor. Yet, for scenario 3, we observe a greater representation of longer flow path length. This is particularly true observing the sub-catchment just upstream and east of the affected area. Indeed, in this catchment, we observe for the scenarios 1 and 2, mostly local to intermediate processes. Nevertheless, for the scenario 3, we observe a majority of regional flows. For the scenario 3, we also observe an impact on flow direction. In scenario 1 and 2, flows from the eastern flank of the fractures area arrived perpendicular to the river network, exfiltrating at topographic low. While for scenario 3, we observe a rotation of flow direction, parallel to the river network. These findings suggest that if the fractures area is permeable enough, it

significantly influences groundwater flows. Rather than exfiltrating at the hillslope foot, water may use the fractures area as a preferential path, leading to exfiltration further downstream. This behavior has direct implications for flow path lengths and the overall behavior of the catchment.

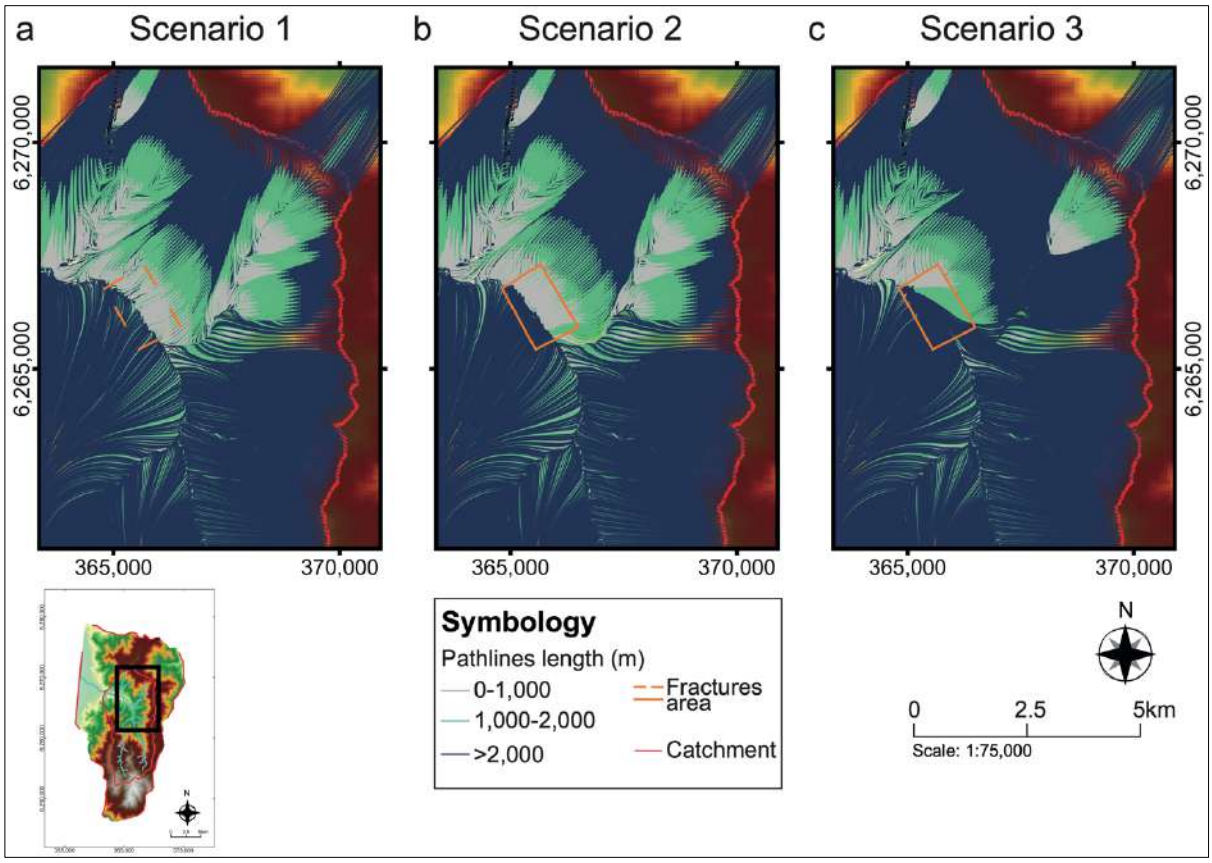

Figure 5-7 Maps zoomed on the fractures area overlayed with flow paths colored according to their length for the scenario 1 (a), the scenario 2 (b) and the scenario 3 (c). Here, the K_{faults} /$K_{homogeneous}$ is fixed at 10^{-1}. For the scenario 1, the fractures area line is dashed as it is plot only for reference perspectives.

5.4.2. Backward tracking and origin of water

We defined that the studied catchment export water, generating MBR or IB flows. We also wanted to discuss the possible inflows of water from surrounding catchments. To do so, we backtracked the flows exfiltrating in the catchment using MODPATH and determine the proportion of water coming from outside our study area. Across the 30

simulations, we found that recharge from external catchments constitutes approximately 10 to 15% of the total (detailed IB inflow bar plots provided in Supplementary Material). Figure 5-8 illustrates the flow paths of water inflows into the catchment, employing the same color scheme as previously defined based on residence times and possible tracing methods.

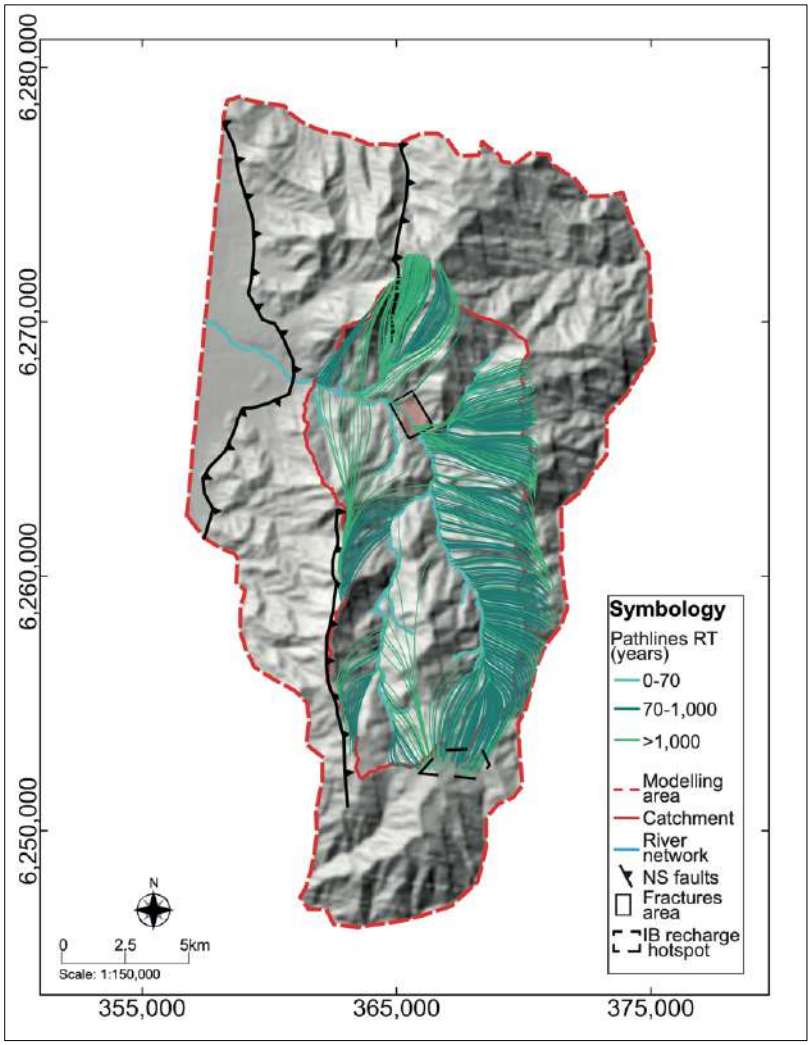

Figure 5-8 Map of the study area overlayed with flow paths colored according to their residence times for IB flows entering the basin and exfiltrating in the catchment.

Flows exhibit intermediate to large residence times, indicating longer flow paths. Examining the origin of these flow paths, we observe that they predominantly initiate near the topographic catchment limits, where delineation can be somewhat arbitrary. A

majority of the IB recharge come from the eastern border of the catchment reaching the principal river branch at topographic low.

Also, we identified a notable hotspot south of the catchment (IB recharge hotspot on Figure 5-8) that significantly contributes to the east branch of the river network. These observations hold particular significance for characterizing the origin of water using geochemical field techniques. As demonstrated earlier, relying solely on topographical limits to assess water inflows and outflows can be misleading, introducing bias to water balance evaluations. This is especially pertinent in mountainous regions, where such exchanges can reach magnitudes of up to 20% (Markovich et al., 2019).

5.5. Conclusions

In this study, we employed a 3D numerical model to explore groundwater flows in a real mountain context and investigate the impact of fault zone permeability. Our contribution extends to estimating MBR while enhancing our understanding of how fault zones permeability influences the organization of groundwater flows.

Our results evaluate the behavior of geological structures considering a wide variability of hydraulic conductivities in the fault and fractures zones, causing a redirection of the flow lines. For high permeability conditions relative to the environment, flows concentrated in the fault zones acting as a preferential path, increasing the flow path lengths. For low permeability relative to the environment, we observe a redirection of the flows.

These behaviors were evidenced through various metrics, showcasing local effects around the fault zone, influencing water levels, and regional impacts that modified groundwater exfiltration zones within the catchment, thereby extending or limiting both flow path lengths and residence times. Additionally, we discussed the local influence of the fractures area, emphasizing its potential to generate preferential flow circulation that hinders groundwater resurgences.

In the context of mountainous terrain, our study highlights that fault zones permeability significantly influences flow organization and the system capacity to generate IB exchanges or MBR. However, we also demonstrated that, on a broader scale, the

topographic limits of mountain systems are not indicative of the groundwater system alone. Inter-basin flows were present in all simulations, contributing notably to around 10 to 15% of the catchment recharge and 20 to 2% of catchment exfiltration (including MBR).

These insights offer crucial considerations for future mountain catchment characterization and field studies. The predominance of longer residence times, with minimal short times, suggests limitations in using CFC and underscores the importance of methods capable of considering extended periods (*e.g.,* ^{39}Ar or ^{14}C). Accounting for IB exchanges in water balance estimations is essential to avoid potential significant biases. Lastly, defining fault zone permeability is crucial for capturing the full behavior of the targeted catchment and the surrounding areas.

6. CONCLUSIONS AND PERSPECTIVES

This thesis presents an extensive investigation into the dynamics of groundwater flows in mountain systems and their interplay with adjacent lowland basins. Utilizing a multifaceted approach, and through three distinct yet connected chapters, the study delves into the intricate relationships between topography, geology, and hydrogeological processes. To conclude this work, an opening of the work is presented, connecting the results to the initial questions and hypotheses. Finally, perspectives to extend this work in mountain hydrogeology are presented.

6.1. Generalizing results to gain perspective on mountain systems

The main goal of this thesis was to have a better understanding of groundwater flows in mountain systems and their relationship with lowland basins. The following paragraphs engage in a discussion of the significance of the results and their relationship to the hypotheses.

Following the thesis development, it starts with the chapter 3 presenting the role of the topography, and the role of desaturation with the presented K/R ratio on groundwater dependent ecosystems. Then, chapter 4 introduces structural features and their impact on groundwater-surface water interactions. Leading us to refined numerical models based on real world topography and structures in chapter 5 contemplating the efforts made in the first two chapters.

Chapter 3 shows a general approach working on a wide variety of catchments along Central and Northern Chile studying the influence of topography on aquifer desaturation. It reveals that 3D aquifer desaturation is highly influenced by the catchment topography. Slope contrasts between flat and steep areas is the primary determinant with the landscape shape exerting a secondary control. Focusing on mountain catchments, they face increased vulnerability, attributed to quick desaturation rates.

Chapter 4 introduces a novel field approach combining multiscale geological mapping, geophysics, and hydrological data. It successfully identified a geologically controlled resurgence in an ungauged Andean catchment. It also helped solidify the connection between geological structures and hydrogeological processes.

Chapter 5 furthers this by employing a sensitivity study to delineate the impact of the hydraulic conductivity of geological structures. The overall K/R ratio of the developed models is calibrated against seepage areas, following insights from chapter 3. Results offer a wide variety of metrics giving an overall better understanding of groundwater flows organization in the mountain block. Modelling results allow to give an estimation of MBR proportion in the total MFR and reveal a non-negligible proportion of inter catchment flows. These findings challenge conventional definitions of groundwater system boundaries, which are often based solely on surface considerations such as hydrological catchment.

Chapter 3 explores extensively the K/R ratio presenting it as a desaturation function. As the K/R ratio increases, the interaction between groundwater and the topography significantly decreases, making it the principal constraint on water table elevation. For low K/R ratios, we observe a higher water table interacting with the topography inducing local flows. On the contrary, for high K/R ratio, this interaction tends to diminish, resulting in regional flows and a reorganization of groundwater flows that eventually exfiltrate at specific reduced locations.

Furthermore, our study thoroughly investigates the influence of topography as a driving force. Notably, the topography's wavelength (λ_T) plays a crucial role in determining the distribution between sMFR and MBR. A steep slope catchment with a large topography wavelength λ_T, will commonly be disconnected from the topography excepted at the lower point of the catchment inducing regional flows and therefore MBR. However, for catchments with shorter topography wavelengths, typically a mountain catchment with incised valleys and varied landscapes, we observe at topographic lows a persistence of groundwater interactions with the topography, ultimately generating sMFR from local flows.

Chapter 4 shows using field methodologies the difficulty of constraining the active depth of groundwater flows. We observe with geological and geophysical methods an important proportion of weathering within the catchment that was not previously mapped. The uncertainty on the affected depth limits the definition of the active depth and the extent of the low K zone. Nevertheless, chapters 4 and 5 demonstrate the effects of high or low hydraulic conductivities on flow organization. In chapter 4, the observed

groundwater resurgence is associated to a network of fractures and local faults that seemingly increases the hydraulic conductivity and creates preferential flow paths. In chapter 5, the differentiation between high and low hydraulic conductivities is constrained. It shows that faults and fractures zone with high hydraulic conductivity will indeed induce longer flow paths and MBR while zones with low hydraulic conductivity will induce local flows.

6.2. General remarks and paths to explore

This study embarked on the ambitious journey of shedding light on the intricate relationship between topography, climate, and geology within mountainous systems. It meticulously examined each of these driving factors, establishing meaningful connections and putting forth conceptual hydrogeological models that extend beyond the traditional 2D conceptual framework into the realm of complex 3D systems. At the first order, the impact of the topography could be highly decisive to determine a mountain system functioning, as an equivalence between the climate and the hydraulic conductivity can be expected. Yet, geological heterogeneities can directly dictate groundwater flow patterns, spanning from local to regional scales. Moreover, catchments with low recharge rate in arid regions already show low water table level with small interactions with the surface waters. Ultimately, it should be acknowledge that the definition of landscapes within mountain systems is primarily governed by tectonic and erosion processes, sculpting the topography, and forging intricate bonds between topography, geology, and climate. Regarding the impact of mountain systems on lowland basins, some patterns emerge with systematic contributions observed. Geological heterogeneities, notably faults and fractures, emerge as pivotal determinants in the potential generation of Mountain Block Recharge. To fully grasp the behavior of mountain groundwater systems and their potential influence on lowland catchments, a global perspective is imperative.

In the future, the necessity to consider these systems is evident to get a better estimation of the recharge to lowlands aquifers. In this pursuit, an increased focus on characterizing subsurface geological heterogeneities is necessary. While remote sensing has significantly advanced our understanding of real-time climate and topography, the

subsurface realm remains the most enigmatic piece of the puzzle. Geophysical techniques offer a solid foundation for obtaining indirect observations, and with the increasing utilization of drones, their applicability extends to remote locations in shorter timeframes. However, given the profound range of hydraulic conductivities encountered in fault zones and their potential to profoundly influence groundwater flows, direct observations through wells and pumping tests should be seriously contemplated in these areas. Moreover, as computational power continues to surge along with the advances in parallel computing, the development of fully integrated groundwater models based on robust geological frameworks should be pursued in critical study areas to estimate water resources accurately. In order to comprehensively assess the impact of climate change, it is imperative for this modeling endeavor to account for the transient effects of climate change. The simulations must be designed to consider the globally projected rise in temperatures and the increasing frequency of extreme precipitation events, as opposed to the traditionally seasonal distribution of rainfall. Ultimately, fostering collaboration across disciplines, spanning from climatology and remote sensing to geology and hydrogeology, holds the key to advancing our comprehensive understanding of global mountain systems.

7. REFERENCES

Abbott, R. E., & Louie, J. N. (2000). Depth to bedrock using gravimetry in the Reno and Carson City, Nevada, area basins. *Geophysics*, *65*(2), 340–350. https://doi.org/10.1190/1.1444730

Abhervé, R., Roques, C., Gauvain, A., Longuevergne, L., Louaisil, S., Aquilina, L., & De Dreuzy, J.-R. (2023). Calibration of groundwater seepage against the spatial distribution of the stream network to assess catchment-scale hydraulic properties. *Hydrology and Earth System Sciences*, *27*(17), 3221–3239. https://doi.org/10.5194/hess-27-3221-2023

Aceituno, P., Boisier, J. P., Garreaud, R., Rondanelli, R., & Rutllant, J. A. (2021). Climate and Weather in Chile. In B. Fernández & J. Gironás (Eds.), *Water Resources of Chile* (Vol. 8, pp. 7–29). Springer International Publishing. https://doi.org/10.1007/978-3-030-56901-3_2

Acharya, B. S., Bhandari, M., Bandini, F., Pizarro, A., Perks, M., Joshi, D. R., Wang, S., Dogwiler, T., Ray, R. L., Kharel, G., & Sharma, S. (2021). Unmanned Aerial Vehicles in Hydrology and Water Management: Applications, Challenges, and Perspectives. *Water Resources Research*, *57*(11). https://doi.org/10.1029/2021WR029925

Adler, C., Huggel, C., Orlove, B., & Nolin, A. (2019). Climate change in the mountain cryosphere: Impacts and responses. *Regional Environmental Change*, *19*(5), 1225–1228. https://doi.org/10.1007/s10113-019-01507-6

Alvarez-Campos, O., Olson, E. J., Welp, L. R., Frisbee, M. D., Zuñiga Medina, S. A., Díaz Rodríguez, J., Roque Quispe, W. R., Salazar Mamani, C. I., Arenas Carrión, M. R., Jara, J. M., Ccanccapa-Cartagena, A., & Jafvert, C. T. (2022). Evidence for high-elevation salar recharge and interbasin groundwater flow in the Western Cordillera of the Peruvian Andes. *Hydrology and Earth System Sciences*, *26*(2), 483–503. https://doi.org/10.5194/hess-26-483-2022

Alvarez-Garreton, C., Boisier, J. P., Garreaud, R., Seibert, J., & Vis, M. (2021). Progressive water deficits during multiyear droughts in basins with long hydrological memory in Chile. *Hydrology and Earth System Sciences*, *25*(1), 429–446. https://doi.org/10.5194/hess-25-429-2021

Amanambu, A. C., Obarein, O. A., Mossa, J., Li, L., Ayeni, S. S., Balogun, O., Oyebamiji, A., & Ochege, F. U. (2020). Groundwater system and climate change: Present status and future considerations. *Journal of Hydrology*, *589*, 125163. https://doi.org/10.1016/j.jhydrol.2020.125163

Ameli, A. A., Gabrielli, C., Morgenstern, U., & McDonnell, J. J. (2018). Groundwater Subsidy From Headwaters to Their Parent Water Watershed: A Combined Field-Modeling Approach. *Water Resources Research*, *54*(7), 5110–5125. https://doi.org/10.1029/2017WR022356

Andermann, C., Longuevergne, L., Bonnet, S., Crave, A., Davy, P., & Gloaguen, R. (2012). Impact of transient groundwater storage on the discharge of Himalayan rivers. *Nature Geoscience*, *5*(2), 127–132. https://doi.org/10.1038/ngeo1356

Anderson, E., & Bakker, M. (2008). Groundwater flow through anisotropic fault zones in multiaquifer systems. *Water Resources Research*, *44*(11). https://doi.org/10.1029/2008WR006925

Anderson, T. R., & Fairley, J. P. (2008). Relating permeability to the structural setting of a fault-controlled hydrothermal system in southeast Oregon, USA. *Journal of Geophysical Research: Solid Earth*, *113*(B5), 2007JB004962. https://doi.org/10.1029/2007JB004962

Antonelli, A., Kissling, W. D., Flantua, S. G. A., Bermúdez, M. A., Mulch, A., Muellner-Riehl, A. N., Kreft, H., Linder, H. P., Badgley, C., Fjeldså, J., Fritz, S. A., Rahbek, C., Herman, F., Hooghiemstra, H., & Hoorn, C. (2018). Geological and climatic influences on mountain biodiversity. *Nature Geoscience*, *11*(10), 718–725. https://doi.org/10.1038/s41561-018-0236-z

Araya Vargas, J., Gil, P. M., Meza, F. J., Yáñez, G., Menanno, G., Garcia-Gutierrez, V., Luque, A. J., Poblete, F., Figueroa, R., Maringue, J., Perez-Estay, N., & Sanhueza, J. (2021). Soil electrical resistivity monitoring as a practical tool for evaluating irrigation systems efficiency at the orchard scale: A case study in a vineyard in Central Chile. *Irrigation Science*, *39*(1), 123–143. https://doi.org/10.1007/s00271-020-00708-w

Armijo, R., Lacassin, R., Coudurier-Curveur, A., & Carrizo, D. (2015). Coupled tectonic evolution of Andean orogeny and global climate. *Earth-Science Reviews*, *143*, 1–35. https://doi.org/10.1016/j.earscirev.2015.01.005

Armijo, R., Rauld, R., Thiele, R., Vargas, G., Campos, J., Lacassin, R., & Kausel, E. (2010). The West Andean Thrust, the San Ramón Fault, and the seismic hazard for Santiago, Chile. *Tectonics*, *29*(2), n/a-n/a. https://doi.org/10.1029/2008TC002427

Bakker, M., Post, V., Langevin, C. D., Hughes, J. D., White, J. T., Starn, J. J., & Fienen, M. N. (2016). Scripting MODFLOW Model Development Using Python and FloPy. *Groundwater*, *54*(5), 733–739. https://doi.org/10.1111/gwat.12413

Ball, L. B., Caine, J. S., & Ge, S. (2014). Controls on groundwater flow in a semiarid folded and faulted intermountain basin. *Water Resources Research*, *50*(8), 6788–6809. https://doi.org/10.1002/2013WR014451

Ball, L. B., Ge, S., Caine, J. S., Revil, A., & Jardani, A. (2010). Constraining fault-zone hydrogeology through integrated hydrological and geoelectrical analysis. *Hydrogeology Journal*, *18*(5), 1057–1067. https://doi.org/10.1007/s10040-010-0587-z

Ballester, C., Brinkhoff, J., Quayle, W. C., & Hornbuckle, J. (2019). Monitoring the Effects of Water Stress in Cotton using the Green Red Vegetation Index and Red Edge Ratio. *Remote Sensing*, *11*(7), 873. https://doi.org/10.3390/rs11070873

Baraer, M., McKenzie, J., Mark, B. G., Gordon, R., Bury, J., Condom, T., Gomez, J., Knox, S., & Fortner, S. K. (2015). Contribution of groundwater to the outflow from ungauged glacierized catchments: A multi-site study in the tropical Cordillera Blanca, Peru. *Hydrological Processes*, *29*(11), 2561–2581. https://doi.org/10.1002/hyp.10386

Barnes, H., Hinojosa, J. R., Spinelli, G. A., Mozley, P. S., Koning, D., Sproule, T. G., & Wilson, J. L. (2021). Detecting fault zone characteristics and paleovalley incision using electrical resistivity: Loma Blanca Fault, New Mexico. *GEOPHYSICS*, *86*(3), B209–

B221. https://doi.org/10.1190/geo2020-0375.1

Barnett, T. P., Adam, J. C., & Lettenmaier, D. P. (2005). Potential impacts of a warming climate on water availability in snow-dominated regions. *Nature*, *438*(7066), 303–309. https://doi.org/10.1038/nature04141

Belay, A. S., Yenehun, A., Nigate, F., Nigussie, W., Tilahun, S. A., Dessie, M., Moges, M. M., Chen, M., Adgo, E., Fentie, D., Nyssen, J., & Walraevens, K. (2023). Investigation of interbasin groundwater flow using multiple approaches: The case of the Tana and Beles basins, Ethiopia. *Hydrogeology Journal*, *31*(8), 2251–2270. https://doi.org/10.1007/s10040-023-02724-4

Beniston, M. (2003). Climatic change in mountain regions: A review of possible impacts. *Climatic Change*, *59*(1–2), 5–31. https://doi.org/10.1023/A:1024458411589

Bense, V. F., Gleeson, T., Loveless, S. E., Bour, O., & Scibek, J. (2013). Fault zone hydrogeology. *Earth-Science Reviews*, *127*, 171–192. https://doi.org/10.1016/j.earscirev.2013.09.008

Bense, V. F., Kasse, C., Lapperre, R. E., Van Balen, R. T., & Woolderink, H. A. G. (2019). An overview of fault zone permeabilities and groundwater level steps in the Roer Valley Rift System. *Netherlands Journal of Geosciences*, *98*, e5. Cambridge Core. https://doi.org/10.1017/njg.2019.4

Bense, V. F., Van Den Berg, E. H., & Van Balen, R. T. (2003). Deformation mechanisms and hydraulic properties of fault zones in unconsolidated sediments; the Roer Valley Rift System, The Netherlands. *Hydrogeology Journal*, *11*(3), 319–332. https://doi.org/10.1007/s10040-003-0262-8

Beven, K. (2001). How far can we go in distributed hydrological modelling? *Hydrology and Earth System Sciences*, *5*(1), 1–12. https://doi.org/10.5194/hess-5-1-2001

Binley, A., Hubbard, S. S., Huisman, J. A., Revil, A., Robinson, D. A., Singha, K., & Slater, L. D. (2015). The emergence of hydrogeophysics for improved understanding of subsurface processes over multiple scales. *Water Resources Research*, *51*(6), 3837–3866. https://doi.org/10.1002/2015WR017016

Bishop, K., Buffam, I., Erlandsson, M., Folster, J., Laudon, H., Seibert, J., & Temnerud, J. (2008). Aqua Incognita: The unknown headwaters. *Hydrological Processes*, *22*(8), 1239–1242. https://doi.org/10.1002/hyp.7049

Blakely, R. J. (1995). *Potential Theory in Gravity and Magnetic Applications* (1st ed.). Cambridge University Press. https://doi.org/10.1017/CBO9780511549816

Blin, N., Hausner, M., Leray, S., Lowry, C., & Suárez, F. (2022). Potential impacts of climate change on an aquifer in the arid Altiplano, northern Chile: The case of the protected wetlands of the Salar del Huasco basin. *Journal of Hydrology: Regional Studies*, *39*, 100996. https://doi.org/10.1016/j.ejrh.2022.100996

Bresciani, E., Cranswick, R. H., Banks, E. W., Batlle-Aguilar, J., Cook, P. G., & Batelaan, O. (2018). Using hydraulic head, chloride and electrical conductivity data to distinguish between mountain-front and mountain-block recharge to basin aquifers. *Hydrology and Earth System Sciences*, *22*(2), 1629–1648. https://doi.org/10.5194/hess-22-1629-2018

Bresciani, E., Davy, P., & de Dreuzy, J.-R. (2014). Is the Dupuit assumption suitable for predicting the groundwater seepage area in hillslopes? *Water Resources Research*, *50*(3), 2394–2406. https://doi.org/10.1002/2013WR014284

Bresciani, E., Gleeson, T., Goderniaux, P., De Dreuzy, J. R., Werner, A. D., Wörman, A., Zijl, W., & Batelaan, O. (2016). Groundwater flow systems theory: Research challenges beyond the specified-head top boundary condition. *Hydrogeology Journal*, *24*(5), 1087–1090. https://doi.org/10.1007/s10040-016-1397-8

Bresciani, E., Goderniaux, P., & Batelaan, O. (2016). Hydrogeological controls of water table-land surface interactions: Water Table-Land Surface Interactions. *Geophysical Research Letters*, *43*(18), 9653–9661. https://doi.org/10.1002/2016GL070618

Brunner, P., Cook, P. G., & Simmons, C. T. (2009). Hydrogeologic controls on disconnection between surface water and groundwater. *Water Resources Research*, *45*(1). https://doi.org/10.1029/2008WR006953

Brunner, P., Simmons, C. T., & Cook, P. G. (2009). Spatial and temporal aspects of the transition from connection to disconnection between rivers, lakes and groundwater. *Journal of Hydrology*, *376*(1–2), 159–169. https://doi.org/10.1016/j.jhydrol.2009.07.023

Brunner, P., Therrien, R., Renard, P., Simmons, C. T., & Franssen, H.-J. H. (2017). Advances in understanding river-groundwater interactions: River-Groundwater Interactions. *Reviews of Geophysics*, *55*(3), 818–854. https://doi.org/10.1002/2017RG000556

Cai, W., McPhaden, M. J., Grimm, A. M., Rodrigues, R. R., Taschetto, A. S., Garreaud, R. D., Dewitte, B., Poveda, G., Ham, Y.-G., Santoso, A., Ng, B., Anderson, W., Wang, G., Geng, T., Jo, H.-S., Marengo, J. A., Alves, L. M., Osman, M., Li, S., … Vera, C. (2020). Climate impacts of the El Niño–Southern Oscillation on South America. *Nature Reviews Earth & Environment*, *1*(4), 215–231. https://doi.org/10.1038/s43017-020-0040-3

Caine, J. S., Evans, J. P., & Forster, C. B. (1996). Fault zone architecture and permeability structure. *Geology*, *24*(11), 1025. https://doi.org/10.1130/0091-7613(1996)024<1025:FZAAPS>2.3.CO;2

Cardenas, M. B., & Jiang, X. (2010). Groundwater flow, transport, and residence times through topography-driven basins with exponentially decreasing permeability and porosity. *Water Resources Research*, *46*(11), 2010WR009370. https://doi.org/10.1029/2010WR009370

Carlier, C., Wirth, S. B., Cochand, F., Hunkeler, D., & Brunner, P. (2019). Exploring Geological and Topographical Controls on Low Flows with Hydrogeological Models: Exploring Geological and Topographical Controls on Low Flows with Hydrogeological Models. *Groundwater*, *57*(1), 48–62. https://doi.org/10.1111/gwat.12845

Carrera, J., Alcolea, A., Medina, A., Hidalgo, J., & Slooten, L. J. (2005). Inverse problem in hydrogeology. *Hydrogeology Journal*, *13*(1), 206–222. https://doi.org/10.1007/s10040-004-0404-7

Cartwright, I., Cendón, D., Currell, M., & Meredith, K. (2017). A review of radioactive isotopes and other residence time tracers in understanding groundwater recharge:

Possibilities, challenges, and limitations. *Journal of Hydrology*, *555*, 797–811. https://doi.org/10.1016/j.jhydrol.2017.10.053

Chambers, L. A., Gooddy, D. C., & Binley, A. M. (2019). Use and application of CFC-11, CFC-12, CFC-113 and SF6 as environmental tracers of groundwater residence time: A review. *Geoscience Frontiers*, *10*(5), 1643–1652. https://doi.org/10.1016/j.gsf.2018.02.017

Charrier, R., Baeza, O., Elgueta, S., Flynn, J. J., Gans, P., Kay, S. M., Muñoz, N., Wyss, A. R., & Zurita, E. (2002). Evidence for Cenozoic extensional basin development and tectonic inversion south of the flat-slab segment, southern Central Andes, Chile (33°–36°S.L.). *Journal of South American Earth Sciences*, *15*(1), 117–139. https://doi.org/10.1016/S0895-9811(02)00009-3

Charrier, R., Pinto, L., & Rodríguez, M. P. (2007). Tectonostratigraphic evolution of the Andean Orogen in Chile. In T. Moreno & W. Gibbons (Eds.), *The Geology of Chile* (First, pp. 21–114). The Geological Society of London. https://doi.org/10.1144/GOCH.3

Choi, J.-H., Edwards, P., Ko, K., & Kim, Y.-S. (2016). Definition and classification of fault damage zones: A review and a new methodological approach. *Earth-Science Reviews*, *152*, 70–87. https://doi.org/10.1016/j.earscirev.2015.11.006

Chowdhury, A. H., Uliana, M., & Wade, S. (2008). Ground Water Recharge and Flow Characterization Using Multiple Isotopes. *Groundwater*, *46*(3), 426–436. https://doi.org/10.1111/j.1745-6584.2008.00443.x

Christelis, V., & Hughes, A. G. (2018). Metamodel-assisted analysis of an integrated model composition: An example using linked surface water – groundwater models. *Environmental Modelling & Software*, *107*, 298–306. https://doi.org/10.1016/j.envsoft.2018.05.004

Christensen, C. W., Hayashi, M., & Bentley, L. R. (2020). Hydrogeological characterization of an alpine aquifer system in the Canadian Rocky Mountains. *Hydrogeology Journal*, *28*(5), 1871–1890. https://doi.org/10.1007/s10040-020-02153-7

Clarke, A., Mac Nally, R., Bond, N., & Lake, P. S. (2008). Macroinvertebrate diversity in headwater streams: A review. *Freshwater Biology*, *53*(9), 1707–1721. https://doi.org/10.1111/j.1365-2427.2008.02041.x

Cochand, M., Christe, P., Ornstein, P., & Hunkeler, D. (2019). Groundwater Storage in High Alpine Catchments and Its Contribution to Streamflow. *Water Resources Research*, *55*(4), 2613–2630. https://doi.org/10.1029/2018WR022989

Coira, B., Davidson, J., Mpodozis, C., & Ramos, V. (1982). Tectonic and magmatic evolution of the Andes of northern Argentina and Chile. *Earth-Science Reviews*, *18*(3–4), 303–332. https://doi.org/10.1016/0012-8252(82)90042-3

Condon, L. E., Markovich, K. H., Kelleher, C. A., McDonnell, J. J., Ferguson, G., & McIntosh, J. C. (2020). Where Is the Bottom of a Watershed? *Water Resources Research*, *56*(3), e2019WR026010. https://doi.org/10.1029/2019WR026010

Condon, L. E., & Maxwell, R. M. (2015). Evaluating the relationship between topography and groundwater using outputs from a continental-scale integrated hydrology model. *Water Resources Research*, *51*(8), 6602–6621.

https://doi.org/10.1002/2014WR016774

Cook, P. G., & Solomon, D. K. (1997). Recent advances in dating young groundwater: Chlorofluorocarbons, and 85Kr. *Journal of Hydrology*, *191*(1–4), 245–265. https://doi.org/10.1016/S0022-1694(96)03051-X

Cornette, N., Roques, C., Boisson, A., Courtois, Q., Marçais, J., Launay, J., Pajot, G., Habets, F., & de Dreuzy, J.-R. (2022). Hillslope-scale exploration of the relative contribution of base flow, seepage flow and overland flow to streamflow dynamics. *Journal of Hydrology*, *610*, 127992. https://doi.org/10.1016/j.jhydrol.2022.127992

Cuthbert, M. O., Gleeson, T., Moosdorf, N., Befus, K. M., Schneider, A., Hartmann, J., & Lehner, B. (2019). Global patterns and dynamics of climate–groundwater interactions. *Nature Climate Change*, *9*(2), 137–141. https://doi.org/10.1038/s41558-018-0386-4

Dahlin, T. (2001). The development of DC resistivity imaging techniques. *Computers & Geosciences*, *27*(9), 1019–1029. https://doi.org/10.1016/S0098-3004(00)00160-6

Dai, A. (2013). Increasing drought under global warming in observations and models. *Nature Climate Change*, *3*(1), 52–58. https://doi.org/10.1038/nclimate1633

Devauchelle, O., Petroff, A. P., Seybold, H. F., & Rothman, D. H. (2012). Ramification of stream networks. *Proceedings of the National Academy of Sciences*, *109*(51), 20832–20836. https://doi.org/10.1073/pnas.1215218109

Dewandel, B., Aunay, B., Maréchal, J. C., Roques, C., Bour, O., Mougin, B., & Aquilina, L. (2014). Analytical solutions for analysing pumping tests in a sub-vertical and anisotropic fault zone draining shallow aquifers. *Journal of Hydrology*, *509*, 115–131. https://doi.org/10.1016/j.jhydrol.2013.11.014

Díaz, D., Maksymowicz, A., Vargas, G., Vera, E., Contreras-Reyes, E., & Rebolledo, S. (2014). Exploring the shallow structure of the San Ramón thrust fault in Santiago, Chile (~33.5° S), using active seismic and electric methods. *Solid Earth*, *5*(2), 837–849. https://doi.org/10.5194/se-5-837-2014

DMC. (2023). *Dirección Meteorológica de Chile*. Https://Climatologia.Meteochile.Gob.Cl/.

D'Odorico, P., Bhattachan, A., Davis, K. F., Ravi, S., & Runyan, C. W. (2013). Global desertification: Drivers and feedbacks. *Advances in Water Resources*, *51*, 326–344. https://doi.org/10.1016/j.advwatres.2012.01.013

Dumont, M., Reninger, P. A., Aunay, B., Pryet, A., Jougnot, D., Join, J. L., Michon, L., & Martelet, G. (2021). Hydrogeophysical Characterization in a Volcanic Context From Local to Regional Scales Combining Airborne Electromagnetism and Magnetism. *Geophysical Research Letters*, *48*(12). https://doi.org/10.1029/2020GL092000

Egan, P. A., & Price, M. F. (2017). Mountain ecosystem services and climate change: A global overview of potential threats and strategies for adaptation. *UNESCO Publishing*. https://unesdoc.unesco.org/ark:/48223/pf0000248768

Engdahl, N. B., & Maxwell, R. M. (2015). Quantifying changes in age distributions and the hydrologic balance of a high-mountain watershed from climate induced variations in recharge. *Journal of Hydrology*, *522*, 152–162. https://doi.org/10.1016/j.jhydrol.2014.12.032

Evans, J. P. (1990). Thickness-displacement relationships for fault zones. *Journal of Structural Geology*, *12*(8), 1061–1065. https://doi.org/10.1016/0191-8141(90)90101-4

Fan, L., Kuang, X., Or, D., & Zheng, C. (2023). Streamflow Composition and Water "Imbalance" in the Northern Himalayas. *Water Resources Research*, *59*(10), e2022WR034243. https://doi.org/10.1029/2022WR034243

Fan, Y. (2019). Are catchments leaky? *WIREs Water*, *6*(6). https://doi.org/10.1002/wat2.1386

Farr, T. G., Rosen, P. A., Caro, E., Crippen, R., Duren, R., Hensley, S., Kobrick, M., Paller, M., Rodriguez, E., Roth, L., Seal, D., Shaffer, S., Shimada, J., Umland, J., Werner, M., Oskin, M., Burbank, D., & Alsdorf, D. (2007). The Shuttle Radar Topography Mission. *Reviews of Geophysics*, *45*(2), 2005RG000183. https://doi.org/10.1029/2005RG000183

Faulkner, D. R., Jackson, C. A. L., Lunn, R. J., Schlische, R. W., Shipton, Z. K., Wibberley, C. A. J., & Withjack, M. O. (2010). A review of recent developments concerning the structure, mechanics and fluid flow properties of fault zones. *Journal of Structural Geology*, *32*(11), 1557–1575. https://doi.org/10.1016/j.jsg.2010.06.009

Feth, J. H. (1964). Hidden Recharge. *Groundwater*, *2*(4), 14–17. https://doi.org/10.1111/j.1745-6584.1964.tb01780.x

Fienen, M. N., Nolan, B. T., & Feinstein, D. T. (2016). Evaluating the sources of water to wells: Three techniques for metamodeling of a groundwater flow model. *Environmental Modelling & Software*, *77*, 95–107. https://doi.org/10.1016/j.envsoft.2015.11.023

Fienen, M. N., Nolan, B. T., Feinstein, D. T., & Starn, J. J. (2015). Metamodels to Bridge the Gap Between Modeling and Decision Support. *Groundwater*, *53*(4), 511–512. https://doi.org/10.1111/gwat.12339

Figueroa, R., Viguier, B., Taucare, M., Yáñez, G., Arancibia, G., Sanhueza, J., & Daniele, L. (2021). Deciphering groundwater flow-paths in fault-controlled semiarid mountain front zones (Central Chile). *Science of The Total Environment*, *771*, 145456. https://doi.org/10.1016/j.scitotenv.2021.145456

Fleckenstein, J. H., Krause, S., Hannah, D. M., & Boano, F. (2010). Groundwater-surface water interactions: New methods and models to improve understanding of processes and dynamics. *Advances in Water Resources*, *33*(11), 1291–1295. https://doi.org/10.1016/j.advwatres.2010.09.011

Fock, A. I. (2005). *Cronología y tectónica de la exhumación en el neógeno de Los Andes de Chile Central entre los 33° y los 34° S*. Tesis geólogo--Universidad de Chile.

Folch, A., & Mas-Pla, J. (2008). Hydrogeological interactions between fault zones and alluvial aquifers in regional flow systems. *Hydrological Processes*, *22*(17), 3476–3487. https://doi.org/10.1002/hyp.6956

Freeman, M. C., Pringle, C. M., & Jackson, C. R. (2007). Hydrologic connectivity and the contribution of stream headwaters to ecological integrity at regional scales. *Journal of the American Water Resources Association*, *43*(1), 5–14. https://doi.org/10.1111/j.1752-1688.2007.00002.x

Freeze, R. A., & Cherry, J. A. (1979). *Groundwater*. Prentice-Hall. https://books.google.cl/books?id=feVOAAAAMAAJ

Freeze, R. A., & Witherspoon, P. A. (1967). Theoretical analysis of regional groundwater flow: 2. Effect of water-table configuration and subsurface permeability variation. *Water Resources Research*, *3*(2), 623–634. https://doi.org/10.1029/WR003i002p00623

Fu, Y., Dong, Y., Wang, L., Bour, O., Klepikova, M. V., Zong, Z., Xu, Z., & Zhou, Z. (2022). Characteristics of hydraulic conductivity in mountain block systems and its effects on mountain block recharge: Insights from field investigation and numerical modeling. *Journal of Hydrology*, *612*, 128184. https://doi.org/10.1016/j.jhydrol.2022.128184

Gardner, P. M., Nelson, N. C., Heilweil, V. M., Solder, J. E., & Solomon, D. K. (2020). Rethinking a groundwater flow system using a multiple-tracer geochemical approach: A case study in Moab-Spanish Valley, Utah. *Journal of Hydrology*, *590*, 125512. https://doi.org/10.1016/j.jhydrol.2020.125512

Garreaud, R. (2009). The Andes climate and weather. *Advances in Geosciences*, *22*, 3–11. https://doi.org/10.5194/adgeo-22-3-2009

Garreaud, R., & Aceituno, P. (2001). Interannual rainfall variability over the South American Altiplano. *Journal of Climate*, *14*(12), 2779–2789.

Garreaud, R., Boisier, J. P., Rondanelli, R., Montecinos, A., Sepúlveda, H. H., & Veloso-Aguila, D. (2020). The Central Chile Mega Drought (2010–2018): A climate dynamics perspective. *International Journal of Climatology*, *40*(1), 421–439. https://doi.org/10.1002/joc.6219

Garreaud, R. D., Alvarez-Garreton, C., Barichivich, J., Boisier, J. P., Christie, D., Galleguillos, M., LeQuesne, C., McPhee, J., & Zambrano-Bigiarini, M. (2017). The 2010–2015 megadrought in central Chile: Impacts on regional hydroclimate and vegetation. *Hydrology and Earth System Sciences*, *21*(12), 6307–6327. https://doi.org/10.5194/hess-21-6307-2017

Garreaud, R., Vuille, M., & Clement, A. C. (2003). The climate of the Altiplano: Observed current conditions and mechanisms of past changes. *Palaeogeography, Palaeoclimatology, Palaeoecology*, *194*(1–3), 5–22. https://doi.org/10.1016/S0031-0182(03)00269-4

Gauvain, A., Leray, S., Marçais, J., Roques, C., Vautier, C., Gresselin, F., Aquilina, L., & Dreuzy, J. (2021). Geomorphological Controls on Groundwater Transit Times: A Synthetic Analysis at the Hillslope Scale. *Water Resources Research*, *57*(7). https://doi.org/10.1029/2020WR029463

Geyh, M. A. (2000). An Overview of 14C Analysis in the Study of Groundwater. *Radiocarbon*, *42*(1), 99–114. Cambridge Core. https://doi.org/10.1017/S0033822200053078

Ginn, T. R., Haeri, H., Massoudieh, A., & Foglia, L. (2009). Notes on Groundwater Age in Forward and Inverse Modeling. *Transport in Porous Media*, *79*(1), 117–134. https://doi.org/10.1007/s11242-009-9406-1

Glas, R., Lautz, L., McKenzie, J., Moucha, R., Chavez, D., Mark, B., & Lane, J. W.

(2019). Hydrogeology of an alpine talus aquifer: Cordillera Blanca, Peru. *Hydrogeology Journal*, *27*(6), 2137–2154. https://doi.org/10.1007/s10040-019-01982-5

Gleeson, T., & Manning, A. H. (2008). Regional groundwater flow in mountainous terrain: Three-dimensional simulations of topographic and hydrogeologic controls. *Water Resources Research*, *44*(10). https://doi.org/10.1029/2008WR006848

Gleeson, T., Marklund, L., Smith, L., & Manning, A. H. (2011). Classifying the water table at regional to continental scales. *Geophysical Research Letters*, *38*(5), n/a-n/a. https://doi.org/10.1029/2010GL046427

Gleeson, T., & Novakowski, K. (2009). Identifying watershed-scale barriers to groundwater flow: Lineaments in the Canadian Shield. *Geological Society of America Bulletin*, *121*(3–4), 333–347. https://doi.org/10.1130/B26241.1

Gleick, P. H. (1989). Climate change, hydrology, and water resources. *Reviews of Geophysics*, *27*(3), 329–344. https://doi.org/10.1029/RG027i003p00329

Goderniaux, P., Davy, P., Bresciani, E., de Dreuzy, J.-R., & Le Borgne, T. (2013). Partitioning a regional groundwater flow system into shallow local and deep regional flow compartments. *Water Resources Research*, *49*(4), 2274–2286. https://doi.org/10.1002/wrcr.20186

González, F. A., Maksymowicz, A., Díaz, D., Villegas, L., Leiva, M., Blanco, B., Vera, E., Contreras, S., Cabrera, D., & Bonvalot, S. (2018). Characterization of the depocenters and the basement structure, below the central Chile Andean Forearc: A 3D geophysical modelling in Santiago Basin area. *Basin Research*, *30*(4), 799–815. https://doi.org/10.1111/bre.12281

Gorelick, N., Hancher, M., Dixon, M., Ilyushchenko, S., Thau, D., & Moore, R. (2017). Google Earth Engine: Planetary-scale geospatial analysis for everyone. *Remote Sensing of Environment*, *202*, 18–27. https://doi.org/10.1016/j.rse.2017.06.031

Grêt-Regamey, A., Brunner, S. H., & Kienast, F. (2012). Mountain Ecosystem Services: Who Cares? *Mountain Research and Development*, *32*(S1), S23–S34. https://doi.org/10.1659/MRD-JOURNAL-D-10-00115.S1

Gu, Y., Brown, J. F., Verdin, J. P., & Wardlow, B. (2007). A five-year analysis of MODIS NDVI and NDWI for grassland drought assessment over the central Great Plains of the United States. *Geophysical Research Letters*, *34*(6), L06407. https://doi.org/10.1029/2006GL029127

Gu, Y., Hunt, E., Wardlow, B., Basara, J. B., Brown, J. F., & Verdin, J. P. (2008). Evaluation of MODIS NDVI and NDWI for vegetation drought monitoring using Oklahoma Mesonet soil moisture data. *Geophysical Research Letters*, *35*(22), L22401. https://doi.org/10.1029/2008GL035772

Haitjema, H. M., & Mitchell-Bruker, S. (2005). Are Water Tables a Subdued Replica of the Topography? *Groundwater*, *43*(6), 781–786. https://doi.org/10.1111/j.1745-6584.2005.00090.x

Haneberg, W. C. (1995). Steady State Groundwater Flow Across Idealized Faults. *Water Resources Research*, *31*(7), 1815–1820. https://doi.org/10.1029/95WR01178

Harbaugh, A. W. (2005). *MODFLOW-2005: The U.S. Geological Survey modular*

ground-water model—The ground-water flow process (Report 6-A16; Techniques and Methods). USGS Publications Warehouse. https://doi.org/10.3133/tm6A16

Hartley, A. J., & Evenstar, L. (2010). Cenozoic stratigraphic development in the north Chilean forearc: Implications for basin development and uplift history of the Central Andean margin. *Tectonophysics*, *495*(1–2), 67–77. https://doi.org/10.1016/j.tecto.2009.05.013

Hayashi, M. (2020). Alpine Hydrogeology: The Critical Role of Groundwater in Sourcing the Headwaters of the World. *Groundwater*, *58*(4), 498–510. https://doi.org/10.1111/gwat.12965

Healy, R. W. (Ed.). (2010). Groundwater recharge. In *Estimating Groundwater Recharge* (pp. 1–14). Cambridge University Press; Cambridge Core. https://doi.org/10.1017/CBO9780511780745.002

Hilberg, S. (2016). Review: Natural tracers in fractured hard-rock aquifers in the Austrian part of the Eastern Alps—previous approaches and future perspectives for hydrogeology in mountain regions. *Hydrogeology Journal*, *24*(5), 1091–1105. https://doi.org/10.1007/s10040-016-1395-x

Hill, M. C., & Tiedeman, C. R. (2007). *Effective groundwater model calibration: With analysis of data, sensitivities, predictions, and uncertainty*. Wiley; USGS Publications Warehouse. https://doi.org/10.1002/9780470041086.index

Hobouchian, M. P., Salio, P., García Skabar, Y., Vila, D., & Garreaud, R. (2017). Assessment of satellite precipitation estimates over the slopes of the subtropical Andes. *Atmospheric Research*, *190*, 43–54. https://doi.org/10.1016/j.atmosres.2017.02.006

Hood, J. L., & Hayashi, M. (2015). Characterization of snowmelt flux and groundwater storage in an alpine headwater basin. *Journal of Hydrology*, *521*, 482–497. https://doi.org/10.1016/j.jhydrol.2014.12.041

Houston, J. (2006). Variability of precipitation in the Atacama Desert: Its causes and hydrological impact. *International Journal of Climatology: A Journal of the Royal Meteorological Society*, *26*(15), 2181–2198.

Hsu, S.-M., Ke, C.-C., Dong, M.-C., & Lin, Y.-T. (2022). Investigating fault zone hydraulic properties and groundwater potential in a fault-dominated aquifer system: A case study of the Dili fault in Central Taiwan. *Engineering Geology*, *308*, 106805. https://doi.org/10.1016/j.enggeo.2022.106805

Hu, A., Wang, J., Sun, H., Niu, B., Si, G., Wang, J., Yeh, C.-F., Zhu, X., Lu, X., Zhou, J., Yang, Y., Ren, M., Hu, Y., Dong, H., & Zhang, G. (2020). Mountain biodiversity and ecosystem functions: Interplay between geology and contemporary environments. *The ISME Journal*, *14*(4), 931–944. https://doi.org/10.1038/s41396-019-0574-x

Huss, M., Bookhagen, B., Huggel, C., Jacobsen, D., Bradley, R. S., Clague, J. J., Vuille, M., Buytaert, W., Cayan, D. R., Greenwood, G., Mark, B. G., Milner, A. M., Weingartner, R., & Winder, M. (2017). Toward mountains without permanent snow and ice. *Earths Future*, *5*(5), 418–435. https://doi.org/10.1002/2016EF000514

Hussien, H. M., Kehew, A. E., Aggour, T., Korany, E., Abotalib, A. Z., Hassanein, A., & Morsy, S. (2017). An integrated approach for identification of potential aquifer zones

in structurally controlled terrain: Wadi Qena basin, Egypt. *Catena*, *149*, 73–85. https://doi.org/10.1016/j.catena.2016.08.032

Immerzeel, W. W., Lutz, A. F., Andrade, M., Bahl, A., Biemans, H., Bolch, T., Hyde, S., Brumby, S., Davies, B. J., Elmore, A. C., Emmer, A., Feng, M., Fernández, A., Haritashya, U., Kargel, J. S., Koppes, M., Kraaijenbrink, P. D. A., Kulkarni, A. V., Mayewski, P. A., … Baillie, J. E. M. (2020). Importance and vulnerability of the world's water towers. *Nature*, *577*(7790), 364–369. https://doi.org/10.1038/s41586-019-1822-y

Izbicki, J. A., Teague, N. F., Hatzinger, P. B., Böhlke, J. K., & Sturchio, N. C. (2015). Groundwater movement, recharge, and perchlorate occurrence in a faulted alluvial aquifer in California (USA). *Hydrogeology Journal*, *23*(3), 467–491. https://doi.org/10.1007/s10040-014-1217-y

Jamieson, G. R., & Freeze, R. A. (1982). Determining Hydraulic Conductivity Distributions in a Mountainous Area Using Mathematical Modeling. *Ground Water*, *20*(2), 168–177. https://doi.org/10.1111/j.1745-6584.1982.tb02745.x

Jasechko, S., Kirchner, J. W., Welker, J. M., & McDonnell, J. J. (2016). Substantial proportion of global streamflow less than three months old. *Nature Geoscience*, *9*(2), 126–129. https://doi.org/10.1038/ngeo2636

Jasiewicz, J., & Stepinski, T. F. (2013). Geomorphons—A pattern recognition approach to classification and mapping of landforms. *Geomorphology*, *182*, 147–156. https://doi.org/10.1016/j.geomorph.2012.11.005

Jordan, T. E., Isacks, B. L., Allmendinger, R. W., Brewer, J. A., Ramos, V. A., & Ando, C. J. (1983). Andean tectonics related to geometry of subducted Nazca plate. *Geological Society of America Bulletin*, *94*(3), 341. https://doi.org/10.1130/0016-7606(1983)94<341:ATRTGO>2.0.CO;2

Jordan, T. E., Kirk-Lawlor, N. E., Blanco, N. P., Rech, J. A., & Cosentino, N. J. (2014). Landscape modification in response to repeated onset of hyperarid paleoclimate states since 14 Ma, Atacama Desert, Chile. *Geological Society of America Bulletin*, *126*(7–8), 1016–1046. https://doi.org/10.1130/B30978.1

Jung, Y.-Y., Koh, D.-C., Shin, W.-J., Kwon, H.-I., Oh, Y.-H., & Lee, K.-S. (2021). Assessing seasonal variations in water sources of streamflow in a temperate mesoscale catchment with granitic bedrocks using hydrochemistry and stable isotopes. *Journal of Hydrology: Regional Studies*, *38*, 100940. https://doi.org/10.1016/j.ejrh.2021.100940

Kamenik, C., Schmidt, R., Kum, G., & Psenner, R. (2001). The influence of catchment characteristics on the water chemistry of mountain lakes. *Arctic Antarctic and Alpine Research*, *33*(4), 404–409. https://doi.org/10.2307/1552549

Kaminsky, A. (2010). ZondRes2D. *Software for Two-Dimensional Interpretation of DC Resistivity and IP Data. Zond Geophysical Software, Saint-Petersburg (Russia)*.

Katsoulas, N., Elvanidi, A., Ferentinos, K. P., Kacira, M., Bartzanas, T., & Kittas, C. (2016). Crop reflectance monitoring as a tool for water stress detection in greenhouses: A review. *Biosystems Engineering*, *151*, 374–398. https://doi.org/10.1016/j.biosystemseng.2016.10.003

Keegan-Treloar, R., Irvine, D. J., Solórzano-Rivas, S. C., Werner, A. D., Banks, E. W.,

& Currell, M. J. (2022). Fault-controlled springs: A review. *Earth-Science Reviews*, *230*, 104058. https://doi.org/10.1016/j.earscirev.2022.104058

Kløve, B., Ala-aho, P., Bertrand, G., Boukalova, Z., Ertürk, A., Goldscheider, N., Ilmonen, J., Karakaya, N., Kupfersberger, H., Kvœrner, J., Lundberg, A., Mileusnić, M., Moszczynska, A., Muotka, T., Preda, E., Rossi, P., Siergieiev, D., Šimek, J., Wachniew, P., … Widerlund, A. (2011). Groundwater dependent ecosystems. Part I: Hydroecological status and trends. *Environmental Science & Policy*, *14*(7), 770–781. https://doi.org/10.1016/j.envsci.2011.04.002

Kløve, B., Ala-Aho, P., Bertrand, G., Gurdak, J. J., Kupfersberger, H., Kværner, J., Muotka, T., Mykrä, H., Preda, E., Rossi, P., Uvo, C. B., Velasco, E., & Pulido-Velazquez, M. (2014). Climate change impacts on groundwater and dependent ecosystems. *Journal of Hydrology*, *518*, 250–266. https://doi.org/10.1016/j.jhydrol.2013.06.037

Kolbe, T., Marçais, J., Thomas, Z., Abbott, B. W., De Dreuzy, J.-R., Rousseau-Gueutin, P., Aquilina, L., Labasque, T., & Pinay, G. (2016). Coupling 3D groundwater modeling with CFC-based age dating to classify local groundwater circulation in an unconfined crystalline aquifer. *Journal of Hydrology*, *543*, 31–46. https://doi.org/10.1016/j.jhydrol.2016.05.020

Konapala, G., Mishra, A. K., Wada, Y., & Mann, M. E. (2020). Climate change will affect global water availability through compounding changes in seasonal precipitation and evaporation. *Nature Communications*, *11*(1), 3044. https://doi.org/10.1038/s41467-020-16757-w

Kreamer, D. K., Ball, D. M., Re, V., Simmons, C. T., Bothwell, T., Verweij, H. J. M., Mukherjee, A., & Moreau, M. F. (2021). The future of groundwater science and research. In *Global Groundwater* (pp. 503–517). Elsevier. https://doi.org/10.1016/B978-0-12-818172-0.00037-2

Kresic, N. (2006). *Hydrogeology and Groundwater Modeling* (0 ed.). CRC Press. https://doi.org/10.1201/9781420004991

Kummu, M., Guillaume, J. H. A., de Moel, H., Eisner, S., Flörke, M., Porkka, M., Siebert, S., Veldkamp, T. I. E., & Ward, P. J. (2016). The world's road to water scarcity: Shortage and stress in the 20th century and pathways towards sustainability. *Scientific Reports*, *6*(1), 38495. https://doi.org/10.1038/srep38495

Langevin, C. D., Hughes, J. D., Banta, E. R., Niswonger, R. G., Panday, S., & Provost, A. M. (2017). *Documentation for the MODFLOW 6 Groundwater Flow Model* (Report 6-A55; Techniques and Methods). USGS Publications Warehouse. https://doi.org/10.3133/tm6A55

Lehner, B., & Grill, G. (2013). Global river hydrography and network routing: Baseline data and new approaches to study the world's large river systems. *Hydrological Processes*, *27*(15), 2171–2186. https://doi.org/10.1002/hyp.9740

Leibowitz, S. G., Wigington, P. J., Schofield, K. A., Alexander, L. C., Vanderhoof, M. K., & Golden, H. E. (2018). Connectivity of Streams and Wetlands to Downstream Waters: An Integrated Systems Framework. *JAWRA Journal of the American Water Resources Association*, *54*(2), 298–322. https://doi.org/10.1111/1752-1688.12631

Leray, S., de Dreuzy, J.-R., Bour, O., & Bresciani, E. (2013). Numerical modeling of the productivity of vertical to shallowly dipping fractured zones in crystalline rocks. *Journal of Hydrology*, *481*, 64–75. https://doi.org/10.1016/j.jhydrol.2012.12.014

Leray, S., de Dreuzy, J.-R., Bour, O., Labasque, T., & Aquilina, L. (2012). Contribution of age data to the characterization of complex aquifers. *Journal of Hydrology*, *464–465*, 54–68. https://doi.org/10.1016/j.jhydrol.2012.06.052

Linde, N., Renard, P., Mukerji, T., & Caers, J. (2015). Geological realism in hydrogeological and geophysical inverse modeling: A review. *Advances in Water Resources*, *86*, 86–101. https://doi.org/10.1016/j.advwatres.2015.09.019

Lindsay, J. B. (2016). Whitebox GAT: A case study in geomorphometric analysis. *Computers & Geosciences*, *95*, 75–84. https://doi.org/10.1016/j.cageo.2016.07.003

Loke, M. H. (2004). *Tutorial: 2-D and 3-D electrical imaging surveys*. www.geoelectrical.com

Longuevergne, L., Scanlon, B. R., & Wilson, C. R. (2010). GRACE Hydrological estimates for small basins: Evaluating processing approaches on the High Plains Aquifer, USA. *Water Resources Research*, *46*(11). https://doi.org/10.1029/2009WR008564

Loosli, H. H., & Oeschger, H. (1980). Use of 39Ar and 14C for Groundwater Dating. *Radiocarbon*, *22*(3), 863–870. Cambridge Core. https://doi.org/10.1017/S0033822200010250

Lopez Loera, H., Ramos Leal, J. A., Davila Harris, P., Torres Gaytan, D. E., Martinez Ruiz, V. J., & Gogichaishvili, A. (2015). Geophysical Exploration of Fractured-Media Aquifers at the Mexican Mesa Central: Satellite City, San Luis Potosi, Mexico. *Surveys in Geophysics*, *36*(1), 167–184. https://doi.org/10.1007/s10712-014-9302-2

Lu, D., Huang, D., & Xu, C. (2021). Estimation of hydraulic conductivity by using pumping test data and electrical resistivity data in faults zone. *Ecological Indicators*, *129*, 107861. https://doi.org/10.1016/j.ecolind.2021.107861

Ma, B., Jin, M., Liang, X., & Li, J. (2018). Groundwater mixing and mineralization processes in a mountain–oasis–desert basin, northwest China: Hydrogeochemistry and environmental tracer indicators. *Hydrogeology Journal*, *26*(1), 233–250. https://doi.org/10.1007/s10040-017-1659-0

Mace, E., Aalseth, C., Brandenberger, J., Day, A., Hoppe, E., Humble, P., Keillor, M., Kulongoski, J., Overman, C., Panisko, M., Seifert, A., White, S., Wilcox Freeburg, E., & Williams, R. (2017). Methods for using argon-39 to age-date groundwater using ultra-low-background proportional counting. *Applied Radiation and Isotopes*, *126*, 9–12. https://doi.org/10.1016/j.apradiso.2016.12.037

Manning, A. H., Ball, L. B., Wanty, R. B., & Williams, K. H. (2021). Direct Observation of the Depth of Active Groundwater Circulation in an Alpine Watershed. *Water Resources Research*, *57*(2), 2020WR028548. https://doi.org/10.1029/2020WR028548

Manning, A. H., & Solomon, D. K. (2005). An integrated environmental tracer approach to characterizing groundwater circulation in a mountain block. *Water Resources Research*, *41*(12), 2005WR004178. https://doi.org/10.1029/2005WR004178

Marçais, J., De Dreuzy, J.-R., & Erhel, J. (2017). Dynamic coupling of subsurface and

seepage flows solved within a regularized partition formulation. *Advances in Water Resources*, *109*, 94–105. https://doi.org/10.1016/j.advwatres.2017.09.008

Markovich, K. H., Condon, L. E., Carroll, K. C., Purtschert, R., & McIntosh, J. C. (2021). A Mountain-Front Recharge Component Characterization Approach Combining Groundwater Age Distributions, Noble Gas Thermometry, and Fluid and Energy Transport Modeling. *Water Resources Research*, *57*(1). https://doi.org/10.1029/2020WR027743

Markovich, K. H., Manning, A. H., Condon, L. E., & McIntosh, J. C. (2019). Mountain-Block Recharge: A Review of Current Understanding. *Water Resources Research*, *55*(11), 8278–8304. https://doi.org/10.1029/2019WR025676

Marti, E., Leray, S., & Roques, C. (2023). *Dataset used in "From lowlands to mountain peaks: Impacts of landforms on the desaturation of groundwater-dependent wetlands"* [dataset]. Zenodo. https://doi.org/10.5281/ZENODO.10144981

Marti, E., Leray, S., Villela, D., Maringue, J., Yáñez, G., Salazar, E., Poblete, F., Jimenez, J., Reyes, G., Poblete, G., Huamán, Z., Figueroa, R., Araya Vargas, J., Sanhueza, J., Muñoz, M., Charrier, R., & Fernández, G. (2023). Unravelling geological controls on groundwater flow and surface water-groundwater interaction in mountain systems: A multi-disciplinary approach. *Journal of Hydrology*, *623*, 129786. https://doi.org/10.1016/j.jhydrol.2023.129786

Martos-Rosillo, S., Ruiz-Constán, A., González-Ramón, A., Mediavilla, R., Martín-Civantos, J. M., Martínez-Moreno, F. J., Jódar, J., Marín-Lechado, C., Medialdea, A., Galindo-Zaldívar, J., Pedrera, A., & Durán, J. J. (2019). The oldest managed aquifer recharge system in Europe: New insights from the Espino recharge channel (Sierra Nevada, southern Spain). *Journal of Hydrology*, *578*, 124047. https://doi.org/10.1016/j.jhydrol.2019.124047

McClymont, A. F., Hayashi, M., Bentley, L. R., Muir, D., & Ernst, E. (2010). Groundwater flow and storage within an alpine meadow-talus complex. *Hydrology and Earth System Sciences*, *14*(6), 859–872. https://doi.org/10.5194/hess-14-859-2010

McClymont, A. F., Roy, J. W., Hayashi, M., Bentley, L. R., Maurer, H., & Langston, G. (2011). Investigating groundwater flow paths within proglacial moraine using multiple geophysical methods. *Journal of Hydrology*, *399*(1–2), 57–69. https://doi.org/10.1016/j.jhydrol.2010.12.036

McCord, J. T., Gotway, C. A., & Conrad, S. H. (1997). Impact of geologic heterogeneity on recharge estimation using environmental tracers: Numerical modeling investigation. *Water Resources Research*, *33*(6), 1229–1240. https://doi.org/10.1029/96WR03755

McDonnell, J. J. (2003). Where does water go when it rains? Moving beyond the variable source area concept of rainfall-runoff response. *Hydrological Processes*, *17*(9), 1869–1875. https://doi.org/10.1002/hyp.5132

Meyer, J. L., Strayer, D. L., Wallace, J. B., Eggert, S. L., Helfman, G. S., & Leonard, N. E. (2007). The contribution of headwater streams to biodiversity in river networks. *Journal of the American Water Resources Association*, *43*(1), 86–103. https://doi.org/10.1111/j.1752-1688.2007.00008.x

Montecinos, A., & Aceituno, P. (2003). Seasonality of the ENSO-Related Rainfall Variability in Central Chile and Associated Circulation Anomalies. *Journal of Climate*, *16*(2), 281–296. https://doi.org/10.1175/1520-0442(2003)016<0281:SOTERR>2.0.CO;2

Moore, C., & Doherty, J. (2006). The cost of uniqueness in groundwater model calibration. *Advances in Water Resources*, *29*(4), 605–623. https://doi.org/10.1016/j.advwatres.2005.07.003

Muñoz, M., & Hamza, V. (1993). Heat flow and temperature gradients in Chile. *Studia Geophysica et Geodaetica*, *37*(3), 315–348. https://doi.org/10.1007/BF01624604

Murty, B. V. S., & Raghavan, V. K. (2002). The gravity method in groundwater exploration in crystalline rocks: A study in the peninsular granitic region of Hyderabad, India. *Hydrogeology Journal*, *10*(2), 307–321. https://doi.org/10.1007/s10040-001-0184-2

Nester, P., & Jordan, T. (2011). The Pampa del Tamarugal Forearc Basin in Northern Chile: The Interaction of Tectonics and Climate. In C. Busby & A. Azor (Eds.), *Tectonics of Sedimentary Basins* (1st ed., pp. 369–381). Wiley. https://doi.org/10.1002/9781444347166.ch18

Nicolas, M., Bour, O., Selles, A., Dewandel, B., Bailly-Comte, V., Chandra, S., Ahmed, S., & Maréchal, J.-C. (2019). Managed Aquifer Recharge in fractured crystalline rock aquifers: Impact of horizontal preferential flow on recharge dynamics. *Journal of Hydrology*, *573*, 717–732. https://doi.org/10.1016/j.jhydrol.2019.04.003

Niemeyer, H. (2002). *Historia natural de la Reserva Nacional Río Clarillo: Un espacio para aprender ecología*. s.n.

Niswonger, R. G., Panday, S., & Ibaraki, M. (2011). *MODFLOW-NWT, a Newton formulation for MODFLOW-2005* (Report 6-A37; Techniques and Methods). USGS Publications Warehouse. https://doi.org/10.3133/tm6A37

Oster, H., Sonntag, C., & Münnich, K. O. (1996). Groundwater age dating with chlorofluorocarbons. *Water Resources Research*, *32*(10), 2989–3001. https://doi.org/10.1029/96WR01775

Oyarzún, R., Jofré, E., Morales, P., Maturana, H., Oyarzún, J., Kretschmer, N., Aguirre, E., Gallardo, P., Toro, L. E., Muñoz, J. F., & Aravena, R. (2015). A hydrogeochemistry and isotopic approach for the assessment of surface water–groundwater dynamics in an arid basin: The Limarí watershed, North-Central Chile. *Environmental Earth Sciences*, *73*(1), 39–55. https://doi.org/10.1007/s12665-014-3393-4

Pan, S., Wang, Z., Su, Q., Sun, T., & Zhang, Y. (2008). Groundwater level monitoring model using multi-temporal images in arid region of northwest China. *The International Archives of the Photogrammetry, Remote Sensing and Spatial Information Sciences*, *37*, 745–750.

Pérez, A., Ruiz, J. A., Vargas, G., Rauld, R., Rebolledo, S., & Campos, J. (2014). Improving seismotectonics and seismic hazard assessment along the San Ramón Fault at the eastern border of Santiago city, Chile. *Natural Hazards*, *71*(1), 243–274. https://doi.org/10.1007/s11069-013-0908-3

Pérez-Estay, N., Molina-Piernas, E., Roquer, T., Aravena, D., Araya Vargas, J., Morata, D., Arancibia, G., Valdenegro, P., García, K., & Elizalde, D. (2022). Shallow anatomy of hydrothermal systems controlled by the Liquiñe-Ofqui Fault System and the Andean Transverse Faults: Geophysical imaging of fluid pathways and practical implications for geothermal exploration. *Geothermics*, *104*, 102435. https://doi.org/10.1016/j.geothermics.2022.102435

Pincetti-Zúniga, G. P., Richards, L. A., Daniele, L., Boyce, A. J., & Polya, D. A. (2022). Hydrochemical characterization, spatial distribution, and geochemical controls on arsenic and boron in waters from arid Arica and Parinacota, northern Chile. *Science of The Total Environment*, *806*, 150206. https://doi.org/10.1016/j.scitotenv.2021.150206

Ping, J., Zhu, Y., Mei, X., Leng, W., Li, S., & Zhao, J. (2021). Estimation of mountain block recharge on the northern Tianshan Mountains using numerical modeling. *Journal of Mountain Science*, *18*(7), 1794–1810. https://doi.org/10.1007/s11629-020-6589-y

Piquer, J., Hollings, P., Rivera, O., Cooke, D. R., Baker, M., & Testa, F. (2017). Along-strike segmentation of the Abanico Basin, central Chile: New chronological, geochemical and structural constraints. *Lithos*, *268–271*, 174–197. https://doi.org/10.1016/j.lithos.2016.10.025

Piquer, J., Rivera, O., Yáñez, G., & Oyarzun, N. (2021). The Piuquencillo fault system: A long-lived, Andean-transverse fault system and its relationship with magmatic and hydrothermal activity. *Solid Earth*, *12*(1), 253–273. https://doi.org/10.5194/se-12-253-2021

Pokhrel, Y., Felfelani, F., Satoh, Y., Boulange, J., Burek, P., Gädeke, A., Gerten, D., Gosling, S. N., Grillakis, M., Gudmundsson, L., Hanasaki, N., Kim, H., Koutroulis, A., Liu, J., Papadimitriou, L., Schewe, J., Müller Schmied, H., Stacke, T., Telteu, C.-E., … Wada, Y. (2021). Global terrestrial water storage and drought severity under climate change. *Nature Climate Change*, *11*(3), 226–233. https://doi.org/10.1038/s41558-020-00972-w

Pollock, D. W. (2016). *User guide for MODPATH Version 7—A particle-tracking model for MODFLOW* (Report 2016–1086; Open-File Report, p. 41). USGS Publications Warehouse. https://doi.org/10.3133/ofr20161086

Rajabpour, H., Vaezihir, A., & Sedghi, M. H. (2016). The North Tabriz Fault, a barrier to groundwater flow in an alluvial aquifer northwest of Tabriz, Iran. *Environmental Earth Sciences*, *75*(10), 849. https://doi.org/10.1007/s12665-016-5663-9

Rapp, G. A., Condon, L. E., & Markovich, K. H. (2020). Sensitivity of Simulated Mountain Block Hydrology to Subsurface Conceptualization. *Water Resources Research*, *56*(10). https://doi.org/10.1029/2020WR027714

Rauld, R. A. (2002). *Análisis morfoestructural del frente cordillerano Santiago Oriente entre el río Mapocho y la Quebrada de Macul*. Tesis geólogo--Universidad de Chile.

Reeves, C. (2005). *Aeromagnetic Surveys: Principles, Practice and Interpretation*. Geosoft. http://www.geosoft.com/knowledge

Reutter, K.-J., Scheuber, E., & Chong, G. (1996). The Precordilleran fault system of Chuquicamata, Northern Chile: Evidence for reversals along arc-parallel strike-slip

faults. *Tectonophysics*, *259*(1–3), 213–228. https://doi.org/10.1016/0040-1951(95)00109-3

Robert, T., Dassargues, A., Brouyere, S., Kaufmann, O., Hallet, V., & Nguyen, F. (2011). Assessing the contribution of electrical resistivity tomography (ERT) and self-potential (SP) methods for a water well drilling program in fractured/karstified limestones. *Journal of Applied Geophysics*, *75*(1), 42–53. https://doi.org/10.1016/j.jappgeo.2011.06.008

Robinson, D. A., Binley, A., Crook, N., Day-Lewis, F. D., Ferré, T. P. A., Grauch, V. J. S., Knight, R., Knoll, M., Lakshmi, V., Miller, R., Nyquist, J., Pellerin, L., Singha, K., & Slater, L. (2008). Advancing process-based watershed hydrological research using near-surface geophysics: A vision for, and review of, electrical and magnetic geophysical methods. *Hydrological Processes*, *22*(18), 3604–3635. https://doi.org/10.1002/hyp.6963

Roques, C., Bour, O., Aquilina, L., Dewandel, B., Leray, S., Schroetter, Jm., Longuevergne, L., Le Borgne, T., Hochreutener, R., Labasque, T., Lavenant, N., Vergnaud-Ayraud, V., & Mougin, B. (2014). Hydrological behavior of a deep sub-vertical fault in crystalline basement and relationships with surrounding reservoirs. *Journal of Hydrology*, *509*, 42–54. https://doi.org/10.1016/j.jhydrol.2013.11.023

Roques, C., Rupp, D. E., De Dreuzy, J.-R., Longuevergne, L., Jachens, E. R., Grant, G., Aquilina, L., & Selker, J. S. (2022). Recession discharge from compartmentalized bedrock hillslopes. *Hydrology and Earth System Sciences*, *26*(16), 4391–4405. https://doi.org/10.5194/hess-26-4391-2022

Ruelleu, S., Moreau, F., Bour, O., Gapais, D., & Martelet, G. (2010). Impact of gently dipping discontinuities on basement aquifer recharge: An example from Ploemeur (Brittany, France). *Journal of Applied Geophysics*, *70*(2), 161–168. https://doi.org/10.1016/j.jappgeo.2009.12.007

Ruiz Pereira, S., Díez, B., Cifuentes-Anticevic, J., Leray, S., Fernandoy, F., Marquardt, C., & Lambert, F. (2023). Hydrological connections in a glaciated Andean catchment under permafrost conditions (33°S). *Journal of Hydrology: Regional Studies*, *45*, 101311. https://doi.org/10.1016/j.ejrh.2022.101311

Samouelian, A., Cousin, I., Tabbagh, A., Bruand, A., & Richard, G. (2005). Electrical resistivity survey in soil science: A review. *Soil & Tillage Research*, *83*(2), 173–193. https://doi.org/10.1016/j.still.2004.10.004

Sanford, W. (2002). Recharge and groundwater models: An overview. *Hydrogeology Journal*, *10*(1), 110–120.

Sanhueza, J., Yáñez, G., Barra, F., Maringue, J., Figueroa, R., & Saez, E. (2022). Rheological, petrophysical and geometrical constraints of a subduction channel from a numerical model perspective: Insights from La Cabana Paleozoic peridotites, Coastal Cordillera of south-central Chile. *Journal of South American Earth Sciences*, *114*, 103706. https://doi.org/10.1016/j.jsames.2021.103706

Santibáñez, I., Cembrano, J., García-Pérez, T., Costa, C., Yáñez, G., Marquardt, C., Arancibia, G., & González, G. (2018). Crustal faults in the Chilean Andes: Geological constraints and seismic potential. *Andean Geology*, *46*(1), 32. https://doi.org/10.5027/andgeoV46n1-3067

Scanlon, B. R., Fakhreddine, S., Rateb, A., De Graaf, I., Famiglietti, J., Gleeson, T., Grafton, R. Q., Jobbagy, E., Kebede, S., Kolusu, S. R., Konikow, L. F., Long, D., Mekonnen, M., Schmied, H. M., Mukherjee, A., MacDonald, A., Reedy, R. C., Shamsudduha, M., Simmons, C. T., … Zheng, C. (2023). Global water resources and the role of groundwater in a resilient water future. *Nature Reviews Earth & Environment*, *4*(2), 87–101. https://doi.org/10.1038/s43017-022-00378-6

Scanlon, B. R., Keese, K. E., Flint, A. L., Flint, L. E., Gaye, C. B., Edmunds, W. M., & Simmers, I. (2006). Global synthesis of groundwater recharge in semiarid and arid regions. *Hydrological Processes: An International Journal*, *20*(15), 3335–3370.

Schaaf, C., & Wang, Z. (2015). *MCD43A4 MODIS/Terra+Aqua BRDF/Albedo Nadir BRDF Adjusted Ref Daily L3 Global—500m V006* [dataset]. NASA EOSDIS Land Processes DAAC. https://doi.org/10.5067/MODIS/MCD43A4.006

Schaller, M. F., & Fan, Y. (2009). River basins as groundwater exporters and importers: Implications for water cycle and climate modeling. *Journal of Geophysical Research: Atmospheres*, *114*(D4), 2008JD010636. https://doi.org/10.1029/2008JD010636

Schilling, O. S., Cook, P. G., Grierson, P. F., Dogramaci, S., & Simmons, C. T. (2021). Controls on Interactions Between Surface Water, Groundwater, and Riverine Vegetation Along Intermittent Rivers and Ephemeral Streams in Arid Regions. *Water Resources Research*, *57*(2), e2020WR028429. https://doi.org/10.1029/2020WR028429

Scibek, J., Allen, D. M., Cannon, A. J., & Whitfield, P. H. (2007). Groundwater–surface water interaction under scenarios of climate change using a high-resolution transient groundwater model. *Journal of Hydrology*, *333*(2–4), 165–181. https://doi.org/10.1016/j.jhydrol.2006.08.005

Scibek, J., Gleeson, T., & McKenzie, J. M. (2016). The biases and trends in fault zone hydrogeology conceptual models: Global compilation and categorical data analysis. *Geofluids*, *16*(4), 782–798. https://doi.org/10.1111/gfl.12188

Scott, C. A., Zhang, F., Mukherji, A., Immerzeel, W., Mustafa, D., & Bharati, L. (2019). Water in the Hindu Kush Himalaya. In P. Wester, A. Mishra, A. Mukherji, & A. B. Shrestha (Eds.), *The Hindu Kush Himalaya Assessment* (pp. 257–299). Springer International Publishing. https://doi.org/10.1007/978-3-319-92288-1_8

Seeyan, S., Merkel, B., & Abo, R. (2014). Investigation of the Relationship between Groundwater Level Fluctuation and Vegetation Cover by using NDVI for Shaqlawa Basin, Kurdistan Region – Iraq. *Journal of Geography and Geology*, *6*(3), p187. https://doi.org/10.5539/jgg.v6n3p187

Seibert, J., & McDonnell, J. J. (2015). Gauging the Ungauged Basin: Relative Value of Soft and Hard Data. *Journal of Hydrologic Engineering*, *20*(1), A4014004. https://doi.org/10.1061/(ASCE)HE.1943-5584.0000861

Siegfried, T., Bernauer, T., Guiennet, R., Sellars, S., Robertson, A. W., Mankin, J., Bauer-Gottwein, P., & Yakovlev, A. (2012). Will climate change exacerbate water stress in Central Asia? *Climatic Change*, *112*(3–4), 881–899. https://doi.org/10.1007/s10584-011-0253-z

Somers, L. D., Gordon, R. P., McKenzie, J. M., Lautz, L. K., Wigmore, O., Glose, A.,

Glas, R., Aubry-Wake, C., Mark, B., Baraer, M., & Condom, T. (2016). Quantifying groundwater–surface water interactions in a proglacial valley, Cordillera Blanca, Peru. *Hydrological Processes*, *30*(17), 2915–2929. https://doi.org/10.1002/hyp.10912

Somers, L. D., & McKenzie, J. M. (2020). A review of groundwater in high mountain environments. *WIREs Water*, *7*(6), e1475. https://doi.org/10.1002/wat2.1475

Sophocleous, M. (2002). Interactions between groundwater and surface water: The state of the science. *Hydrogeology Journal*, *10*(1), 52–67. https://doi.org/10.1007/s10040-001-0170-8

Soulsby, C., Tetzlaff, D., Van Den Bedem, N., Malcolm, I. A., Bacon, P. J., & Youngson, A. F. (2007). Inferring groundwater influences on surface water in montane catchments from hydrochemical surveys of springs and streamwaters. *Journal of Hydrology*, *333*(2–4), 199–213. https://doi.org/10.1016/j.jhydrol.2006.08.016

Starn, J. J., & Belitz, K. (2018). Regionalization of Groundwater Residence Time Using Metamodeling. *Water Resources Research*, *54*(9), 6357–6373. https://doi.org/10.1029/2017WR021531

Suárez, F., Leray, S., & Sanzana, P. (2021). Groundwater Resources. In B. Fernández & J. Gironás (Eds.), *Water Resources of Chile* (Vol. 8, pp. 93–127). Springer International Publishing. https://doi.org/10.1007/978-3-030-56901-3_5

Tabari, H. (2020). Climate change impact on flood and extreme precipitation increases with water availability. *Scientific Reports*, *10*(1), 13768. https://doi.org/10.1038/s41598-020-70816-2

Taucare, M., Daniele, L., Viguier, B., Vallejos, A., & Arancibia, G. (2020). Groundwater resources and recharge processes in the Western Andean Front of Central Chile. *Science of The Total Environment*, *722*, 137824. https://doi.org/10.1016/j.scitotenv.2020.137824

Taucare, M., Viguier, B., Figueroa, R., & Daniele, L. (2024). The alarming state of Central Chile's groundwater resources: A paradigmatic case of a lasting overexploitation. *Science of The Total Environment*, *906*, 167723. https://doi.org/10.1016/j.scitotenv.2023.167723

Taylor, R. G., Scanlon, B., Döll, P., Rodell, M., van Beek, R., Wada, Y., Longuevergne, L., Leblanc, M., Famiglietti, J. S., Edmunds, M., Konikow, L., Green, T. R., Chen, J., Taniguchi, M., Bierkens, M. F. P., MacDonald, A., Fan, Y., Maxwell, R. M., Yechieli, Y., … Treidel, H. (2013). Ground water and climate change. *Nature Climate Change*, *3*(4), 322–329. https://doi.org/10.1038/nclimate1744

Telford, W. M., Geldart, L. P., & Sheriff, R. E. (1990). *Applied Geophysics* (2nd ed.). Cambridge University Press. https://doi.org/10.1017/CBO9781139167932

Thiele, R. (1980). *Hoja Santiago: Región metropolitana: Carta geológica de Chile escala 1: 250.000*. Instituto de Investigaciones Geológicas.

Thornton, J. M., Therrien, R., Mariéthoz, G., Linde, N., & Brunner, P. (2022). Simulating Fully-Integrated Hydrological Dynamics in Complex Alpine Headwaters: Potential and Challenges. *Water Resources Research*, *58*(4), e2020WR029390. https://doi.org/10.1029/2020WR029390

Tiwari, T., Lidman, F., Laudon, H., Lidberg, W., & Ågren, A. M. (2017). GIS-based

prediction of stream chemistry using landscape composition, wet areas, and hydrological flow pathways: Modeling Biogeochemistry. *Journal of Geophysical Research: Biogeosciences*, *122*(1), 65–79. https://doi.org/10.1002/2016JG003399

Toller, E. A. L. (2022). An Analytic Element Model for Intersecting and Heterogeneous Fractures in Groundwater Flow. *Water Resources Research*, *58*(5), e2021WR031520. https://doi.org/10.1029/2021WR031520

Tóth, J. (1963). A theoretical analysis of groundwater flow in small drainage basins. *Journal of Geophysical Research*, *68*(16), 4795–4812. https://doi.org/10.1029/JZ068i016p04795

Toth, J. (1963). A theoretical analysis of groundwater flow in small drainage basins. *Journal of Geophysical Research*, *68*(16), 4795–4812.

Troldborg, L., Refsgaard, J. C., Jensen, K. H., & Engesgaard, P. (2007). The importance of alternative conceptual models for simulation of concentrations in a multi-aquifer system. *Hydrogeology Journal*, *15*(5), 843–860. https://doi.org/10.1007/s10040-007-0192-y

Tsutsumi, A., Nishino, S., Mizoguchi, K., Hirose, T., Uehara, S., Sato, K., Tanikawa, W., & Shimamoto, T. (2004). Principal fault zone width and permeability of the active Neodani fault, Nobi fault system, Southwest Japan. *Tectonophysics*, *379*(1–4), 93–108. https://doi.org/10.1016/j.tecto.2003.10.007

UN. (2017). *2010–2020: UN Decade for Deserts and the Fight against Desertification*. https://www.un.org/en/events/desertification_decade/whynow.shtml

Valdenegro, P., Muñoz, M., Yáñez, G., Parada, M. A., & Morata, D. (2019). A model for thermal gradient and heat flow in central Chile: The role of thermal properties. *Journal of South American Earth Sciences*, *91*, 88–101. https://doi.org/10.1016/j.jsames.2019.01.011

Vignoli, G., Cassiani, G., Rossi, M., Deiana, R., Boaga, J., & Fabbri, P. (2012). Geophysical characterization of a small pre-Alpine catchment. *Journal of Applied Geophysics*, *80*, 32–42. https://doi.org/10.1016/j.jappgeo.2012.01.007

Viguier, B., Daniele, L., Jourde, H., Leonardi, V., & Yáñez, G. (2019). Changes in the conceptual model of the Pampa del Tamarugal Aquifer: Implications for Central Depression water resources. *Journal of South American Earth Sciences*, *94*, 102217. https://doi.org/10.1016/j.jsames.2019.102217

Viguier, B., Jourde, H., Yáñez, G., Lira, E. S., Leonardi, V., Moya, C. E., García-Pérez, T., Maringue, J., & Lictevout, E. (2018). Multidisciplinary study for the assessment of the geometry, boundaries and preferential recharge zones of an overexploited aquifer in the Atacama Desert (Pampa del Tamarugal, Northern Chile). *Journal of South American Earth Sciences*, *86*, 366–383. https://doi.org/10.1016/j.jsames.2018.05.018

Vittecoq, B., Reninger, P.-A., Lacquement, F., Martelet, G., & Violette, S. (2019). Hydrogeological conceptual model of andesitic watersheds revealed by high-resolution heliborne geophysics. *Hydrology and Earth System Sciences*, *23*(5), 2321–2338. https://doi.org/10.5194/hess-23-2321-2019

Viviroli, D., Archer, D. R., Buytaert, W., Fowler, H. J., Greenwood, G. B., Hamlet, A.

F., Huang, Y., Koboltschnig, G., Litaor, M. I., López-Moreno, J. I., Lorentz, S., Schädler, B., Schreier, H., Schwaiger, K., Vuille, M., & Woods, R. (2011). Climate change and mountain water resources: Overview and recommendations for research, management and policy. *Hydrology and Earth System Sciences*, *15*(2), 471–504. https://doi.org/10.5194/hess-15-471-2011

Viviroli, D., Kummu, M., Meybeck, M., Kallio, M., & Wada, Y. (2020). Increasing dependence of lowland populations on mountain water resources. *Nature Sustainability*, *3*(11), 917–928. https://doi.org/10.1038/s41893-020-0559-9

Voeckler, H., & Allen, D. M. (2012). Estimating regional-scale fractured bedrock hydraulic conductivity using discrete fracture network (DFN) modeling. *Hydrogeology Journal*, *20*(6), 1081–1100. https://doi.org/10.1007/s10040-012-0858-y

Vuille, M., Carey, M., Huggel, C., Buytaert, W., Rabatel, A., Jacobsen, D., Soruco, A., Villacis, M., Yarleque, C., Elison Timm, O., Condom, T., Salzmann, N., & Sicart, J.-E. (2018). Rapid decline of snow and ice in the tropical Andes – Impacts, uncertainties and challenges ahead. *Earth-Science Reviews*, *176*, 195–213. https://doi.org/10.1016/j.earscirev.2017.09.019

Wang, J., Jiang, X., Zhang, Z., Wan, L., Wang, X., & Li, H. (2017). An analytical study on three-dimensional versus two-dimensional water table-induced flow patterns in a Tóthian basin. *Hydrological Processes*, *31*(22), 4006–4018. https://doi.org/10.1002/hyp.11317

Welch, L. A., & Allen, D. M. (2012). Consistency of groundwater flow patterns in mountainous topography: Implications for valley bottom water replenishment and for defining groundwater flow boundaries. *Water Resources Research*, *48*(5). https://doi.org/10.1029/2011WR010901

Welch, L. A., & Allen, D. M. (2014). Hydraulic conductivity characteristics in mountains and implications for conceptualizing bedrock groundwater flow. *Hydrogeology Journal*, *22*(5), 1003–1026. https://doi.org/10.1007/s10040-014-1121-5

Weyer, C., Peiffer, S., Schulze, K., Borken, W., & Lischeid, G. (2014). Catchments as heterogeneous and multi-species reactors: An integral approach for identifying biogeochemical hot-spots at the catchment scale. *Journal of Hydrology*, *519*, 1560–1571. https://doi.org/10.1016/j.jhydrol.2014.09.005

White, B. A., & Burbey, T. J. (2007). Evidence for structurally controlled recharge in the Blue Ridge Province, Virginia, USA. *Hydrogeology Journal*, *15*(5), 929–943. https://doi.org/10.1007/s10040-006-0150-0

Wilske, C., Suckow, A., Mallast, U., Meier, C., Merchel, S., Merkel, B., Pavetich, S., Rödiger, T., Rugel, G., Sachse, A., Weise, S. M., & Siebert, C. (2020). A multi-environmental tracer study to determine groundwater residence times and recharge in a structurally complex multi-aquifer system. *Hydrology and Earth System Sciences*, *24*(1), 249–267. https://doi.org/10.5194/hess-24-249-2020

Wilson, J. L., & Guan, H. (2004). Mountain-block hydrology and mountain-front recharge. *Groundwater Recharge in a Desert Environment: The Southwestern United States*, *9*, 113–137.

Winter, T. C. (1999). Relation of streams, lakes, and wetlands to groundwater flow systems. *Hydrogeology Journal*, *7*(1), 28–45. https://doi.org/10.1007/s100400050178

Winter, T. C. (2001). The concept of hydrologic landscapes 1. *JAWRA Journal of the American Water Resources Association*, *37*(2), 335–349. https://doi.org/10.1111/j.1752-1688.2001.tb00973.x

Xue, L., Li, H.-B., Brodsky, E. E., Xu, Z.-Q., Kano, Y., Wang, H., Mori, J. J., Si, J.-L., Pei, J.-L., Zhang, W., Yang, G., Sun, Z.-M., & Huang, Y. (2013). Continuous Permeability Measurements Record Healing Inside the Wenchuan Earthquake Fault Zone. *Science*, *340*(6140), 1555–1559. https://doi.org/10.1126/science.1237237

Yáñez, G., & Cembrano, J. (2004). Role of viscous plate coupling in the late Tertiary Andean tectonics. *Journal of Geophysical Research: Solid Earth*, *109*(B2), 2003JB002494. https://doi.org/10.1029/2003JB002494

Yáñez, G., & Herrera, O. R. (2019). Crustal dense blocks in the fore-arc and arc region of Chilean ranges and their role in the magma ascent and composition: Breaking paradigms in the Andean metallogeny. *Journal of South American Earth Sciences*, *93*, 51–66. https://doi.org/10.1016/j.jsames.2019.04.006

Yáñez, G., Munoz, M., Flores-Aqueveque, V., & Bosch, A. (2015). Gravity derived depth to basement in Santiago Basin, Chile: Implications for its geological evolution, hydrogeology, low enthalpy geothermal, soil characterization and geo-hazards. *Andean Geology*, *42*(2), 147–172. https://doi.org/10.5027/andgeoV42n2-a01

Yáñez, G., Perez-Estay, N., Araya-Vargas, J., Sanhueza, J., Figueroa, R., Maringue, J., & Rojas, T. (2020). Shallow Anatomy of the San Ramón Fault (Chile) Constrained by Geophysical Methods: Implications for its Role in the Andean Deformation. *Tectonics*, *39*(8), e2020TC006294. https://doi.org/10.1029/2020TC006294

Yao, Y., Zheng, C., Andrews, C., Zheng, Y., Zhang, A., & Liu, J. (2017). What controls the partitioning between baseflow and mountain block recharge in the Qinghai-Tibet Plateau?: Mountainous Groundwater Flow System. *Geophysical Research Letters*, *44*(16), 8352–8358. https://doi.org/10.1002/2017GL074344

Yao, Y., Zheng, C., Liu, J., Cao, G., Xiao, H., Li, H., & Li, W. (2015). Conceptual and numerical models for groundwater flow in an arid inland river basin. *Hydrological Processes*, *29*(6), 1480–1492. https://doi.org/10.1002/hyp.10276

Yihdego, Y., Danis, C., & Paffard, A. (2015). 3-D numerical groundwater flow simulation for geological discontinuities in the Unkheltseg Basin, Mongolia. *Environmental Earth Sciences*, *73*(8), 4119–4133. https://doi.org/10.1007/s12665-014-3697-4

Zambrano-Bigiarini, M., Nauditt, A., Birkel, C., Verbist, K., & Ribbe, L. (2017). Temporal and spatial evaluation of satellite-based rainfall estimates across the complex topographical and climatic gradients of Chile. *Hydrology and Earth System Sciences*, *21*(2), 1295–1320. https://doi.org/10.5194/hess-21-1295-2017

Zhang, X., Jiao, J. J., & Guo, W. (2022). How Does Topography Control Topography-Driven Groundwater Flow? *Geophysical Research Letters*, *49*(20), e2022GL101005. https://doi.org/10.1029/2022GL101005

A. APPENDICES

A.1. Supplementary Material for chapter 3

Framework for 2D analytical solutions and sensitivity analysis of solution parameters

Bresciani et al. (2014) devised an analytical approach based on the Dupuit-Forchheimer assumption to estimate seepage length in hillslopes. This particular hillslope scenario is depicted in Figure A-1, where d [L] represents the depth to the impervious base beneath the streambed, L [L] denotes the hillslope length, L_S [L] the seepage length, K [LT^{-1}] the hydraulic conductivity, R [LT^{-1}] the available recharge rate, and s [-] the topographic slope.

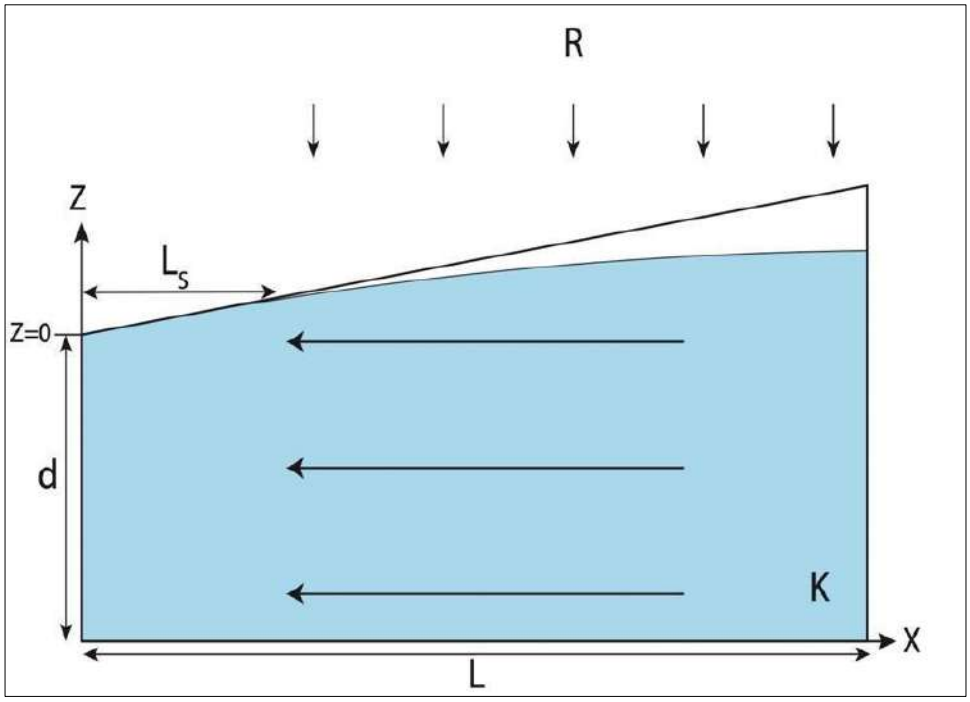

Figure A-1 Illustration of the 2D hillslope model employed to define the analytical solution, based on Bresciani et al. (2014).

In this 2D hillslope framework, the model top (Z_T) is represented as a constant slope topography:

$$Z_T(x) = sx$$

with s [-] the topographic slope.

For this case the ratio between seepage length and hillslope length is defined, by mass balance, as:

$$\frac{L_S}{L} = \frac{1 - \frac{sKd}{RL}}{1 + \frac{s^2K}{R}}$$

To delve deeper into the geomorphological impact and introduce complexity beyond the constant slope framework, Bresciani et al. (2014) introduced variable slope topography, including the concave case:

$$Z_{Tconcave}(x) = sx + \frac{1}{2}bx^2$$

Or convex case:

$$Z_{Tconvex}(x) = sx - \frac{1}{2}bx^2$$

With b [-] the curvature degree.

Here, we expand this work with the Dupuit solution seepage length estimation from the three different cases. For comparison purpose, we introduce a constraint on topography borders as:

$$Z_T(x = 0) = Z_{Tconcave}(x = 0) = Z_{Tconvex}(x = 0)$$

And:

$$Z_T(x = L) = Z_{Tconcave}(x = L) = Z_{Tconvex}(x = L)$$

To take this constraint into account, we need to accommodate the expression of the concave and convex topography:

$$\Longrightarrow Z_{Tconcave}(x) = \frac{2s - bL}{2}x + \frac{1}{2}bx^2$$

$$\Longrightarrow Z_{Tconvex}(x) = \frac{2s + bL}{2}x - \frac{1}{2}bx^2$$

Resolving the same mass balance as for the linear case, for the concave and convex cases, the seepage length (L_S/L) is determined as the real roots of the following 3rd degree polynomials:

For concave case:

$$\frac{1}{2}(bL)^2\left(\frac{L_S}{L}\right)^3 + \frac{3bL(2s - bL)}{4}\left(\frac{L_S}{L}\right)^2 + \left(\frac{R}{K} + \frac{(2s - bL)^2}{4} + \frac{d}{L}bL\right)\left(\frac{L_S}{L}\right) + \frac{(2s - bL)}{2}\frac{d}{L} - \frac{R}{K} = 0$$

For convex case:

$$\frac{1}{2}(bL)^2\left(\frac{L_S}{L}\right)^3 - \frac{3bL(2s + bL)}{4}\left(\frac{L_S}{L}\right)^2 + \left(\frac{R}{K} + \frac{(2s + bL)^2}{4} - \frac{d}{L}bL\right)\left(\frac{L_S}{L}\right) + \frac{(2s + bL)}{2}\frac{d}{L} - \frac{R}{K} = 0$$

In this study, our primary focus was on the L_S/L ratio in comparison to the K/R ratio. To comprehensively investigate the analytical solution, we conducted a sensitivity analysis on the slope parameter, which serves as the most significant indicator of topography in this specific case. For this analysis, the hillslope length (L) was set to 1,000 m, and the depth to impervious base (d) was maintained at d=100 m to respect the ratio d/L=0.1 and to consider the Dupuit Forchheimer condition (d/L < 0.2) (Bresciani et al., 2014; Haitjema & Mitchell-Bruker, 2005). We considered a range of slope values, spanning [0.02, 0.05, 0.1, 0.15, 0.2, 0.25, 0.3, 0.4].

To further explore the effects of these cases, we conducted a sensitivity study on the curvature degree. For this analysis, we maintained a fixed slope (s=0.2), and the

curvature degree multiplied by the hillslope length (bL) was varied in the range [0.01, 0.05, 0.1, 0.15, 0.2] for the concave case and in the opposite range [-0.01, -0.05, -0.1, -0.15, -0.2] for the convex case.

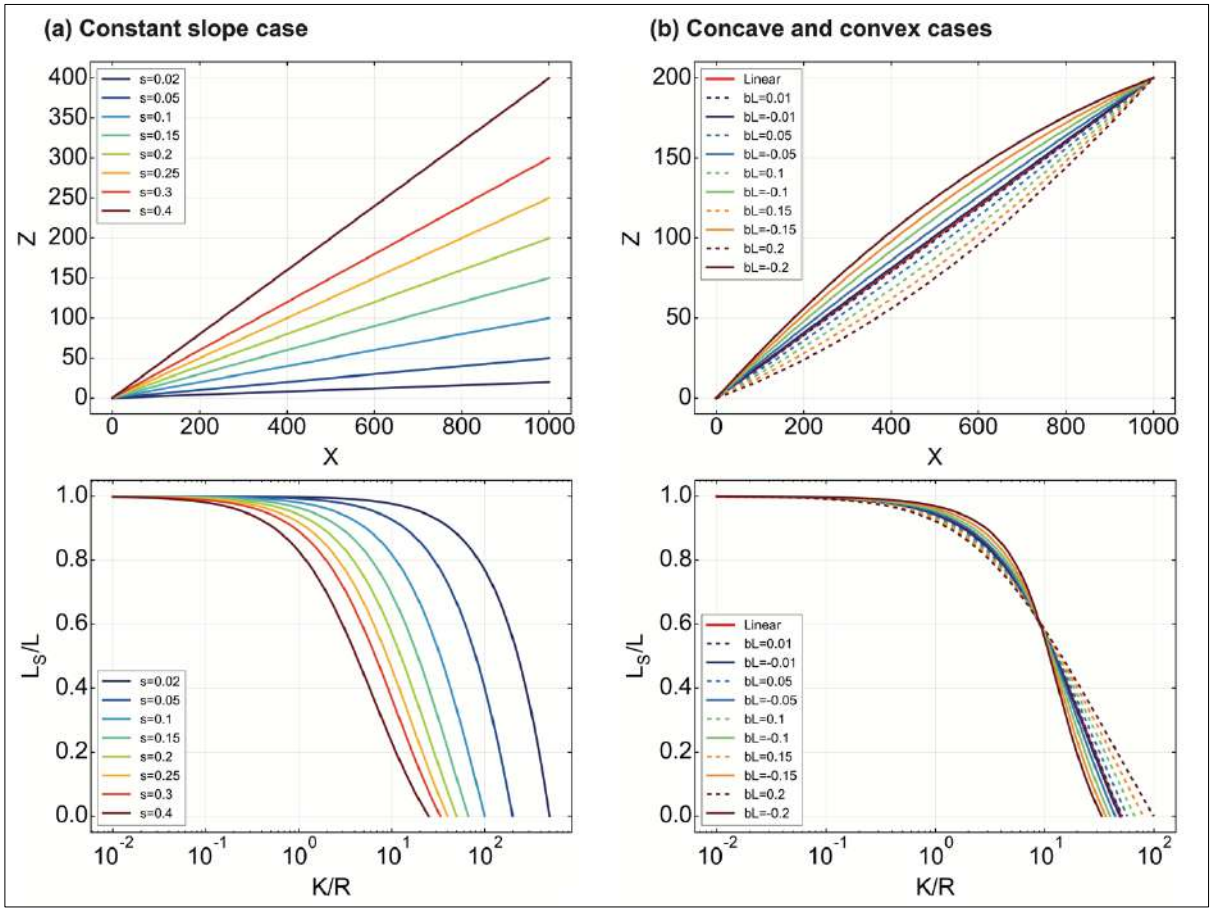

Figure A-2 (a) Left upper panel: Topography of the hillslope Z_T, with each color corresponding to a different slope value. Left lower panel: Seepage length ratio L_S/L plotted against the ratio R/K for each hillslope case presented on the left upper panel using the same color palette. (b) Right upper panel: Topography of the hillslope Z_T, with each color corresponding to a different curvature degree value. Dashed lines represent concave cases, and solid lines represent convex cases. The linear case is represented by a solid red line. Right lower panel: Seepage length ratio L_S/L plotted against the ratio R/K for each hillslope case presented on the right upper panel, using the same color palette and line patterns.

Figure A-2 presents the results of the sensitivity study with the slope (s) for the left panel and curvature degree (bL) on the right panel. The lower panel Figure A-2 presents the ratio L_S/L for the various topography described on the upper panel plotted against the ratio K/R. Regarding the varying slope (s) on the left panel of Figure A-2, the results show that slope incrementation exhibits a linear effect, with gentler slopes remaining fully saturated for a higher number of K/R and reaching $L_S/L = 0$ for the highest value of K/R. In contrast, steeper slopes desaturate at lower K/R and intercept $L_S/L = 0$ for the smallest value of K/R. The right panel of Figure A-2 displays the results for the concave and convex cases. In terms of seepage length, we observed distinct behaviors between concave and convex topography, with more pronounced effects as the degree of curvature increased. In the convex hillslope case, remains fully saturated for a higher K/R, but the desaturation rate become quicker, leading to full desaturation ($L_S/L=0$) before the linear case. Conversely, desaturation occurred earlier in the concave hillslope cases (lower K/R), but with a slower rate, indicating that they reached total desaturation ($L_S/L=0$) beyond the linear case.

Overall, we noticed that the curvature degree has a secondary influence on the seepage length compared to the slope value (Figure A-2 left versus right panel). Nevertheless, there is a noteworthy effect of the curvature degree on the desaturation rate of the hillslope.

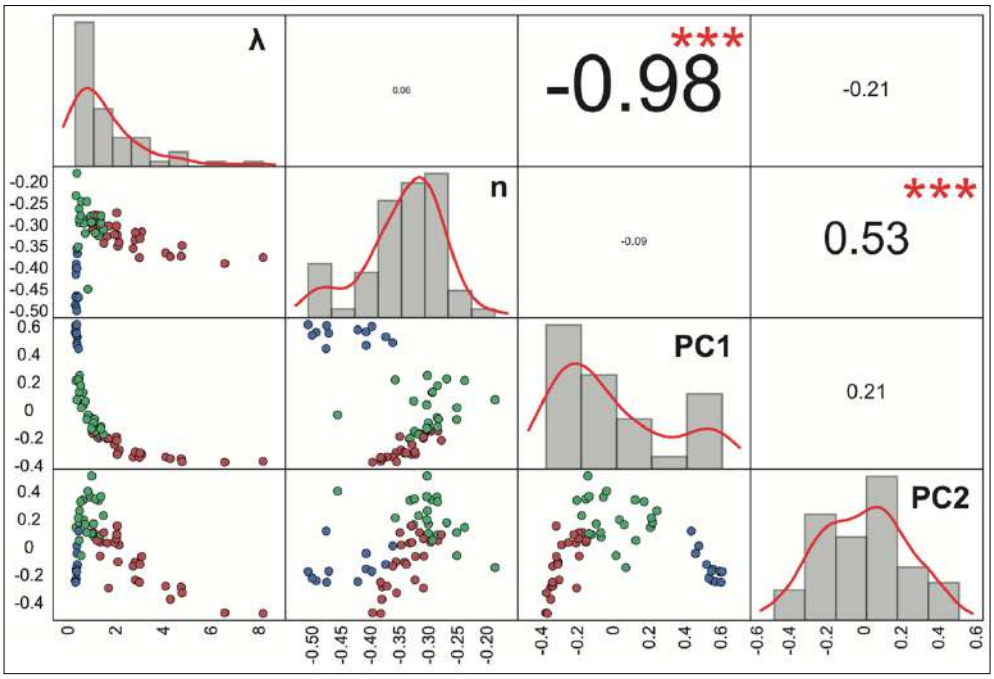

Figure A-3 Correlation matrix between topographical parameters (PC1 and PC2) and seepage distribution parameters (λ and n) obtained from the curve fit. The diagonal part represents the distribution of each parameter associated with its name. The upper part indicates the correlation coefficient (r) between two variables, with stars indicating the strength of the correlation on a scale from 0 to 3 (for 3 stars p-value<0.001). The lower part represents the scatter plot between the two corresponding variables using the clusters color scheme. The X-axis is associated with both the scatter plots and the histogram distribution, while the Y-Axis is only associated with the scatter plots.

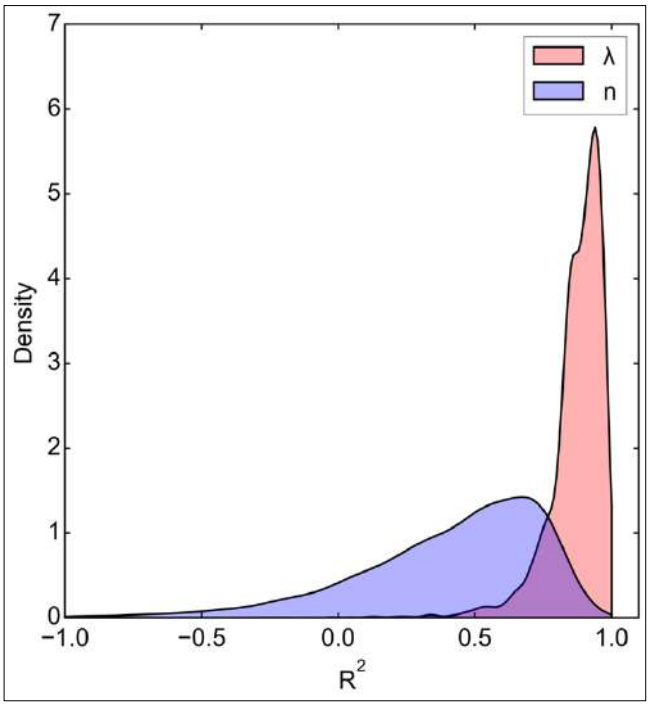

Figure A-4 Kernel Density Estimate (KDE) plot depicting the coefficient of determination (R^2) for parameter estimations of λ and n using a Random Forest algorithm. Each R^2 value corresponds to one of 6500 resampling (with replacements) iterations involving 10 catchments, serving as test data within a 60-catchment dataset, while 50 catchments were utilized for training. The sampling procedure was conducted to assess the estimation's robustness in the presence of random variations.

A.2. Supplementary Material for chapter 4

Geophysical results For the Rio Coipo transect (B-B', Figure 4-1)

As stated in section 4.1.1 a second transect is located 10-km up north of the reserve and further east, in the Rio Coipo valley. We present the results in this appendix. This transect is separated in 3 distinct zone associated only with the Rio Coipo Valley and based on geological considerations and results interpretation.

The ERT Rio Coipo transect (Figure A-5) shows a generally more conductive environment than the Rio Clarillo one. Overall, there is a conductive layer, with resistivity values below 200 ohm.m, over a more resistive layer with values ranging between 300 and 3,000 ohm.m. This profile shows a lot more heterogeneities than the Rio Clarillo one, with low resistivity zones at depth. These areas are located between 200 and 600 m, 1,000 and 1,300 m, 1,800 and 2,000 m or between 2,300 and 2,600 m. The last part of the profile between 2,800 and 3,400 m shows a high resistivity zone (>800 ohm.m). Centered on 1,500 m, is located a punctual highly resistive body (> 2,000 ohm.m).

Interpreting this ERT transect with the help of the geological map, we can determine that the limit between the intrusive unit at east and volcanic unit at west is located around 1,000 m along the profile. This contact between the two units presents a resistivity contrast represented by the low resistivity zone between 1,000 and 1,300 m. Compared with the Rio Clarillo transect (Figure 4-3) the resistivity values of the intrusive unit are lower (until 1,000 m) (around 300-500 Ohm.m). Although it is expected that intrusive was more resistant, the zone shows strong alteration with possible alluvial deposits over the more resistive plutonic intrusion inducing low resistivities values. The volcanic unit environment, west of 1,000 m, there presents similar resistivity values as on the Rio Clarillo profile (Figure 4-3), between 200 and 1,000 Ohm.m. This highly heterogeneous character of this profile both in the intrusive or the volcanic unit, can indicate important

impact of alteration in the area, including possible zones of mass removal (blue zones with low resistivity). Finally, the highly resistive body at 1,500 m inside the volcanic unit, can denote the presence of a metamorphic body at depth. The implementation of the intrusive rock could have had an impact on pressure and temperature condition inducing the formation of a metamorphic body.

The Rio Coipo gravity anomaly profile (Figure A-6) shows three distinct zones. The first one between 0 and 1,000 m shows a negative (between -2 and 0 mGal) slightly increasing anomaly with some irregularities along the curve. At 100 m the anomaly increases significantly until reaching a peak value at 1,800 m of 2.5 mGal. Between 1,800 m and 5,000 m, the anomaly stays above 0 mGal with a decreasing trend until 3,300 m where the anomaly increases again reaching a second peak (2.7 mGal) at 4,000 m. This part of the profile could correspond well to the second zone. The third zone, after the 4,000 m peak and until the end of the profile, shows a sudden drop in the anomaly data until it reaches a negative value of -2 mGal.

The suggested density model (Figure A-6 bottom) has generally a great fit with the anomaly, except at the borders of the where it is more difficult to characterize. The model is showing a deficit of mass in the first and third zones when the second part shows an excess of mass. In the first zone, gravity anomalies variations can be associated with heterogeneities in the intrusive unit, which can be covered by a layer of sediment of variable depth. This model shows a good definition of the contact between intrusive and volcanic units around 1,000 m in accordance with both geologic map and ERT profile (Zone 1). The details of the contact here shows part of the intrusive unit covering the volcanic unit between 500 and 1,000 m. The underlying volcanic layer can explain the positive anomaly at 800 m. The increase of the anomaly between 1,000 m and 1,800 m can also be explained by the growing importance of the volcanic unit along the profile. Secondly, as described on the ERT profile, a metamorphic body was modelled inside this volcanic unit (around 1,500 m), represented by a higher density. This metamorphic body also influence the anomaly upwards reaching the peak value at 1,800 m. The second zone for the Rio Coipo transect corresponds to the volcanic unit. Even though in the same geological unit, the non-linear aspect of the gravity anomalies can be explained by variations of density always according to in-situ rock samples density measurements.

This proves the highly heterogeneous character of this volcanic unit. Finally, the third zone, the clear drop in the anomaly, is identified as a fault zone with intrusive rocks represented by a much lower density (2.50 g/cc). It is in good agreement with the geological map where it shows a damaged zone with intrusive rocks.

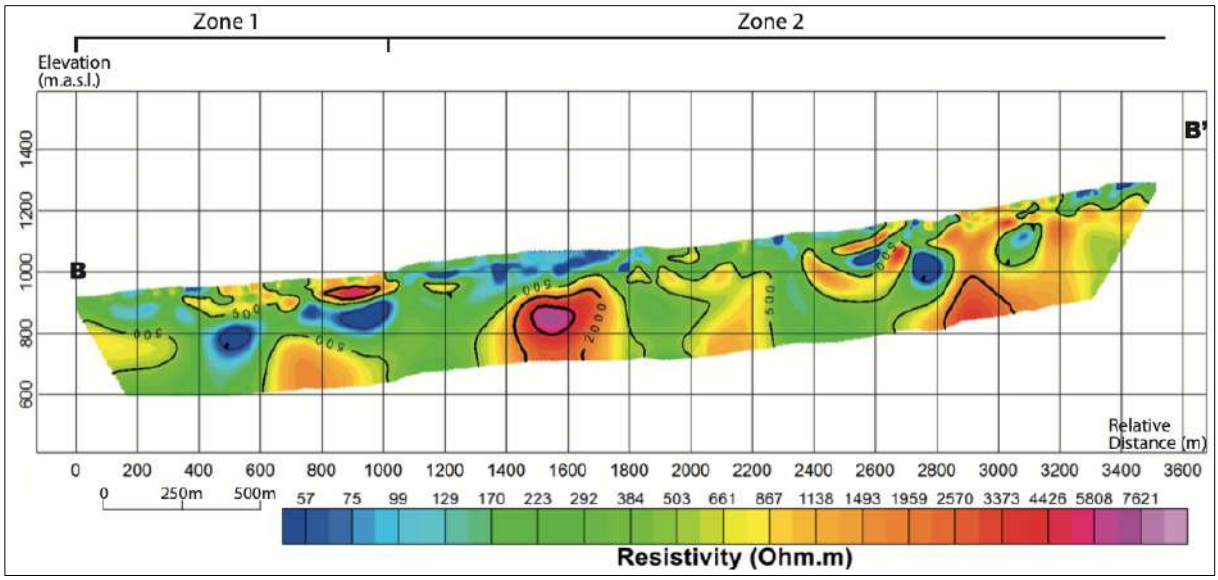

Figure A-5 Electrical resistivity model for the Rio Coipo transect (B-B', Figure 4-1).

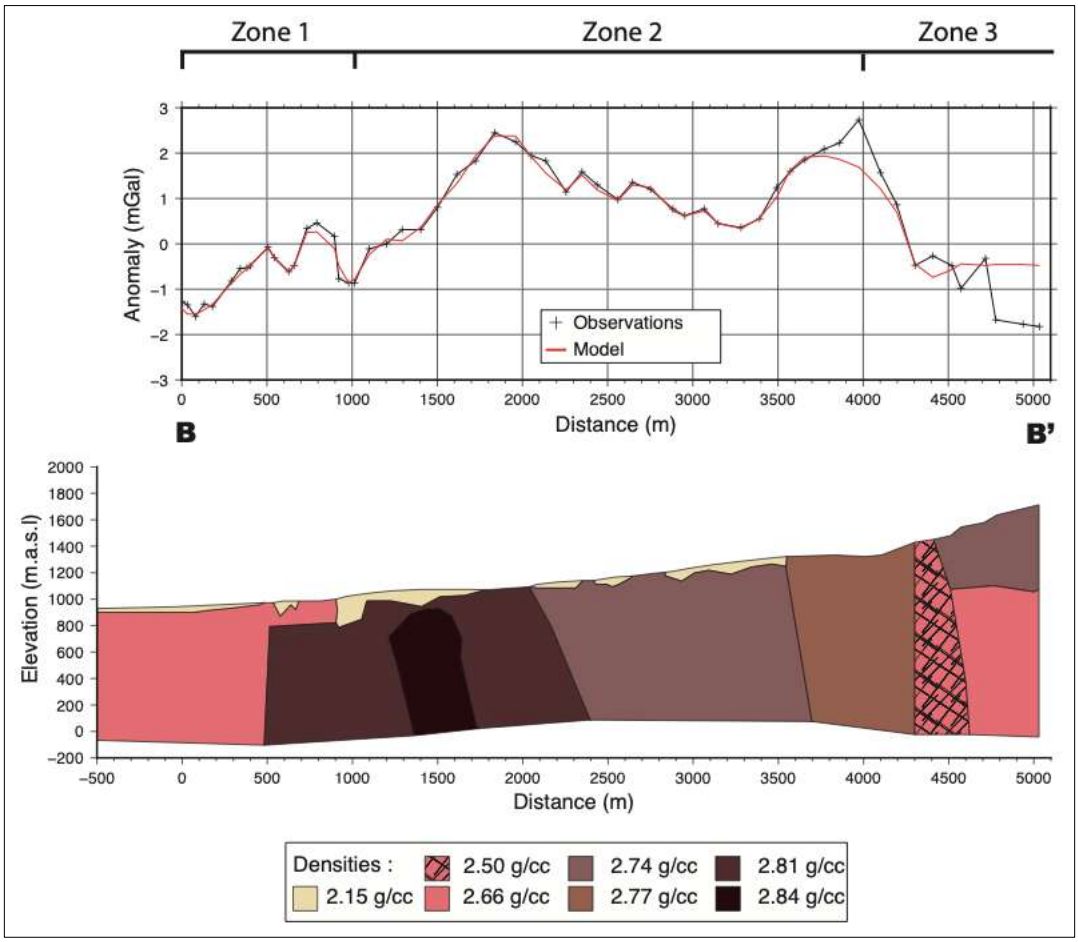

Figure A-6 Model of the gravity data for the Rio Coipo transect (B-B', Figure 4-1) and the associated interpretation derived from geophysical and geological constraints. Top: the black line with crosses represents the data, the red line represents the fit of the model described above. Bottom: Model representing the gravity data based on density variations.

A.3. Supplementary Material for chapter 5

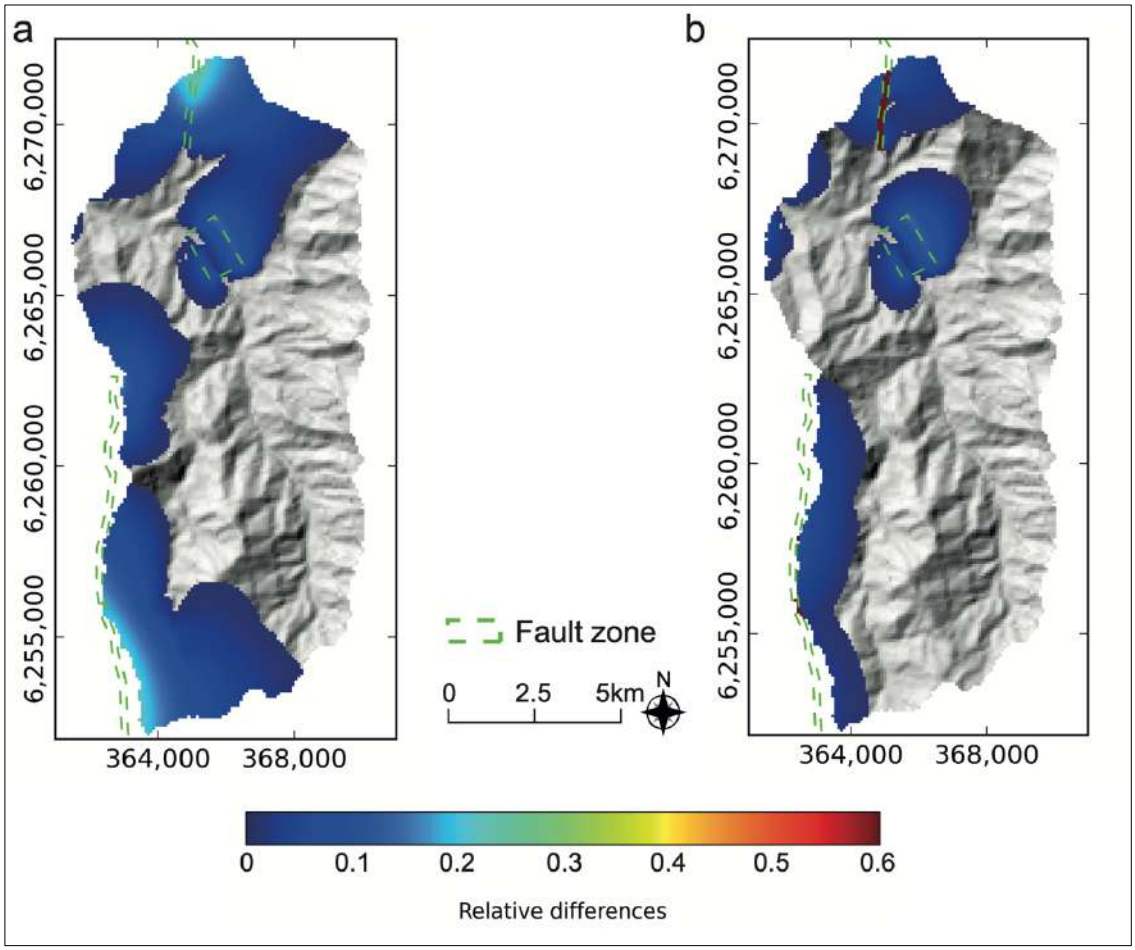

Figure A-7 Maps with topography of head relative differences (null difference is masked) including the fractures area (Scenario 3) for a) the more permeable case and b) the less permeable case.

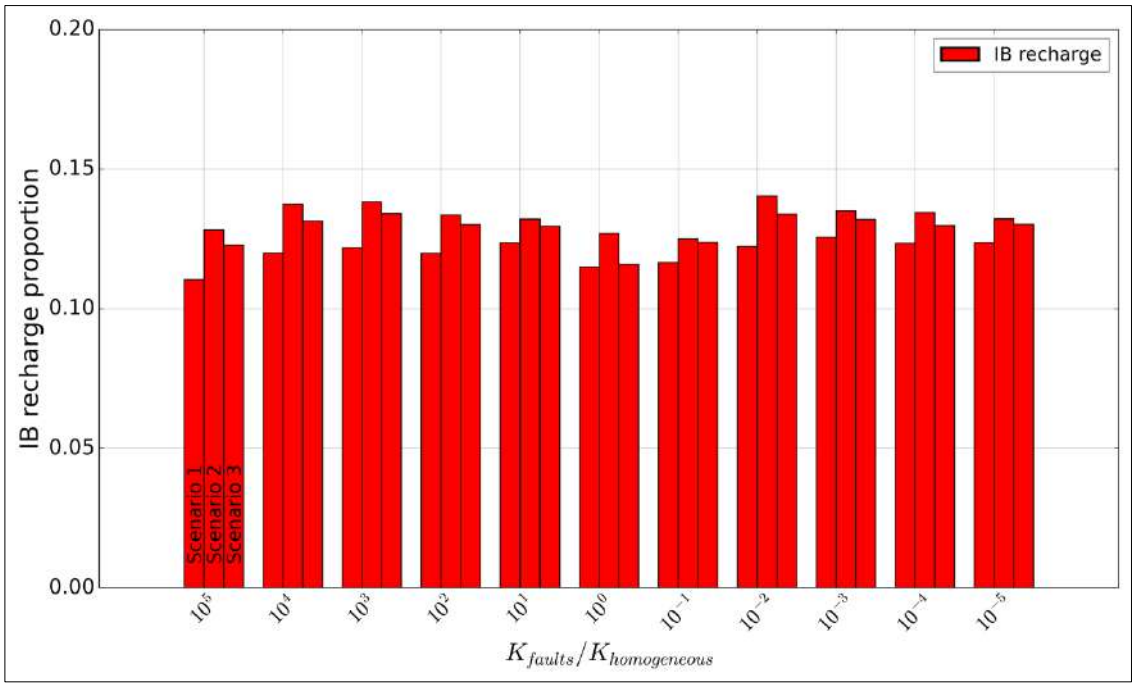

Figure A-8 Bar-plot presenting the proportion of recharge to the catchment coming from IB flows based on the $K_{faults}/K_{homogeneous}$ ranging from the more permeable case to the less permeable case. For each $K_{faults}/K_{homogeneous}$, bars represent one scenario each, scenario 1 to 3 from left to right, representing our 30 simulations. The ratio $K_{faults}/K_{homogeneous} = 10^{0}$ represents the reference case.